ELECTROMAGNETIC INTERFERENCE FROM VARIABLE SPEED MOTOR DRIVES

John David Maggs

Submitted for the Degree of
Doctor of Philosophy

The University of Aston in Birmingham

June 1996

The University of Aston in Birmingham

Electromagnetic Interference from Variable Speed Drives

John David Maggs

Doctor of Philosophy

1996

ABSTRACT: A methodology is presented which can be used to predict the level of electromagnetic interference, in the form of conducted and radiated emissions, from variable speed drives. The drive that was modelled being a Eurotherm 583 drive.

The conducted emissions are predicted using an accurate circuit model of the drive and its associated equipment. The circuit model was constructed from a number of different areas, these being: the power electronics of the drive, the line impedance stabilising network used during the experimental work to measure the conducted emissions, a model of an induction motor assuming near zero load, an accurate model of the shielded cable which connected the drive to the motor, and finally the parasitic capacitances that were present in the drive modelled. The conducted emissions were predicted with an error of +/-6dB over the frequency range 150kHz to 16MHz, which compares well with the limits set in the standards which specify a frequency range of 150kHz to 30MHz.

The conducted emissions model was also used to predict the current and voltage sources which were used to predict the radiated emissions from the drive.

Two methods for the prediction of the radiated emissions from the drive were investigated, the first being two-dimensional finite element analysis and the second three-dimensional transmission line matrix modelling.

The finite element model took account of the features of the drive that were considered to produce the majority of the radiation, these features being the switching of the IGBT's in the inverter, the shielded cable which connected the drive to the motor as well as some of the cables that were present in the drive. The model also took account of the structure of the test rig used to measure the radiated emissions. It was found that the majority of the radiation produced came from the shielded cable and the common mode currents that were flowing in the shield, and that it was feasible to model the radiation from the drive by only modelling the shielded cable. The radiated emissions were correctly predicted in the frequency range 30MHz to 200MHz with an error of +10dB/-6dB.

The transmission line matrix method modelled the shielded cable which connected the drive to the motor and also took account of the architecture of the test rig. Only limited simulations were performed using the transmission line matrix model as it was found to be a very slow method and not an ideal solution to the problem. However the limited results obtained were comparable, to within 5%, to the results obtained using the finite element model.

(Key words: Electromagnetic Compatibility, Conducted Emissions, Radiated Emissions, Electric Fields, Mathematical Modelling)

Dedicated to my parents.

"Knowledge is power"

Francis Bacon (1561-1626)

Acknowledgments

Firstly I would like to thank Professor M. T. Wright for supervising me through a very troubled first year at Aston, and for also answering my many questions. Secondly I would like to thank Dr T. Oliver who became my supervisor during the second year of my project and for reading and correcting the many mistakes in my thesis. I would also like to thank all the people who were involved in the Machine Controls & Drives Research Group at Aston for all their advice and support throughout the project, specifically I would like to thank Dr S. Garvey for offering me the chance to do the PhD in the first place. I would also like to thank Jason Hill for answering my questions concerning the use of the software package SABER.

I would like to thank the Engineering and Physical Sciences Research Council for their financial support throughout the project. I would also like to thank Eurotherm Drives for supplying the equipment that was modelled throughout the work and for allowing me use their conducted and radiated emissions test rigs as well as supplying some additional sponsorship throughout the work.

Finally I would like to thank my parents for encouraging me throughout the PhD.

Contents

Figures

Tables

Glossary

AC	Alternating Current
dB	Decibels
DC	Direct Current
CISPR	International Special Committee for Radio Interference
EEC	European Economic Community
EMC	Electromagnetic Compatibility
EMI	Electromagnetic Interference
EUT	Equipment Under Test
FCC	Federal Communications Commission
FDTD	Finite Difference Time Domain
FEA	Finite Element Analysis
FFT	Fast Fourier Transform
GTEM	Gigahertz Transverse Electromagnetic Mode
HF	High Frequency
IC	Integrated Circuit
IEC	International Electrotechnical Commission
IGBT	Insulated Gate Bipolar Transistor
LISN	Line Impedance Stabilising Network
OATS	Open Area Test Site
PCB	Printed Circuit Board
PWM	Pulse Width Modulation
RMS	Root Mean Square
SPICE	Simulation Program with Integrated Circuit Emphasis
TLM	Transmission Line Matrix

Nomenclature

A - cross-sectional area (m)

B - bandwidth (Hz)

C - capacitance (F)

c - speed of light (299.8×10^6 m/s)

d - distance from equipment (m)

d - wire diameter (m)

D - distance between wires (m)

dl - short element length (m)

d/dt - differential operator (1/s)

e - electric charge (C)

E - electric field strength (V/m)

f - frequency (Hz)

{F} - vector of the applied nodal force

g - normalised characteristic conductance

H - magnetic field strength (A/m)

I - current (A)

k - the coefficient of coupling between two inductances

k - Boltzmans constant (1.38×10^{-23} J/K)

[K] - stiffness matrix

l - wire length (m)

L - inductance (H)

L - line length (m)

m - mutual inductance (H)

r - wire radius (m)

R - resistance (Ω)

[s] - TLM scattering matrix

t - time (s)

T - time for a single cycle (s)

T - absolute temperature (K)

$\{U\}$ - vector of unknown voltages or currents

V - potential difference (V)

[V] - TLM vector of pulses

Y - normalised characteristic admittance

Y_o - characteristic admittance ($1/\Omega$)

Z - normalised characteristic impedance

Z_o - characteristic impedance (377Ω)

Δl - TLM modelling node size (m)

Δt - time step (s)

ε_o – permittivity of free space (8.854×10^{-12}F/m)

ε_r – relative permittivity

λ – wavelength (m)

μ_o – permeability of free space ($4\pi \times 10^{-7}$H/m)

μ_r - relative permeability

ρ - resistivity (Ωm)

σ - conductivity (S/m)

ω – angular frequency (rad/s)

Common Subscripts:

cm - common mode

dm - differential mode

n - nodal

x - x-direction

y - y-direction

z - z-direction

Common Superscripts:

i - incident

r - reflected

Chapter 1

Introduction

1.1 Motivation

The aim of this research project was to produce a reliable design methodology for the prediction of the Electromagnetic Interference (EMI), in terms of conducted and radiated emissions, emanating from variable speed motor drives and their related control equipment. These methods can then be used to assist a designer in determining whether a design complies with the Electromagnetic Compatibility (EMC) legislations.

The research was funded by the Engineering and Physical Sciences Research Council (EPSRC) and Eurotherm Drives Ltd. All the devices modelled throughout the research were supplied by Eurotherm Drives Ltd.

Within the last 30 to 40 years man has started to produce electromagnetic noise as well as producing intentional electromagnetic radiation in the form of television signals, radios and portable phones, and it was with this production of noise that man started to have problems with electromagnetic compatibility, or EMC as it is better known. EMC can have many effects from preventing a television from working correctly to affecting a life support system in a hospital. Some of the reported effects of EMI (Williams (1993)) include:

- On a particular car, the central locking and the electric sunroof would start to operate when the car's mobile phone was used.

- When a piezoelectric cigarette lighter was operated near the cabinet of a car park barrier control box the radiated pulse would cause the barrier to raise and allow the drivers to park free of charge.

- Interference to aeronautical safety communications at a US airport was traced to an electronic cash register a mile away.

- The instrument panel of a well known airliner was said to carry the warning "ignore all instruments whilst transmitting HF".

In recognition of this increase with problems associated with EMC/EMI, many countries have begun to implement legislations on the amount of emissions allowed from electrical equipment. It was this implementation in legislations and the new European EMC directive that is due to come into force in 1996 governing the levels of emission and susceptibility for all electrical and electronic devices that are going to be sold in the EEC that caused this project to come into being.

Due to the problems with EMC/EMI that have been briefly discussed above there has been a significant increase in the amount of literature available on EMC. Most of this literature falls into four main areas, these areas being:

1. Modelling of electrical and electronic systems.
2. Measurement of emissions.
3. Design principles for the reduction of EMC.
4. The EMC directive.

The modelling and the reduction of EMC/EMI will be discussed in the literature review, but the thesis will be mainly concerned with the modelling of radiated and conducted emissions.

1.2 Literature Review

The following literature review will be broken down into three areas, the modelling of conducted emissions, the modelling of radiated emissions and the prevention of emissions.

1.2.1 Modelling of Conducted Emissions

A conducted emission as described by Christopoulos (1992a), is where a mixture of unwanted signals propagate in signal and power supply cables.

There are a number of different methods that can be applied to model the crosstalk from a circuit or a cable. Crosstalk is a mixture of capacitive and inductive coupling which allows a signal from one cable to corrupt a neighbouring cable, and is an important cause of conducted emissions. One of the more common methods that is generally applied to predict the crosstalk between cables and pcb tracks, is transmission line modelling. To be able to model a cable as a transmission line model the individual wires need to be parallel. Paul (1979a) showed how a transmission line model could be applied to model a simple configuration of a generator wire, a receptor wire and a ground wire, in terms of the crosstalk that would occur between the wires. With the transmission line model the wires are modelled as an inductance, with capacitances and mutual inductances connecting the wires together. In Paul (1979b) a transmission line model is generated for a ribbon cable with twenty wires in it, and the cables were again modelled as a combination of inductance, mutual inductance and capacitance. The model was accurate to within 1dB for cable lengths when the line was electrically short (total line length less than a tenth of a wavelength), and within 6dB for lengths of cable that were electrically long (total line length more than a tenth of a wavelength). In Paul & McKnight (1979a) a transmission line model is presented for the prediction of crosstalk in twisted pairs of wires. The model assumes that the twisted wires were made up of a series of short parallel lengths, with an infinitesimally small twist distance between each length. This resulted in a transmission line model for the twisted wires that consisted of a series of loops with an abrupt change of the wire position at the end of each loop. For short lengths of wire (total line length less than a tenth of a wavelength) the model had a 3dB error when compared to experimental results. In a later paper Paul & McKnight (1979b) simplified their previous model for twisted wire pairs by combining the capacitive and inductive coupling into one term, this resulted in the computational effort being reduced, but it also meant that the model would only operate at low frequencies. In Paul (1989a) a transmission line model is presented for the prediction of the crosstalk between the tracks on a printed circuit board, which Paul claimed was capable of predicting the crosstalk from a typical pcb track. In a summary paper, Paul (1991) shows how transmission line models can be applied to various cable layouts, to predict the crosstalk between the cables, situations included ribbon cables, twisted pairs of wires, printed circuit boards and shielded wires.

When shielded cables are used the crosstalk effects are different to unshielded cables, this difference being due to the shield and to the pigtail that is used to ground the shielding, see Figure 1.1 for details. Paul (1980) showed with a simple model based on the coupling over the pigtail sections and the shielded sections that the pigtail sections of shielded wires can greatly reduce the effectiveness of the shield. Paul backed up this claim with experimental data, and Paul also proposed that the pigtail sections of the cable should either be minimised in size or they should be eliminated altogether.

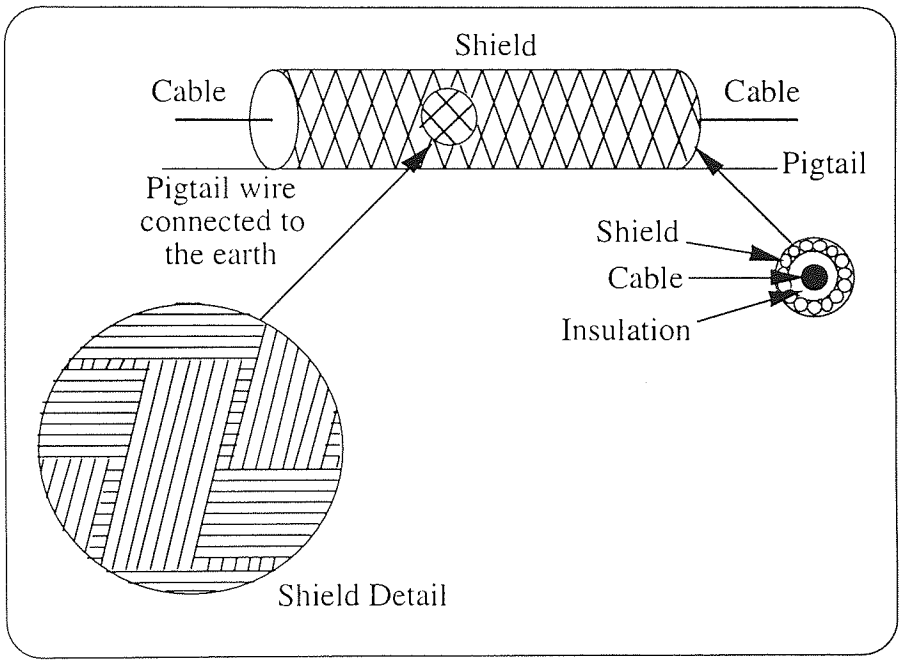

Figure 1.1: Shielded Cable Detail

Even though transmission line models are a useful way of predicting how much crosstalk there will be between two cables, they cannot be used to predict the total amount of conducted emissions emanating from a piece of equipment. Mahdavi *et al* (1993) modelled the differential mode emissions from an AC/DC convertor using the 'MC2' software (MC2 is a simulation tool which simulates the waveforms in a problem), an error of 5dB was found between the experimental and the calculated emissions. In a further paper Mahdavi *et al* (1994) presented a model to simulate the common mode emissions from an AC/DC convertor. This model was more complex than the differential mode model as it included the parasitic capacitances between the convertor and the ground plane (i.e the heatsink) and the loop inductances, with the

error in this model being 20dB. Hargis (1994) demonstrated that it was possible to produce some fairly simple circuit models using a computer package that was similar to SPICE (Simulated Program with Integrated Circuit Emphasis), Rashid (1993). The package predicted the common mode and differential mode conducted emissions. He also found that above 10MHz unexpected effects can occur which make the prediction of the emissions extremely difficult.

1.2.2 Modelling of Radiated Emissions

Christopoulos (1992a) described a radiated emission as the generation of electromagnetic waves from cables and pcb's, and takes the form of an electromagnetic wave travelling through space.

The most obvious way of modelling the electromagnetic radiation from a simple device is to apply standard electromagnetic theory and calculate the fields from Maxwell's equations, Popovic (1973) and Kraus (1992). Obviously when the device starts to get more complex, as with the majority of electrical devices, the application of these theorems is time consuming and complex so various methods of calculating the electromagnetic radiation from complicated systems have been developed. Most of these methods have been summarised by Hubing (1991).

One of the most intuitive methods is the Transmission Line Matrix (TLM) method which was developed by Johns & Beurle (1971), and is described in detail by Hoefer (1985) and Hoefer & So (1992). TLM is a time-domain, differential, numerical modelling method, that is based on the close analogy between the propagation of a plane electromagnetic wave and the propagation of voltage and current along a transmission line. The model is generated by breaking the area to be simulated into a series of transmission lines which intersect at right angles to form nodes, and the time taken for the wave to travel between nodes is a time step. The model would then be excited by the application of voltages, currents or field strengths, and then the sources can be monitored at the required points. Christopoulos (1990) showed how the TLM method could be used to model a simple parallel plate capacitor,and demonstrated how

the method could be integrated into field analysis software. He also outlined a number of areas where the TLM method could be applied, and these regions are:

1. Source region modelling.
2. External interaction (susceptibility).
3. Internal interaction (susceptibility).
4. Field to wire coupling.
5. Multi-conductor coupling.
6. Mapping of transient electromagnetic fields.

Christopoulos & Herring (1993) showed how the TLM method could be applied to three different problems. The first problem was the radiation produced by a spherical dipole placed near conducting walls. The second problem was to determine the emissions produced by a typical device that would be tested for its emission properties. The third problem was to determine the currents induced in two wires that were situated on either side of a thin conducting plate. The results from the first problem were confirmed by determining the radiation resistance of the electromagnetic wave, it was found that in the far field the radiation resistance was converging to the value of the resistance of free space (377Ω). The second problem only showed how the TLM method was capable of predicting changes in the field generated around a device, and no comparisons with experimental results were made. The results from the third problem were compared to published results and it was found that the model was accurate to within 4dB. Duffy *et al* (1993) demonstrated the use of the TLM method in the field of EMC by showing how the method could be used for simulating the electromagnetic radiation. Two different problems were presented the first one being two wires being excited by a third wire in a screened room, and the second problem concerned an equipment casing with an aperture. A good correlation between the simulated results and the measured results was obtained. Johns *et al* (1993) showed how the TLM method could be applied to determine the interaction of electromagnetic fields with equipment housings, pcb's, aircraft, automobiles, ships and military vehicles.

A method that solves Maxwell's time dependent curl equations is known as the Finite-Difference Time-Domain (FDTD) method. This method solves Maxwell's time dependent curl equations. The FDTD grid is constructed from two interlaced grids, the first grid contains the points at which the magnetic field is calculated and the second grid contains the points at which the electric field is calculated. The electric and magnetic fields are alternately calculated at each time step, and the fields propagate throughout the grid. Tirkis *et al* (1993) showed how the FDTD method could be applied to simulate a helicopter for three different EMC situations. The first situation was radiation and this was simulated by attaching a monopole antenna to the top of the helicopter. The second situation was interference and this was simulated by placing a second monopole antenna on the bottom of the helicopter. The final situation was penetration and this was simulated by changing some of the helicopters perfectly conducting structure to non-conducting.

Another method that can be used to solve Maxwell's equations is Finite Element Analysis (FEA). FEA was defined by Burnett (1987) as:

'a computer aided mathematical technique for obtaining approximate numerical solutions to the abstract equations of calculus that predict the response of physical systems subjected to external influences.'

More specifically the finite element method takes the area of interest and breaks it down into a number of elements, and then surrounds this area by various boundary conditions (eg Neumann and Dirichlet boundary conditions), voltage and current sources are then applied at various points in the grid. The voltage and current distribution across each element may be defined by a polynomial (eg linear or quadratic) of a trigonometric function. Next the governing equations for the problem are determined, and the nodal coordinates, material properties and the loading conditions are put into the equations. These individual equations for each element are then combined to obtain the system equation, which will describe the behaviour of the whole system. This will generally take the form:

$$[K] \{ U \} = \{ F \} \quad \text{(eq1.2.1)}$$

where:

[K] - is the stiffness matrix, which represents the shape and medium of the grid

{ U } - is the vector of unknown voltages and currents

{ F } - is the vector of the applied nodal forces

The above equation is the basis of the finite element method, and by solving equation 1.2.1 the unknown voltages and currents can be determined.

Rafinejad & Sabonnadiere (1976) showed how the finite element method could be applied to the modelling of an electromagnet to determine the magnetic fields generated by the magnet. A comparison between the FEA results and the experimental results showed that the finite element method could be used to provide accurate results to electromagnetic problems. Boglietti *et al* (1976) presented the finite element method and showed how it could be implemented into a package for electromechanical analysis. To demonstrate how well the package worked results for a brushless DC motor were presented. Khan & Costache (1989) applied the finite element method to determine the crosstalk between three parallel conductors and a ground plane on a pcb, for which a good correlation between the experimental and modelled results was found. They also presented a simple model to determine the radiation from five parallel conductors above a ground plane, and again good results which compared well with published results were obtained for this simple pcb model. Laroussi & Costache (1993) demonstrated that the finite element method could be used to determine the effects of crosstalk in parallel conductors on a pcb, they also showed how with one set of near field measurements that the finite element method could be applied to determine the overall field strengths in the near and far field regions. Dixon *et al* (1993) presented two finite element models, the first model showed how FEA compared to traditional methods, such as the Biot-Savart law. By simulating a single current carrying wire above a ground plane, a good comparison was found between the two methods in the near field, but as the field came closer to the metal walls the effects that these were having on the field became apparent in the FEA model but not in the Biot-Savart model. The

second model that was presented concerned a shielded room with a single radiating wire and two cabinets, and the FEA performed on it showed that it was possible to correctly predict the electromagnetic radiation within the room using a two dimensional finite element model.

Paul (1989b) showed how the electromagnetic radiation due to the common mode current, was much greater than the electromagnetic radiation due to the differential mode current. Due to this it was proposed that any radiation models that only took into account the differential mode currents would severely under predict the emissions. To show this Paul took a commonly used prediction model (the Hertzian dipole), and rearranged the equations to show that the contribution to the radiated emissions came predominantly from the common mode currents, and this can be seen in equations 1.2.2 and 1.2.3 below, which show the electric field strength due to the common and differential mode currents.

$$E_D = \left[\frac{Z_O\,\pi}{c2}\right]\frac{I_D\,f^2\,L\,D}{R} = 1.316\times 10^{-14}\,\frac{I_D\,f^2\,L\,D}{R} \qquad \text{(eq1.2.2)}$$

$$E_C = \left[\frac{Z_O}{c}\right]\frac{I_C\,f\,L}{R} = 1.257\times 10^{-6}\,\frac{I_C\,f\,L}{R} \qquad \text{(eq1.2.3)}$$

Where:

$$Z_O = \sqrt{\frac{\mu_O}{\varepsilon_O}} \qquad \text{(eq1.2.4)}$$

$$c = \frac{1}{\sqrt{\mu_O\,\varepsilon_O}} \qquad \text{(eq1.2.5)}$$

where:

c - speed of light (m/s)

D - line separation (m)

E - electric field strength (V/m)

f - frequency (Hz)

I - current (A)

L - line length (m)

R - distance of the field from the wire (m)

Z_o - intrinsic impedance (Ω)

ε_o - permittivity of free space (F/m)

μ_o - permeability of free space (H/m)

subscripts:

C - common mode

D - differential mode

o - free space

The model results were within 4dB of the measured results, which were taken from a simple setup consisting of two PCB tracks connected together with a 330Ω resistor and excited with a 10MHz oscillator.

Hubing & Kaufman (1989) presented a method of modelling electrically small products (that is the dimensions of the product are less than a wavelength). They take advantage of the fact that the circuits are inefficient sources of radiation and that the majority of the radiation comes from the power and signal cables. The model proposed only considers the product's cables, which are modelled as ideal dipole radiation sources. The drawback of this method is that it can only be applied to products that are electrically small.

Cerri *et al* (1993) proposed a model for the radiated emissions from pcb's, where the differential mode current and the common mode current are treated separately. The problem was set up as Green's function for the stratified media (eg tracking, dielectric and the air) and this allowed the authors to determine the Hertzian potential due to a current distribution in the pcb track. The results obtained using this method compared well with the measured results to within 4dB. They also present a method for

determining the maximum allowable current distribution as a function of frequency to comply with the CISPR EMC legislations.

Bergervoet (1994) showed that radiated emissions are generally from cables that are connected to the PCB's, rather than from the PCB's themselves. This radiated emission is predominantly due to the common mode currents. The reason for the common mode current being generated is the capacitive and inductive coupling of tracking on the PCB. The model for predicting the radiated emissions begins by predicting the parasitic capacitances and inductances on the board, and the results obtained compare well to the measured values.

1.2.3 Prevention of EMI

Even though EMI is currently a major problem with electrical devices, it is in fact possible to reduce the amount of emissions (both conducted and radiated) from a device, or to protect a particularly sensitive device from emissions from another source. There are four main ways of preventing EMI, these being:

1. Filtering.
2. Shielding.
3. Earthing.
4. Careful layout of components.

One of the common methods is filtering, which is generally used for the prevention of conducted interference, Goedbloed (1990), Christopoulos (1992b), Williams (1993), Hargis (1994), Conway (1994) and Taylor (1994), where the filter would be placed between the power cable and the device. Although filters are generally used to prevent conducted emissions, it is possible to prevent radiated emissions from cables by placing the filter between the device and cable, which actually prevents the common mode currents, which are the major source of radiated emissions.

Shielding is the most common defence against radiated emissions, Vance (1975), Goedbloed (1990), Christopoulos (1992b), Williams (1993) and Conway (1994), and will generally take the form of a piece of steel sheeting which is used to enclose the item

that needs protecting, for example the steel braiding on a piece of shielded cable. The one main problem with shielding is that complete shielding is very rarely possible, so some penetration of the shield is likely through small openings, access panels etc. Also it can prove expensive to shield complete products.

Earthing is a very important way of reducing electromagnetic emissions because it will provide a low impedance path for the current to return to its source, Christopoulos (1992b) and Williams (1993).

EMC design, Christopoulos (1992b), Macleod (1993) and Williams (1993), concerns the way a system is laid out. The amount of emissions from a system can be minimised by applying a number of simple rules when designing systems, the rules being:

1. All cables and pcb tracks should be classified and grouped together according to the signals that they are carrying, eg control cables should not be placed next to power cables.

2. When cables cross, they should be placed at right angles to minimise the mutual coupling between the cables.

3. The use of shielded cables or twisted wire pairs will help to minimise the amount of radiation generated by cables.

4. The shield of a shielded must be grounded, but pigtails should be avoided. Instead a 360^{O} contact between the shield and the ground should be used.

5. Switching frequencies and device rise times should be made as low as possible, because high frequencies and fast rise times are a common cause of radiation.

6. Any bonds between casings and ground should have a low impedance at radio frequencies.

7. Casings should be designed with care, as a noise voltage can be created if dissimilar metals are in contact.

1.3 Structure and Content of Thesis

The thesis is broken down into 8 chapters and 8 appendices, each chapter and appendix is summarised as follows:

Chapter 2:

Presents a brief history of EMC from the late 1800's to the present day, and the legislations that are currently being implemented to govern the levels of electromagnetic emissions from all electrical products. A brief explanation of the basic concepts concerning EMC is also presented, which concentrates on sources of emissions and conducted and radiated emissions. The chapter is concluded with details of the testing methods that can be employed to measure the conducted and radiated emissions.

Chapter 3:

This chapter presents a circuit model of the Eurotherm 583 drive that was set up in the SABER simulator to predict the conducted emissions and also to generate the sources that would be used to predict the radiated emissions.The model took account of all the elements that made up the drive system during the measurement of the conducted emissions, these elements being the power electronics side of the drive, the shielded cable that connected the drive to the motor, the induction motor used in all the tests, the line impedance stabilising network and the parasitic capacitances that were present in the system. The conducted emissions were modelled using the SABER model in the frequency range 150kHz to 16MHz and were found to have an error of +/-6dB when compared to the measured results.

Chapter 4:

This chapter describes the test rig used to measure the radiated emissions from the drive, along with the procedure used in making the measurements. The results obtained for the radiated emissions are presented, with the antenna in both the horizontal and

vertical positions. The results with the antenna in the vertical and horizontal positions are then combined to give the modulus of the radiated emissions. Finally a number of problems associated with the test rig and its inability to produce repeatable results are identified.

Chapter 5:

This chapter presents a two-dimensional finite element model of the Eurotherm 583 drive that was set up in the finite element package PC-OPERA. The model took into account the areas of the drive that were most likely to radiate, as well as the structure of the test rig used to measure the radiated emissions. The model was excited with the sources that had been previously generated using the SABER model. The radiated emissions that were generated using the finite element were found to compare with the measured values to within +10dB and -6dB. It was also determined that the majority of the radiation was coming from the shielded cable, so a second model was run which only took account of the shielded model which was excited with the current that the motor would see and also the common mode currents that were flowing in the shield, and again it was found that the radiated emissions could be predicted to within +10dB and -6dB of the measured results.

Chapter 6:

This chapter presents the Transmission Line Matrix (TLM) modelling method as a way of predicting the radiated emissions from the 583 drive. The first part of the chapter presents the theory for both two and three-dimensional TLM models. The second part of the chapter develops a three-dimensional TLM model for the 583 drive based on the shielded cable which connected the drive to the motor, as the finite element model had previously showed that this was the major source of the radiation from the drive. It was not possible to excite the cable model with the common mode currents so the only source that was used was the current that the motor would see. The results from the TLM model were compared to the previously generated finite element model, and it was found that the two methods were comparable to within 5%. It was also explained that the TLM method is not an ideal method for predicting the radiation profiles from variable speed drives, but it may be more useful for the development of immunity

models.

Chapter 7:

This chapter discusses the work that is presented in this thesis and also draws a number of conclusions from the discussion. A number of overall conclusions for the work were drawn, these being:

1. That it is feasible to predict the conducted emissions to within +/-6dB of measured values using circuit modelling techniques.

2. Circuit modelling techniques can also be used to generate current and voltage sources for the use in predicting the radiated emissions.

3. Theory has shown that it is possible to predict the radiated emissions to within +10dB and -6dB of measured values using two-dimensional finite element theory.

4. The majority of the radiation from the drive is in fact being generated by the shielded cable which connects the drive to the motor.

5. The transmission line matrix modelling method is currently not a suitable method for predicting the electromagnetic radiation profiles from variable speed drives, due to the difficulty of presenting the sources in a suitable format.

6. A complete methodology has been developed to predict the electromagnetic radiation, in terms of the conducted and the radiated emissions, from variable speed drives.

Chapter 8:

This chapter presents a number of areas of future work, which have been highlighted throughout the duration of the project and were outside the realms of the project. These are:

1. Circuit modelling.
2. Measurement techniques for radiated emissions.
3. Prediction of radiated emissions.

4. Improvement of the TLM modelling method.

5. Immunity modelling.

Appendix 1:

Contains details of the devices modelled during the project.

Appendix 2:

Contains a brief description of the SABER circuit simulator and the two-dimensional finite element package PC-OPERA.

Appendix 3:

Contains the circuit diagrams of the Eurotherm 583 drive and the LISN used to make the conducted measurements.

Appendix 4:

Defines the default values used in the IGBT and diode models in the SABER circuit simulator.

Appendix 5:

Contains all the programs that were run in the SABER circuit simulator.

Appendix 6:

Describes the method of graded meshes in transmission line matrix modelling.

Appendix 7:

Contains both two and three-dimensional TLM models.

Appendix 8:

Presents the papers that were published throughout the project.

1.4 Equipment Investigated

There was one main piece of equipment that was investigated in the project, and that was the Eurotherm 583 induction motor drive, and this was connected to a 3 phase induction motor via a 5 metre length of shielded cable. Full details of drive and the motor can be seen in appendix 1.

Chapter 2

General Background

2.1 Introduction

In the first chapter the literature that was relevant to this project was presented. In this chapter a brief history of EMC is presented along with additional information on the EMC directives that are due to come into force at the beginning of 1996. Also presented are some of the basic concepts of EMC along with an explanation of the types of tests that can be performed to measure the conducted and radiated emissions, in compliance with the EMC legislations.

2.2 Historical Background of EMC

The history of EMC can be traced back to when Marconi performed his first spark-gap experiment towards the end of the 1800's, and in 1901 he provided the first transatlantic transmission lines. At this time the only receptors being used were radio receivers, of which there were few and these were placed far enough apart so the correction of interference was fairly simple.

It was towards the 1920's that papers started to appear on the subject of EMI. The radio receivers of the time were rather prone to the affects of EMI whether it was from an external source or from within the receiver itself. Major problems from EMI did not really start to occur until the 1930's when the usage of such items as electric motors, electric railroads and electric signs became more common.

At the time of the second world war the use of such equipment as radios, navigation devices and radar had begun to grow, and as a consequence, so did the number of instances of interference between such devices. The majority of these problems were solved by merely changing the operating frequencies of the equipment.

The real explosion in problems concerning EMI came with the invention of the bi-polar transistor in the 1950's, the integrated circuit (ic) in the 1960's and the microprocessor chip in the 1970's. The number of people wanting to use the frequency spectrum has also been increasing since the 1950's and this in itself has caused interference problems

and still does today, but to a much greater extent.

Although all of these events have produced more interest in EMC, the one event that has promoted the most interest was the introduction of digital signal processing and computation in the 1960's. At this time the expense and space required for such digital systems was very high. In the 1970's the integrated circuit changed this and the expense and space required was reduced such that digital systems started to appear in the home. Also the amount of deliberate man-made electromagnetic signals in the form of television, radio and mobile phones has greatly increased in the last few years. This increase in the use of digital systems continues, and as a consequence of this rise the density of noise sources rich in spectral content has risen to such an extent that EMI problems have begun to rise. For these reasons legislation governing the amount of emissions from electrical devices was needed. Military equipment has been governed by such legislations for a number of years now, also all products sold in the US are governed by the Federal Communications Commission (FCC). As mentioned in the introduction a new European directive governing the emissions of electrical devices marketed in the EEC is due to come into force at the beginning of 1996.

2.3 The EMC Directive

As mentioned in the preceding section a new European EMC directive, Green (1994), Simms (1992) and The UK Department of Trade and Industry (1992), is due to come into force at the beginning of 1996, and this legislation (EC directive 89/336/EEC) states that any electrical equipment that is to be marketed in the EEC, must be constructed so that:

1. The electromagnetic disturbance it generates does not exceed the level that prevents other pieces of electrical equipment from operating correctly.
2. The piece of equipment has an adequate level of immunity to electromagnetic disturbances, to allow it to operate correctly.

Even though this new legislation only applies to products sold within the EEC, all electrical products sold within the US must comply with the directives laid down by

the FCC (Federal Communications Commission) which is an equivalent directive to the ones which are due to be applied within the EEC.

There are two sets of limits concerning conducted and radiated emissions, and these are separated into class A and class B devices. Class A devices are destined for residential, commercial and light industrial use, and the test measurements can be made either on site or at a test site. Class B devices are for use in an industrial environment and the measurements should be made on a test site.

Figure 2.1 shows the limits laid down, in a draft standard for power drive systems (IEC 22G-WG4 (Cv) 5, 12th-15th October 1993), for both radiated and conducted emissions, where the emissions from the drive system must be below the selected limit line. The limits are for low power systems where the current is below 25A.

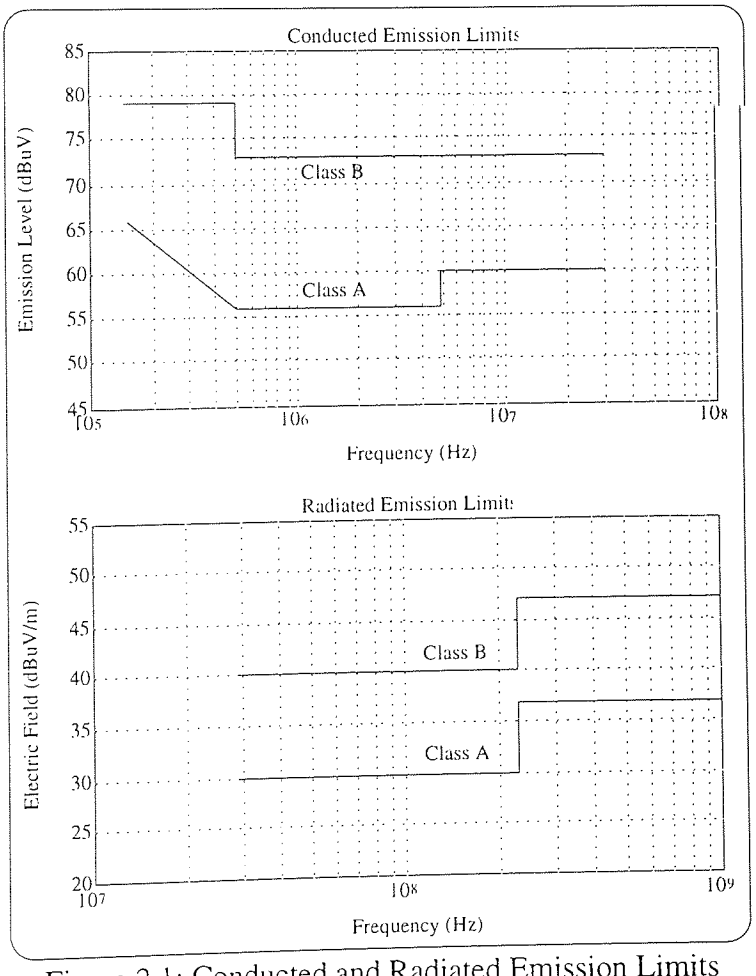

Figure 2.1: Conducted and Radiated Emission Limits

2.4 Basic Concepts

A standard definition of electromagnetic compatibility can be stated as follows:

"the ability of a device, equipment or system to function satisfactorily in its electromagnetic environment without introducing intolerable electromagnetic disturbances to anything in that environment" (IEC 1989)

Going on from this definition it can be seen that EMI can be generated from inside or outside the equipment as stated by Christopoulos (1992a), and Figure 2.2 shows these paths and how they interact with the equipment, in the case of a motor and its inverter drive system.

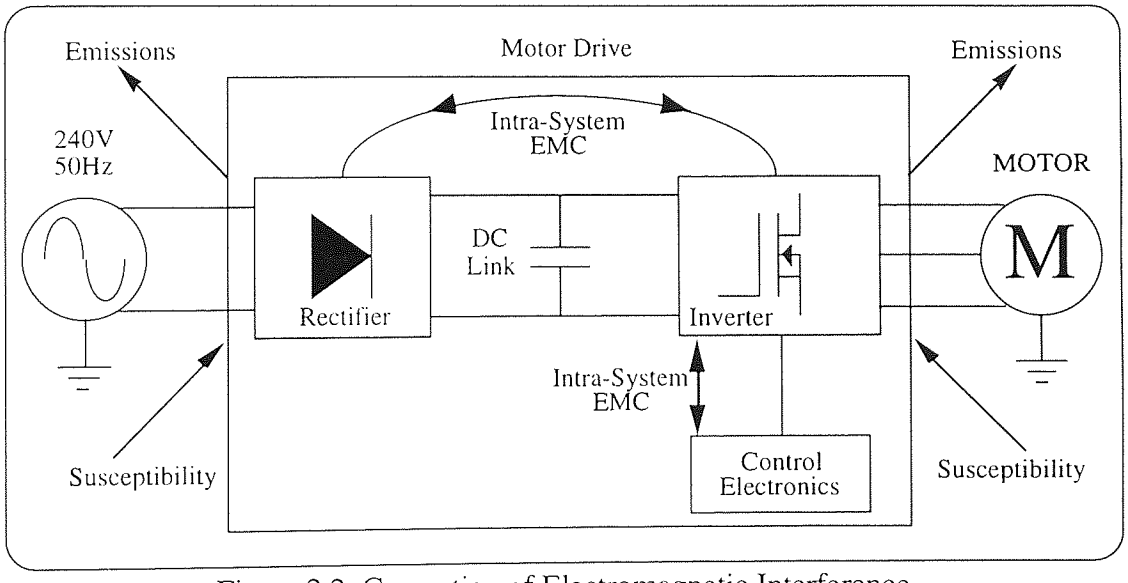

Figure 2.2: Generation of Electromagnetic Interference

There are a large range of sources from which electromagnetic interference can be generated, and this range of sources can be split into two distinct classes of noise the first being emissions due to natural sources and the second is due to man made sources.

The terrestrial electromagnetic environment as discussed by Christopoulos (1992a) and Degauque & Hamelin (1993) is characterised by a magnetic field (H) of about 30 A/m, and an electric field (E) of about 100 V/m. Both of the values given for the natural fields above are approximate values and will tend to vary due to the weather and

location. The next natural phenomena is lightning which tends to have very high frequency signals and peak currents of around 200 kA, Figure 2.3 shows the field strength due to a lightning strike to ground.

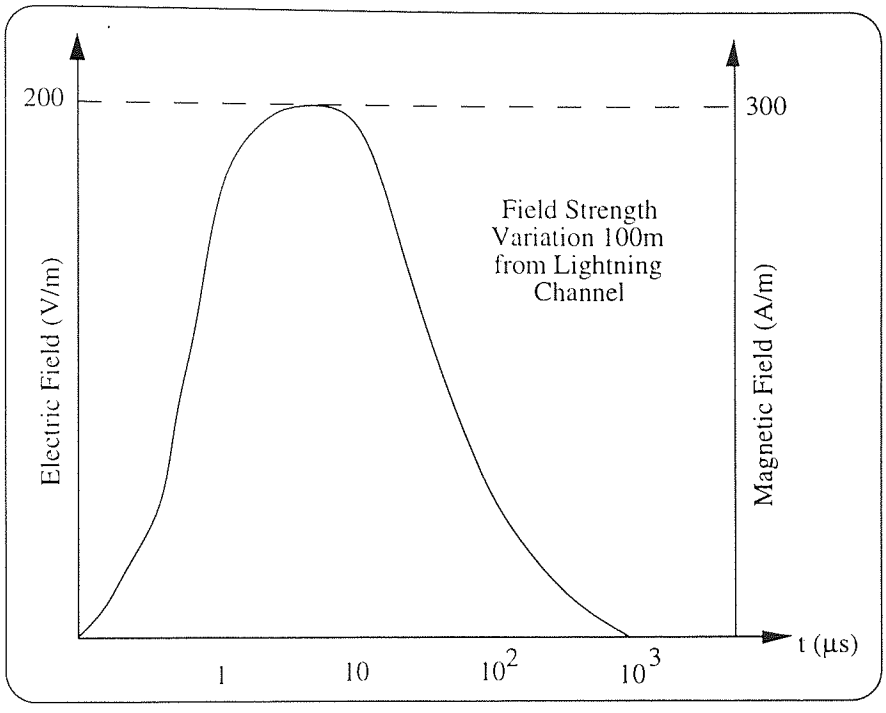

Figure 2.3: Field Strength due to a Lightning Strike to Ground

The final types of natural phenomena are all related to the conductors in a circuit, and the first type is known as thermal noise, Conner (1982) and Davies (1993), which exists due to the movement of electrons, which produce an electric current that has a random amplitude, phase and time. This noise is known as thermal noise because the rms value of the current is temperature dependent, the thermal noise voltage (V) is given by:

$$V = \sqrt{4\,k\,T\,B\,R} \qquad \text{(eq2.4.1)}$$

where:

T = Absolute Temperature (K),

R = Resistance (Ω)

B = Bandwidth (Hz)

k = Boltzmann's Constant (1.38×10^{-23} J/K)

The reason that thermal noise is important, is that it sets the level for which a signal can be detected without integration, because any signal which has an amplitude less than this level will be lost in the noise.

The second type of noise, associated with conductors is known as shot noise, Davies (1993). This is caused by the clustering of charge carriers as they cross potential barriers such as a p-n junction. Shot noise current (i) is given by:

$$i = \sqrt{2 e I B} \qquad \text{(eq2.4.2)}$$

where:

e = electronic charge (C)

I = mean current (A)

B = Bandwidth (Hz)

The final natural noise source is known as flicker noise, Davies (1993), which is caused by impurities and irregularities in the surface material of semiconductors, and results in the fact that the noise is greatest at lower frequencies due to the fact that the noise is a function of:

$$V_f \alpha \sqrt{\frac{I}{f}} \qquad \text{(eq2.4.3)}$$

The electromagnetic environment due to human activities is extremely wide ranging. Therefore only a few EMI sources due to power networks will be discussed. A major area of interference associated with power networks is high-frequency switching or more importantly high rise times. These can generate a high rate of change of current and subsequently a high rate of change of voltage. Generally the higher the frequency and the quicker the rise times the higher the level of interference. Another reason for

EMI in power networks is that loads often exhibit non-linear characteristics and examples of this are electronic converter equipment, transformers and reactors, and these non-linearities introduce harmonics of the mains frequency in power supplies.

There are two basic types of electromagnetic emissions, the first being conducted emissions and the second being radiated emissions These will be discussed separately in the following sections.

2.4.1 Conducted Emissions

An emission can be classed as being conducted when interference sources inside a piece of equipment or its associated power supply are coupled onto the power cable that supplies the equipment. The coupling from the equipment to the power cable can be either inductive (magnetic) or capacitive (electric), and Figure 2.4 shows how this coupling may occur. Where there is capacitive coupling between the ground plane and the two circuits as well as between the coils of the transformer inductive coupling is also present on the power cable.

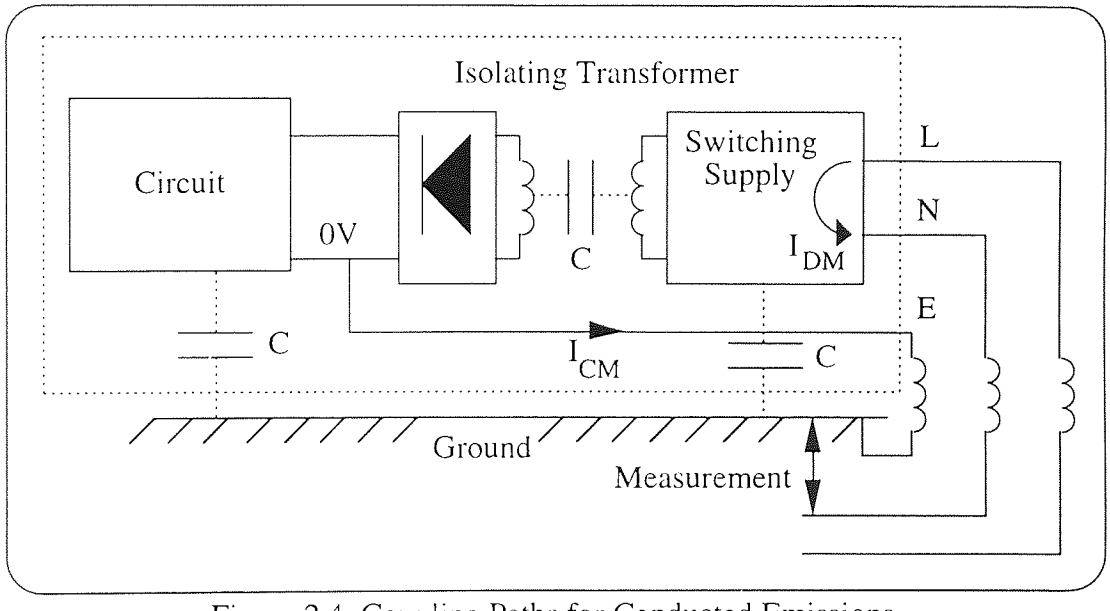

Figure 2.4: Coupling Paths for Conducted Emissions

Conducted emissions may appear as either differential mode noise (symmetrical line-to-line noise) which will appear between live and neutral wires or between the signal

wires, or as common mode noise (asymmetrical line-to-earth noise) which will appear between either the live, the neutral or the signal wires and the earth wire, or it can appear as a combination of the two. In terms of magnitude, phase and direction, it can be said that a differential mode current has equal magnitudes, and direction but are 180^{o} out of phase with the current returning on the second wire (either neutral or a signal wire). Common mode currents which are directed to the right in Figure 2.4 can be said to have equal magnitudes and phases. Figure 2.5 shows the difference between differential and common mode currents.

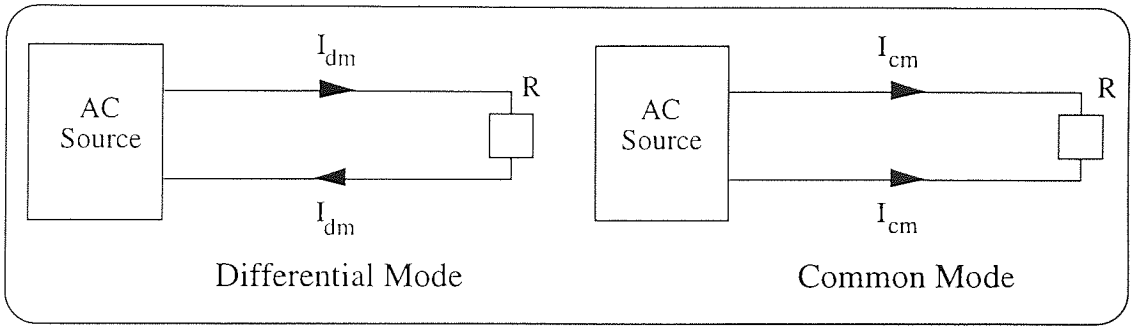

Figure 2.5: Differential and Common Mode Currents

Differential mode noise is generally associated with low frequency switching noise from the power supply, whereas common mode noise is generally due to high frequency switching components, internal circuit sources or inter-cable coupling. Conducted emissions are generally more troublesome than radiated emissions.

2.4.2 Radiated Emissions

As the name suggests radiated emissions are the transport of electromagnetic energy through space and are far more complex than conducted emissions. The current EMC legislations only consider the field strengths in the far field, that is when:

$$d > \frac{\lambda}{2\pi} \qquad \text{(eq2.4.4)}$$

where:

d - distance from the equipment (m)

λ - wavelength (m)

Also in the far field there is a fixed relationship between the electric field (E) and the magnetic field (H), which is known as the wave intrinsic impedance (Z_0):

$$Z_0 = \frac{E}{H} = \sqrt{\frac{\mu_0}{\varepsilon_0}} = 377\ \Omega \qquad \text{(eq2.4.5)}$$

where:

E - electric field (V/m)

H - magnetic field (A/m)

μ_0 - permeability of free space ($4\pi \times 10^{-7}$ H/m)

ε_0 - permittivity of free space (8.854×10^{-12} F/m)

The following equations (eq2.4.6 to eq2.4.7) characterise the electric and magnetic fields at a point (p), due to a Hertzian dipole, Kraus (1992). The Hertzian dipole can only be applied when the following assumptions are correct:

1. The length of the dipole is infinitesimally small.
2. The dipole carries a phasor current that is assumed to be the same magnitude and phase at all points along the dipole.

The spherical coordinate system used in the Hertzian dipole is shown in Figure 2.6.

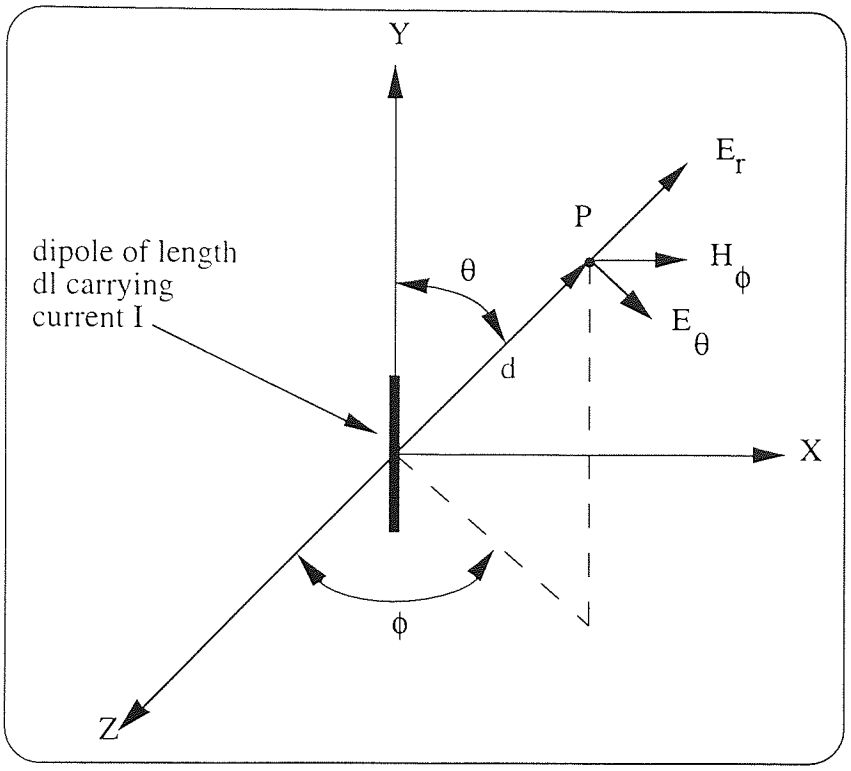

Figure 2.6: Relation of the Dipole to the Spherical Coordinates

As the only area of interest is the far field, the electric and magnetic fields at the point P due to a current flowing in the dipole are (Williams (1992)):

$$E_\theta = \frac{j \beta I l \sin\theta}{4 \pi d} \sqrt{\frac{\mu_0}{\varepsilon_0}} e^{-j \beta d} \qquad \text{(eq2.4.6)}$$

$$H_\phi = \frac{j \beta I l \sin\theta}{4 \pi d} e^{-j \beta d} \qquad \text{(eq2.4.7)}$$

Where:

$$\beta = \frac{2 \pi}{\lambda} \qquad \text{(eq2.4.8)}$$

where:

I - current flowing in the dipole (A)

l - length of the dipole (m)

d - distance from point P to the dipole (m)

λ - wavelength (m)

As was said previously the above equations relate only to the far field, and the electromagnetic wave will decay as a function of 1/r.

The Hertzian dipole can be applied to any electromagnetic problem to determine the field strengths in the far field, providing that sufficient information is known about the currents flowing in the system

If the wave is in the near field the coupling is not truly radiative but a mixture of capacitive and inductive coupling, so the wave impedance will vary depending on whether the electric or the capacitive coupling is dominant, and these will decay as $1/r^2$ if the dominant field is inductive and as a function of $1/r^3$ if the dominant field is capacitive.

In practice it is not feasible to apply the Hertzian dipole theory to real problems as it cannot take account of other factors which may effect the fields, for example shielding.

2.5 Testing Methods

There are a number of different tests that can be performed to ensure that compatibility is achieved, and these are detailed below:

1. Conducted Emissions Test,

   This is a generation test in which the conducted emissions are measured across a 50Ω impedance connected between the power cable and ground and is measured in the frequency range 150kHz to 30MHz.

2. Electrostatic Discharge Tests,

   This is an immunity test in which 8kV is discharged to the earthed case of the EUT (Equipment Under Test) and other accessible external parts.

3. Radiated Emissions Test,

This a generation test in which the radiated emissions from the EUT are measured on an open field test site over the frequency range 30MHz to 1GHz.

4. Radiated Electromagnetic Field Disturbance Test,

This is an immunity test in which the EUT is subjected to a frequency sweep of radio frequencies at a field strength of 10V/m, and covers the frequency range 27MHz to 500MHz.

As the models being developed in this thesis are only concerned with radiated and conducted emissions, these will be the only tests discussed here.

2.5.1 Conducted Emissions

Out of the two types of emissions, conducted emissions are easier to measure than the radiated emissions. The reason for this being that the test set-up needed to measure conducted emissions is much simpler than the test set up required for radiated emissions, and also that a conducted emission is a current flowing in a wire rather than an electromagnetic wave travelling through space. The type of test set up that is required has been specified by CISPR (International Special Committee for Radio Interference), and Figure 2.7 shows the CISPR layout for conducted tests.

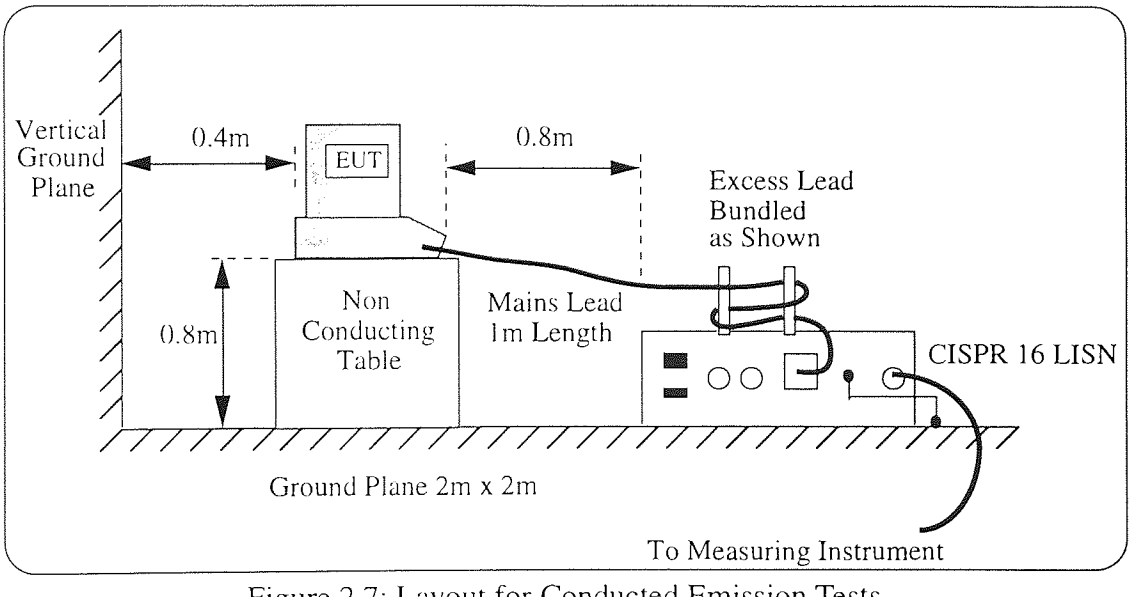

Figure 2.7: Layout for Conducted Emission Tests

The purpose of the LISN (Line Impedance Stabilising Network), as discussed by Lin & Chen (1994) and Williams (1994), is to provide a defined impedance (50Ω) at radio frequencies across the measuring device, which enables the measuring point to be coupled to the test instrumentation (either a spectrum analyser or a dedicated EMC receiver), as well as isolating the test circuit from any unwanted interference signals on the mains supply.

A second way of measuring the conducted emissions is to use an absorbing ferrite clamp, Williams (1993), Marvin (1991) and Jackson (1989). The ferrite clamp is made up with a current transformer using three ferrite rings, which are split to allow the cable to be inserted. This is followed by a series of ferrite rings which form a power absorber and impedance stabiliser, and the whole device clamps around the cable to be measured. Figure 2.8 shows how a ferrite clamp could be used to measure the conducted emissions of a cable, the clamp would be moved along the cable until the maximum value of the current flowing in the cable was found.

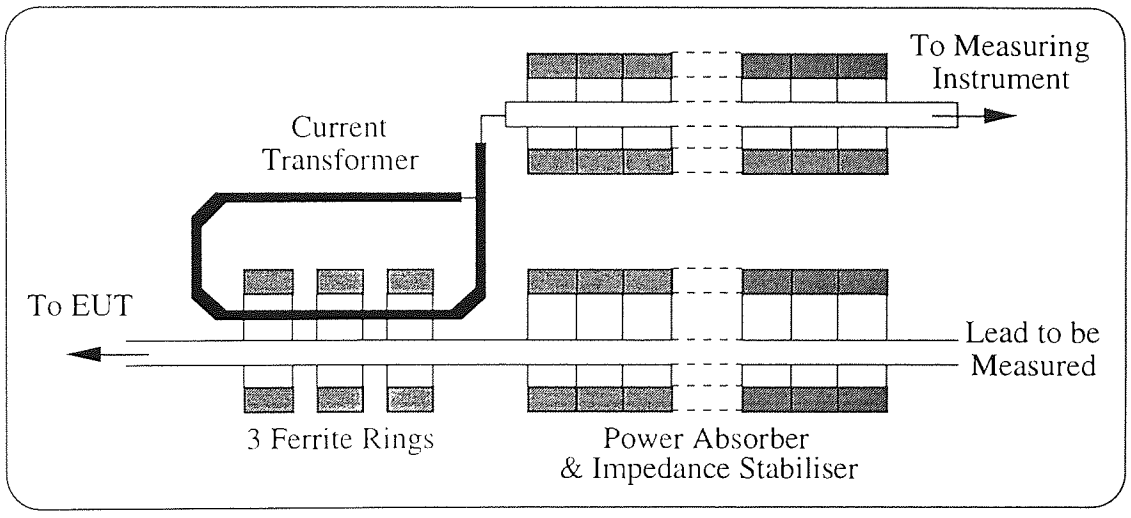

Figure 2.8: The Absorbing Ferrite Clamp

There are three types of measuring instrument, as argued by Cook (1990), that can be used to observe the electrical signals that are obtained from the LISN or the ferrite clamp. Ideally a device is required that can display a three dimensional image with axis showing time, frequency and amplitude. To the authors knowledge no such device exists. The first practical means is to use an oscilloscope. The signals will be observed

in the time domain, and as electromagnetic emissions cannot be characterised properly with just time domain information this is not an ideal solution. It is possible to display frequency and magnitude and currently there are two devices that can do this, the first being the spectrum analyser and the second being the dedicated EMC receiver. The problem with the spectrum analyser is that to meet the requirements of CISPR 16, a notch filter must be added between the analyser and the equipment under test, and this obviously increases the price of the analyser, whereas the dedicated EMC receiver the notch filter will be built into the receiver. The EMC receiver is likely to have a better bandwidth than a spectrum analyser. The problem with the dedicated EMC receiver is that typically two or more receivers are needed to cover the complete EMC spectrum (9kHz-1GHz).

2.5.2 Radiated Emissions

As was stated in the previous section radiated emissions are harder to measure than conducted emissions. The reason for this being that the emissions rely heavily on any conducting material surrounding the source, eg metallic furniture. This means that radiated emissions should be measured in free space. There are three ways of achieving this, the first being to use an Open-Area Test Site (OATS) discussed by Goedbloed (1990) and Williams (1994). The EMC legislations generally stipulate that all radiated emissions testing should be done on an open-area test site, and Figure 2.9 shows the CISPR open-area test site.

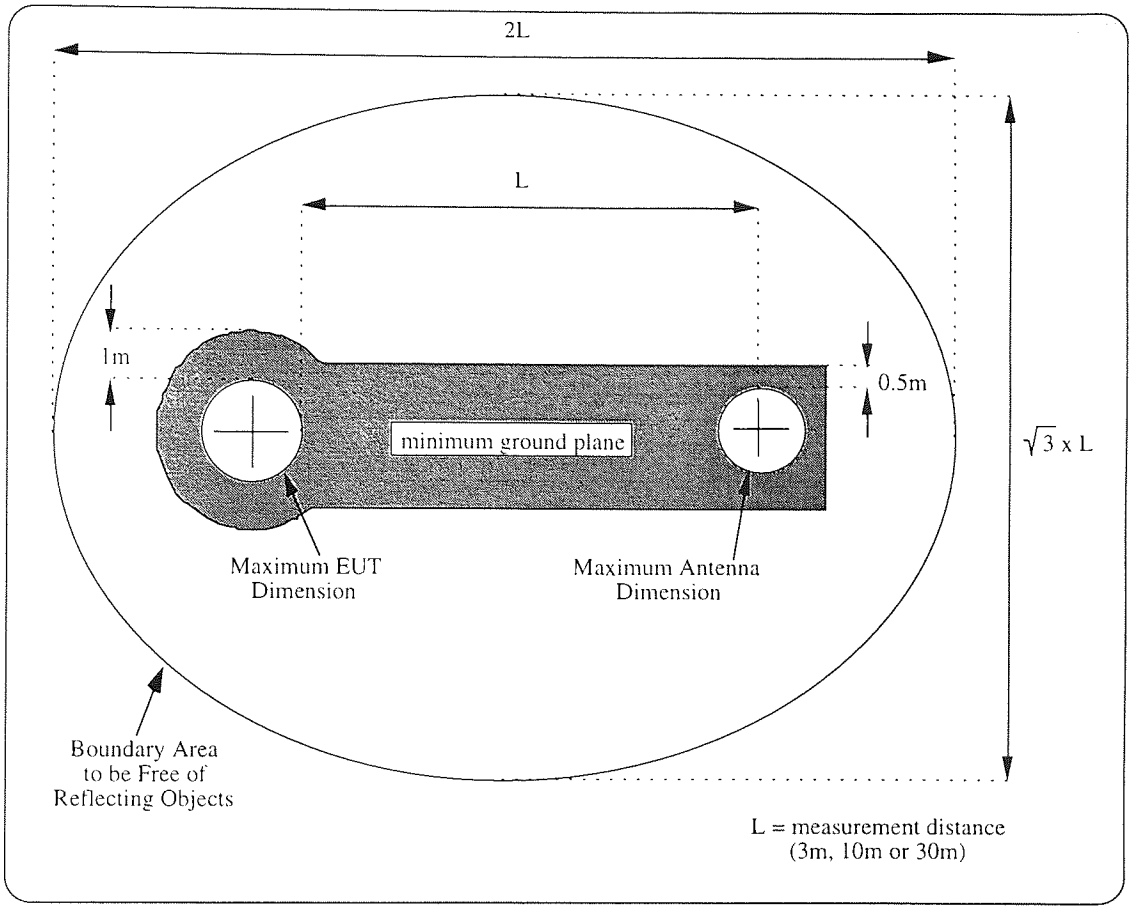

Figure 2.9: The CISPR Open Area Test Site

The above diagram shows the minimum requirements for an OATS, but for repeatable results it is advisable to ensure that the surrounding area is free from all reflecting objects. This implies that the measuring and control equipment needs to be situated well away from the test site. As with the conducted emissions the measuring device is either a spectrum analyser or a dedicated EMC receiver.

The second way is to use a shielded chamber as discussed by Goedbloed (1990) and Williams (1994). A problem with shielded chambers are that the chamber will have a number of resonant frequencies, due to the reflections from the walls, and the larger the room the lower the resonant frequencies will be. These resonances can be damped by lining the room with absorbing material, generally carbon loaded foam shaped into pyramidal sections which reduce the reflections from the walls or ferrite tiles. A chamber is said to be anechoic if all the walls and the floor are lined, but if they are only partially lined then it is said to be semi-anechoic. A problem with lining a chamber with

absorbing material is that the physical size of the room is reduced, and also that the material used is expensive and to fully line a chamber can double the unlined cost. A typical screened room can be seen in Figure 2.10. However a shielded chamber can be used to make a fast sweep of a product to determine the frequencies where the emissions are too high, and then to use an open area test site to measure at the frequencies highlighted during the fast sweep.

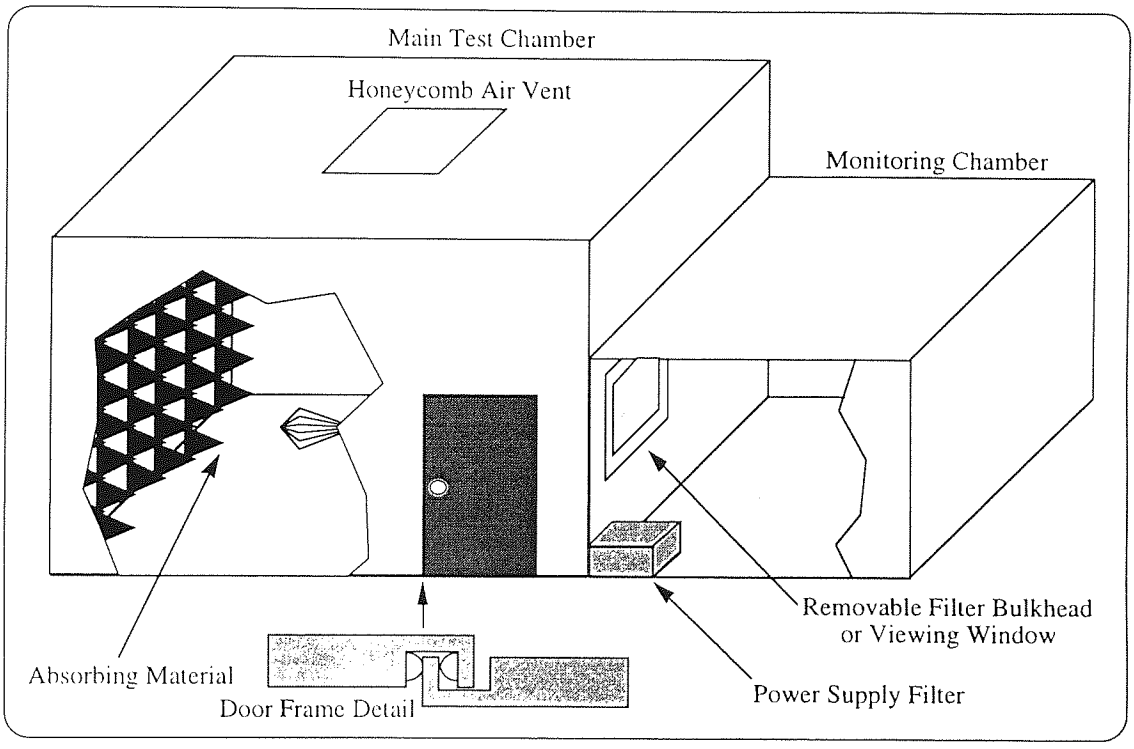

Figure 2.10: Structure of a Screened Room

The final method that can be used to measure radiated emissions is to use a Gigahertz Transverse Electromagnetic Mode (GTEM) cell. The GTEM cell is a pyramid shaped metallic structure in the form of a linearly flared rectangular 50Ω transmission line, which is terminated with a 50Ω impedance. Figure 2.11 shows the structure of a GTEM cell. The inner conductor is angularly offset from the centre of the structure to provide as much space as possible for the EUT. The load at the far end of the cell provides a 50Ω termination impedance over the complete frequency range required for EMC work (ie dc to 1000MHz). The resistive load provides the 50Ω impedance up to

100MHz and the absorber load provides the 50Ω impedance above 100MHz. The output (radiated emission) is measured at the point of the GTEM cell.

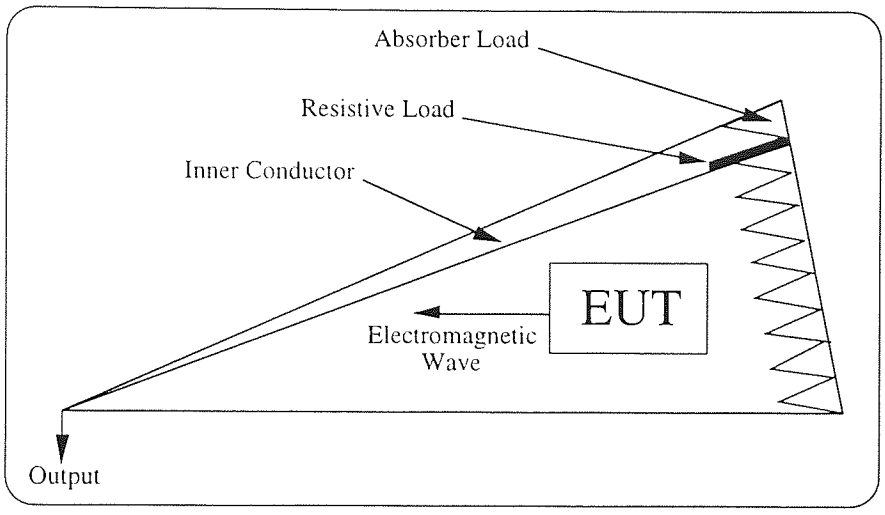

Figure 2.11: Structure of the GTEM Cell

A problem with the GTEM cell is that its structure limits its use to the testing of devices that are relatively small, although the test area can be increased by moving the rear wall of the cell. A distinct advantage of the cell is that it can be installed in a laboratory and does not require a large amount of space like the shielded chamber, and also that its use is not weather dependent like an open area test site.

2.6 Summary

A brief history of EMC has been presented from the late 1800's to the present day together with the legislations that are currently coming into practice to govern the levels of EMC from all electrical products. A brief explanation of the basic concepts concerning EMC is presented, which concentrated on sources of emissions and conducted and radiated emissions. The chapter is concluded with details of the testing methods that can be used to determine the conducted and radiated emissions from any piece of electrical equipment.

Chapter 3

Circuit Modelling

3.1 Introduction

The first priority of this research was the setting up of an accurate circuit model from which two things could be determined. The first thing being the current and voltage waveforms at various points in the circuit, which were ultimately used as sources in the model for the prediction of the radiated emissions (see chapters 5 and 6). The second thing to be determined was the conducted emissions on the power cable.

Much of the theory behind circuit models is based on the solving of equations based on theories such as Thevenin's and Norton's as well as Kirchoff's voltage and current laws. If applied correctly these will generate a solution for the voltages and currents in a circuit. Although it is relatively easy to apply these theorems, it can be a time consuming method when the circuits start to become complex. Computer packages such as SPICE (Simulated Program with Integrated Circuit Emphasis), Rashid (1993), and SABER, Analogy UK Ltd (1989), were developed to solve these types of problems. The obvious advantage of using these packages is their time saving abilities, but the use of these packages also makes it possible to perform a range of different analyses, for example:

1. Evaluation of the effects of variations in such elements as resistors, transistors and transformers.
2. Assessment of performance improvements or degradations.
3. Evaluation of the effects of noise in individual components and signal distortion.
4. Sensitivity analysis to determine the permissible bounds due to tolerances on every element value.
5. Fourier analysis or Fast Fourier Transforms (FFT's).
6. Evaluation of the effect of nonlinear elements on circuit performance.
7. Optimisation of the design of electronic circuits in terms of circuit parameters.

Computer based solvers are very powerful tools in the analysis of circuits. So for the remainder of this chapter all the circuit models will be solved using the SABER simulator, a description of the SABER simulator can be seen in appendix A2.1.

The circuit model that was developed consisted of the five elements that made up the drive system during the experimental work, these five elements being:

1. The 583 drive.
2. The shielded cables between the 583 drive and the induction motor.
3. The LISN (Line Impedance Stabilising Network).
4. The induction motor.
5. The circuit parasitics.

The generation of the models for these five elements is presented in the following five sections, along with experimental data to confirm the validity of the circuit models.

3.2 The Drive Model

When the drive was modelled in the circuit solver, there was no point in including all 400 plus component that were contained within the drive as this would have resulted in a highly complex model which would take long periods of time to solve. On inspection of the drive it was obvious that it could in fact be broken down into two areas. These being:

1. The power electronics, or high voltages and currents.
3. The control electronics, or low voltages and currents.

Due to the nature of radiated and conducted emissions, which were discussed in the in the previous chapter, it was decided that it would mainly be the high currents and voltages that would contribute to the emissions, so only the power electronics side of the drive was modelled along with the control signals that would have been generated by the control board. Figure 3.1 shows a block breakdown of the power electronics side of the drive. A detailed circuit diagram is shown in appendix A3.

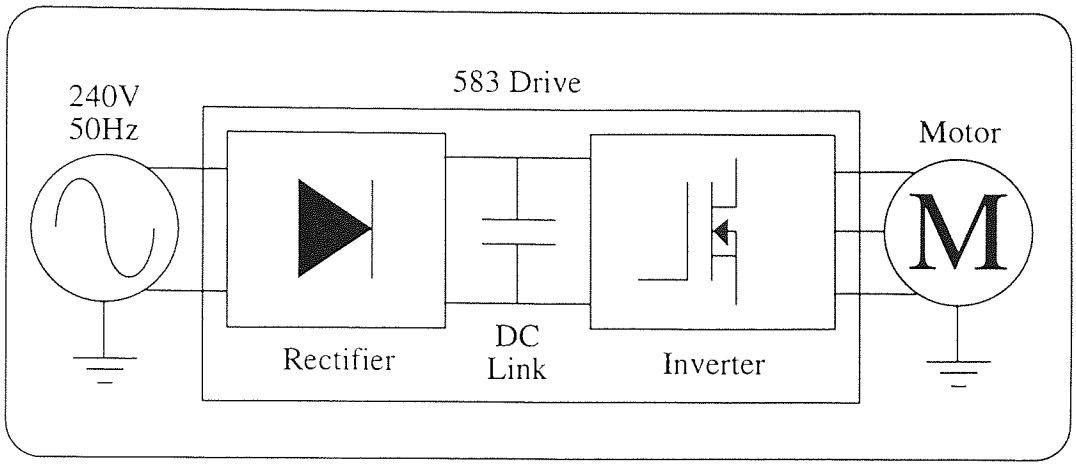

Figure 3.1: Power Electronics of the 583 Drive

On setting up of the drive model, it became apparent that there were several components that could not be taken from SABER's extensive template library of circuit elements. These components were specifically the IGBT's (Insulated Gate Bi-polar Transistors) and the diodes. All the other components, the resistors, capacitors and the inductors could be taken from the template library and a value assigned.

The problems with the IGBT's and diodes were not that the SABER template could not be used, but more specifically that the parameters required could not simply be read off a data sheet.

The SABER model for the IGBT which uses the model developed by Hefner & Blackburn (1988) and Mitter *et al* (1993), actually employs 30 different parameters such as the capacitance between the emitter and the base. The problem being as previously said is that the majority of these parameters are not on standard manufactures data sheets, also they could not be easily measured. So the IGBT model was generated by picking the parameters that could be determined from the data sheet and leaving the rest of the parameters at the default levels, the default levels can be seen in appendix A4.1. The parameters that were chosen being:

1. MOSFET channel threshold voltage - 5.9V
2. empirical parameter that models the MOSFET transconductance reduction due to a transverse electric field - 0.02
3. intrinsic collector series resistance - 0.15Ω

4. gate source capacitance - 900pF

A comparison of the model results for the IGBT's when compared to the data sheet results can be seen in the following graphs, Figures 3.2 to 3.5. As can be seen from these results the SABER IGBT model results correlate well with the data sheet results to within 1V.

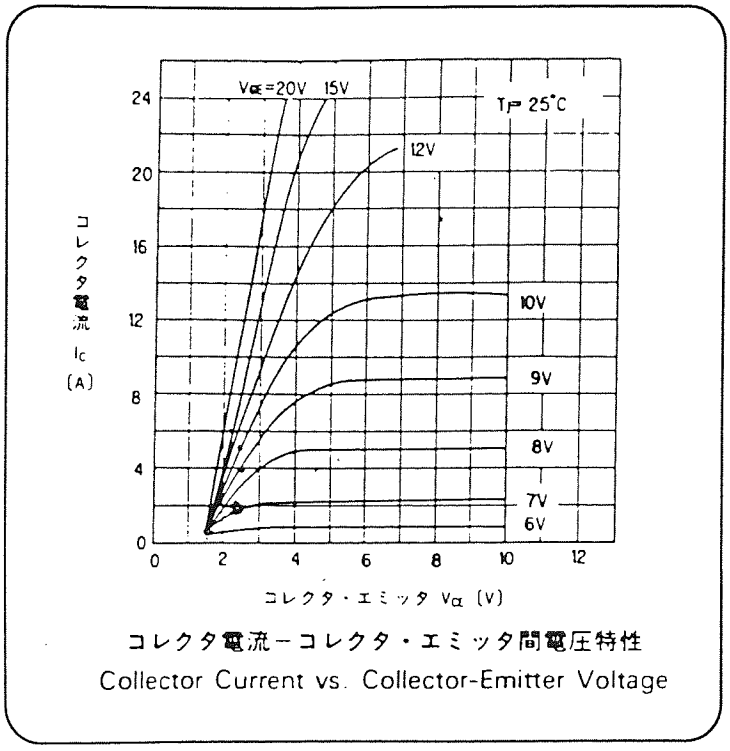

Figure 3.2: IGBT Data Sheet Values

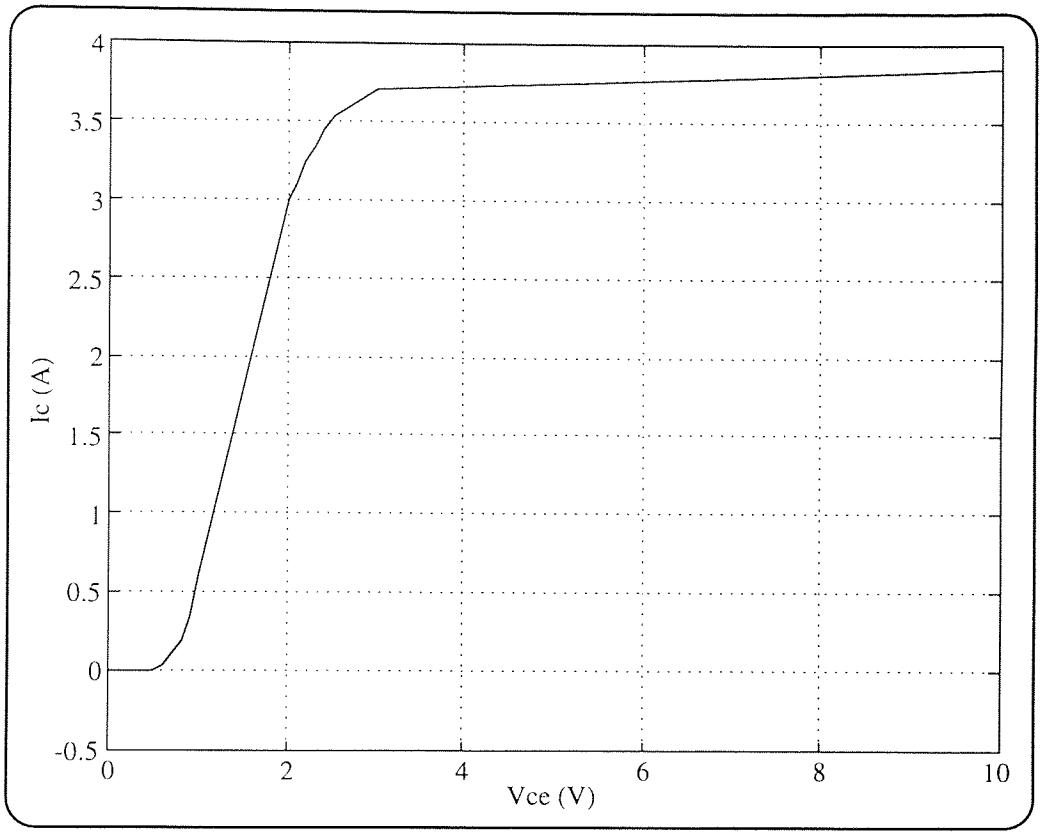

Figure 3.3: IGBT Model Results (V_{ge} = 8V)

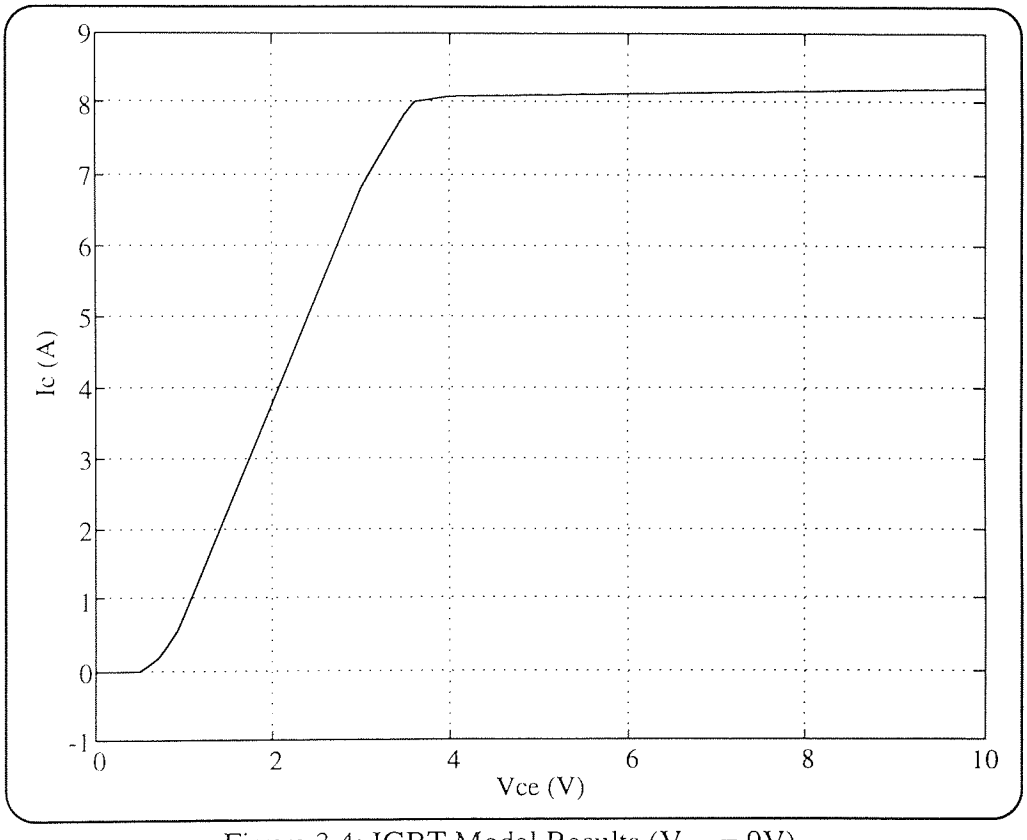

Figure 3.4: IGBT Model Results (V_{ge} = 9V)

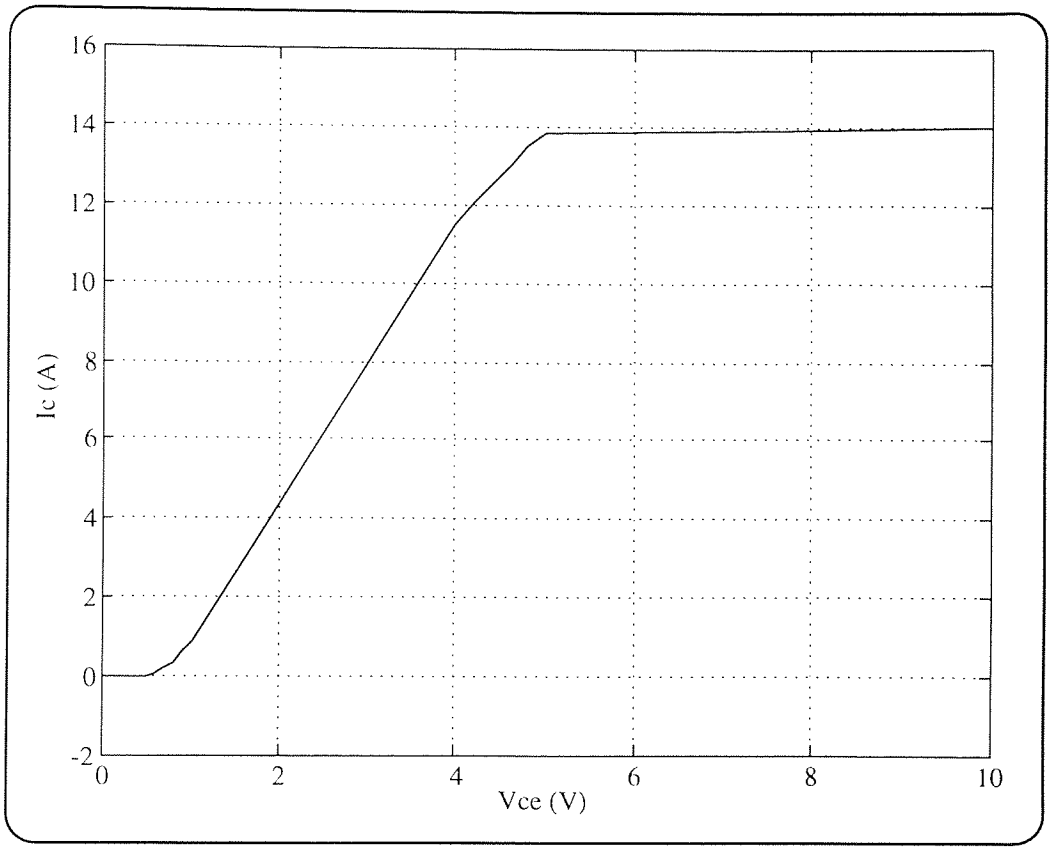

Figure 3.5: IGBT Model Results (V_{ge} = 10V)

Similar problems occurred with the diode model as with the IGBT model, the main difference being that it was discovered that by placing a 0.04Ω resistor in series with the diode, the model was forced to have the same characteristics as the data sheet. The default values for the diode can be seen in appendix A4.2. The parameters that were chosen for the diode model were:

1. junction potential - 0.85V
2. reverse breakdown voltage - 1400V
3. current at breakdown voltage - 0.1mA

A comparison of the model results for the diodes when compared to the data sheet results can be seen in the following graphs, Figures 3.6 and 3.7. As can be seen from these results the SABER diode model results correlate well with the data sheet results to within 1.5A.

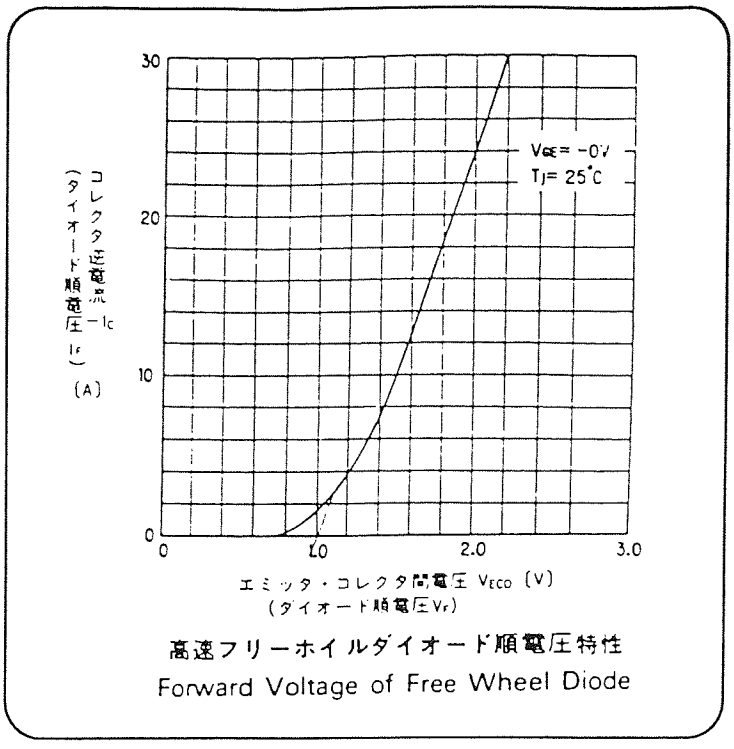

Figure 3.6: Diode Data sheet Values

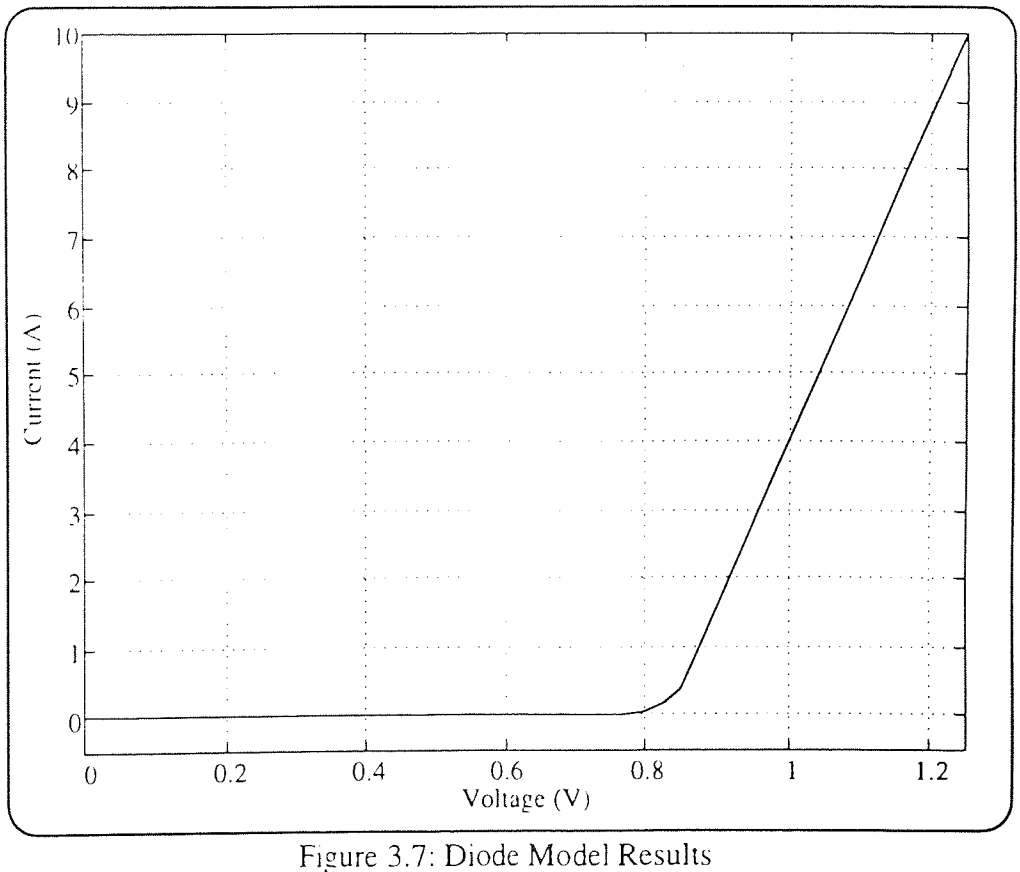

Figure 3.7: Diode Model Results

The final difficulty with the drive model occurred with the switching times of the IGBT's. As the 583 drive is a PWM (Pulse Width Modulation) device the IGBT's could not just be switched on and off at a constant frequency, because this would cause changes with the voltage and current sources around the model and prevent the modelled results from comparing with the measured results. To overcome this problem the switching times were measured and then these times were put into a template within SABER Figure 3.8 below shows the switching times for each IGBT. The program for the PWM switching times can be seen in appendix A5.4.

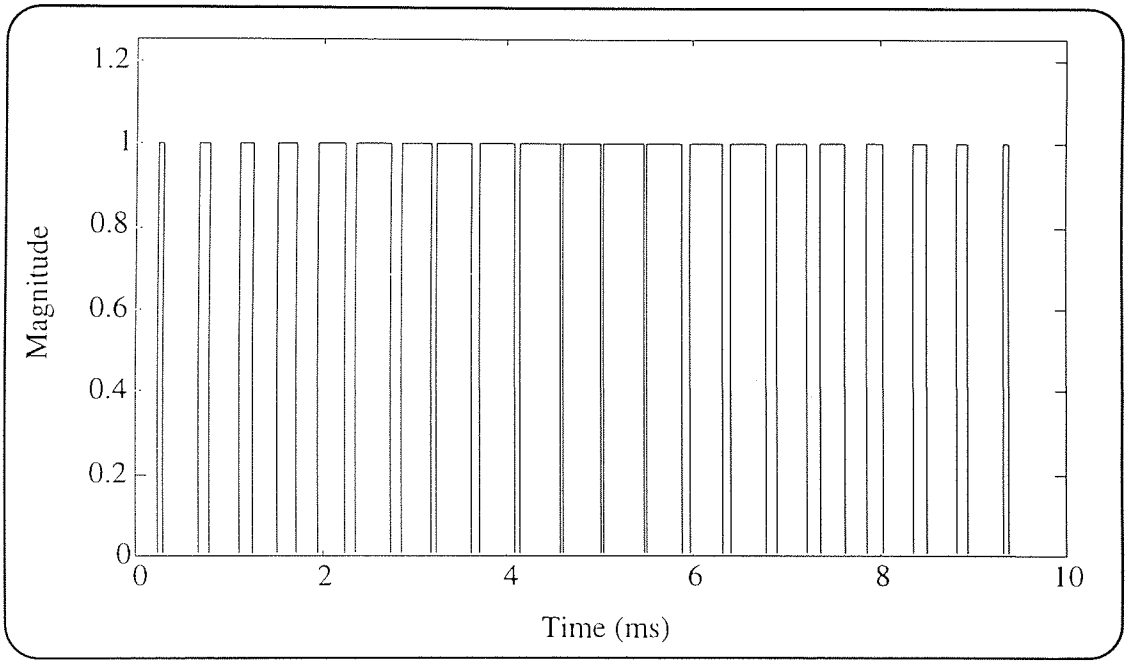

Figure 3.8: PWM Switching Times

3.3 Shielded Cables

The cable that was used to connect the motor to the drive was a five meter length of single braid armoured cable. Due to its length and structure this cable is in fact a very good source of electromagnetic emissions, which is due to the stray capacitive coupling to ground and between the cables as well as any mutual inductance that is present within the cable, Conway (1994). Bergervoet (1994) also showed that any electromagnetic radiation from a device does not usually come from the pcb (printed circuit board) but from the cables that are attached to the board. The reason that

Bergervoet gives for this is that any high frequency signals that are present on the pcb will generally give rise to a common-mode current (I_{cm}) in the attached cables, and this current is a more efficient source of radiation than the currents on the pcb. It was therefore important to correctly characterise the cable that connects the drive to the motor.

The cable model that was used can be seen in Figure 3.9A, only two phases are shown whereas in reality there are three phases. The structure of the shielded and the notation used can be seen in Figure 3.9B.

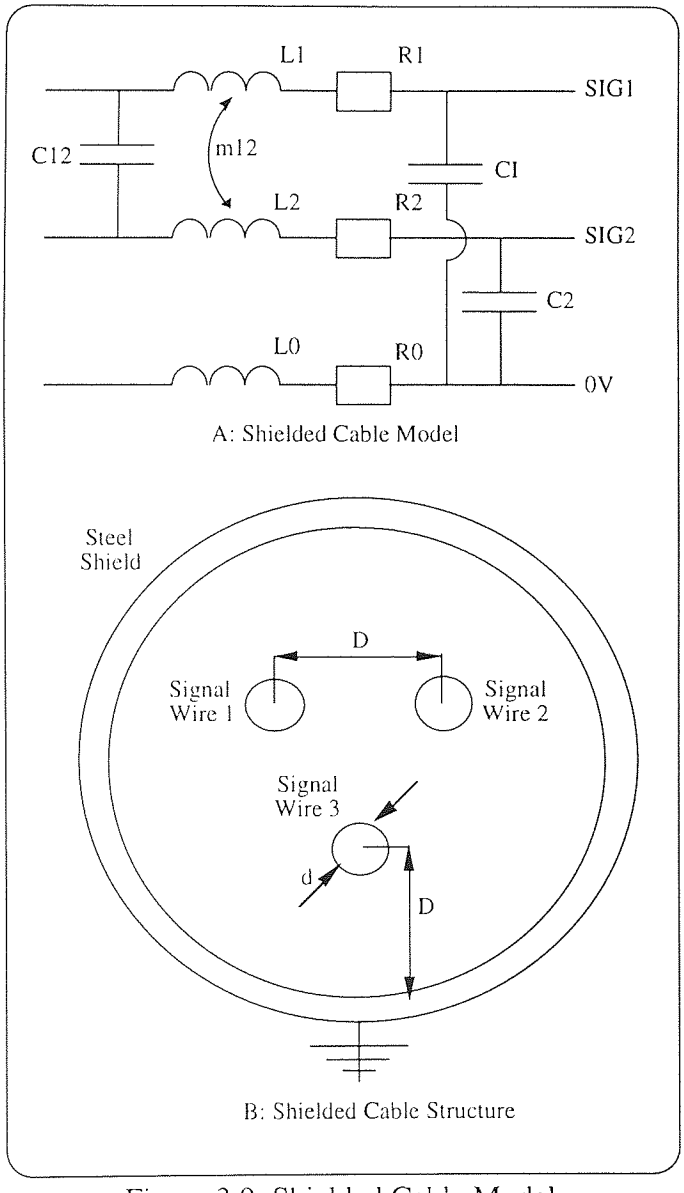

Figure 3.9: Shielded Cable Model

The inductances of the lines were calculated using the following equation from Goedbloed (1990):

$$L = \frac{\mu l}{\pi}\left[\ln\left(\frac{2l}{D}\right) - \frac{D}{l}\right] \qquad \text{(eq3.3.1)}$$

The next parameter to be calculated was the mutual inductance as specified by Williams (1994):

$$m = 0.002\, l\left[\ln\left(\frac{2l}{D}\right) - 1 + \frac{D}{l}\right] \qquad \text{(eq3.3.2)}$$

$$k = \frac{m}{\sqrt{(L_1 L_2)}} \qquad \text{(eq3.3.3)}$$

The capacitance between the cables was defined by Goedbloed (1990) as:

$$C = \frac{\pi \varepsilon l}{\ln(D/r)} \qquad \text{(eq3.3.4)}$$

The capacitance between the cables and the shield, which was electrically connected to the ground plane, was approximated using the equation defined by Stevenson (1962):

$$C_n = \frac{2\pi \varepsilon l}{\ln(D/r)} \qquad \text{(eq3.3.5}$$

The resistance of the cables was calculated using the equation defined by Stevenson (1962):

$$R_{ac} = \frac{\rho l}{A} S \qquad \text{(eq3.3.6)}$$

Where s is:

$$S = \sqrt{\frac{2 f \mu}{\rho / \pi r^2}} \qquad \text{(eq3.3.7)}$$

$$\varepsilon = \varepsilon_0 \varepsilon_r \qquad \text{(eq3.3.8)}$$

$$\mu = \mu_0 \mu_r \qquad \text{(eq3.3.9)}$$

where:

A - cross sectional area = $3.14 \times 10^{-6} m^2$

D - distance between the wires = 4.5mm

f - frequency = 50Hz

k - the coefficient of coupling between the inductances (ratio)

l - length of the wires = 5m

r - radius of the wires = 1mm

ε_0 - permittivity of free space = $8.854 \times 10^{-12} F/m$

ε_r - relative permittivity of copper = 1

μ_0 - permeability of free space = $4 \pi \times 10^{-7} H/m$

μ_r - relative permeability of copper = 1

ρ - resistivity of copper = $2 \times 10^{-8} \Omega m$

The above parameters were calculated using the equations and then where possible the parameters were also measured. The calculated and experimental values can be seen in Table 3.1 below, along with the differences between the values. As can be seen form the differences there was a good correlation between the calculated and the experimental values.

Parameter	Calculated	Experimental	% Difference
R @ 50HZ	0.0267Ω	0.026Ω	2.7
C	462pF	430.5pF	7.3
C_n	924.68pF	1000pF	7.5
L	3.0μH	2.7μH	11.1
m	6.71mH	Not Measurable	/

Table 3.1: Comparison of Experimental and Calculated Cable Parameters

3.4 Line Impedance Stabilising Network

As was mentioned in chapter 2, a LISN (Line Impedance Stabilising Network) is an important part of any conducted emissions testing set up, its function being to provide a defined impedance (50Ω) across the measuring point as well as isolating the EUT (Equipment Under Test) from unwanted interference signals on the supply mains. As the circuit model was going to be used to determine the conducted emissions of the drive it was necessary to include a model for the LISN used in the tests in the circuit model. Figure 3.10 shows the manufacturers circuit diagram for the LISN that was used, and this was put into a template within the SABER circuit simulator.

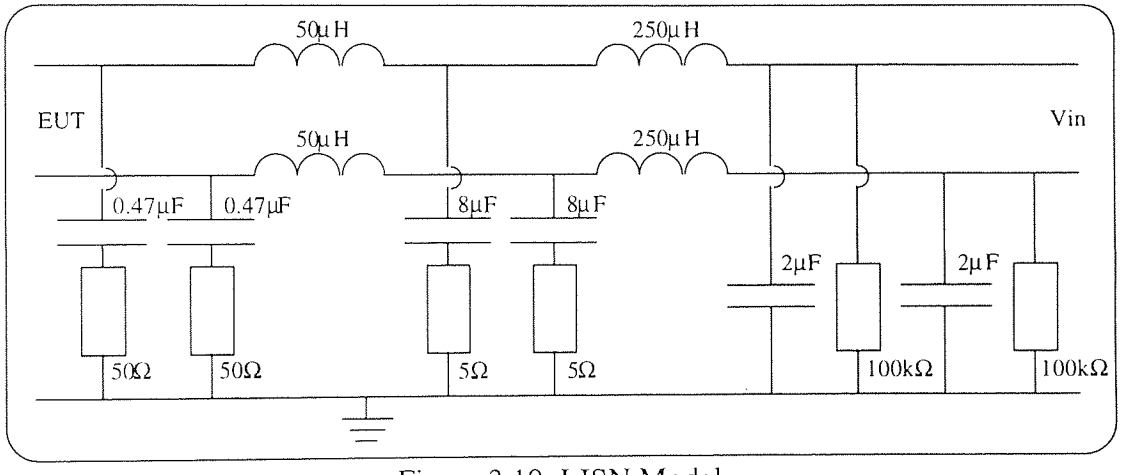

Figure 3.10: LISN Model

3.5 Motor Model

The testing of the drive, for the conducted emissions and for the current and voltage sources, had to be performed whilst a motor was connected and running. Therefore the motor would have to be included in the overall circuit model. As the motor used was an induction motor, it was necessary to generate a circuit model for it. The model that was generated consisted of inductors, resistors and capacitors, all of which were arranged in a delta pattern. The reason for this being that during all the testing the motor windings were connected up in a delta formation. The circuit diagram for the model can be seen in Figure 3.11 below. The motor model assumed that the motor had near zero load, this was justified as all the experimental work was done with the motor running freely.

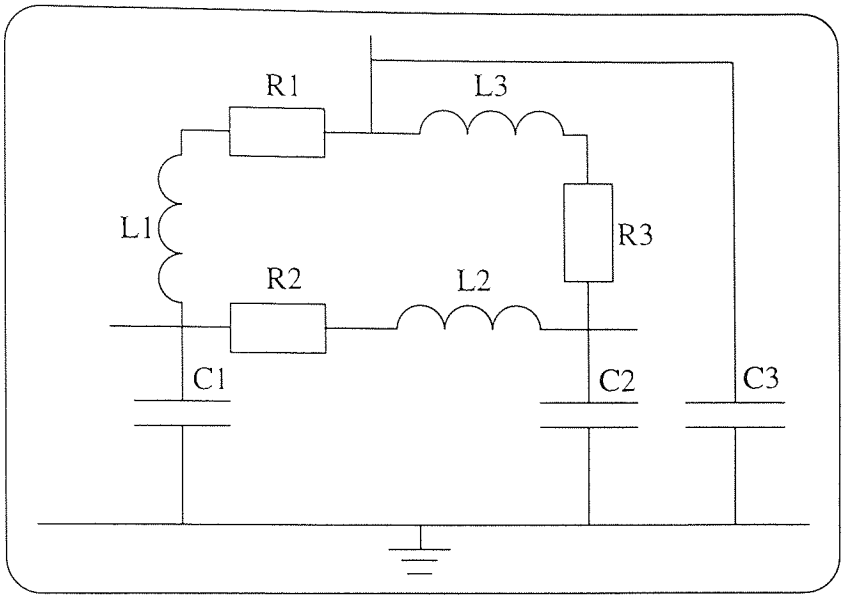

Figure 3.11: Induction Motor Model

The inductors in the model represent the inductance of the windings and the resistors represent the resistance of the windings. The three capacitances do not actually exist in a physical sense, but they are an important part of the motor model. They represent the parasitic capacitance between the windings and the motor casing. The casing is connected to ground via the shielded cable that attaches the motor to the drive. The values that were assigned to the capacitances, inductances and resistances could not be calculated, so measurements were made on the motor that was used for all the tests, see appendix A1.2 for details of the motor. The values of the components being:

1. Inductance = 22mH
2. Resistance = 30Ω
3. Capacitance = 1.6nF

3.6 Circuit Parasitics

A number of parasitic capacitances are present within the 583 drive:

1. between the centre of bridge rectifier and ground
2. between the centres of the pairs of IGBT's and ground
3. between the centres of the pairs of IGBT's and the positive and negative DC link

It is important to include these capacitances in the circuit model as they provide an important path for the common mode currents which are coupled through them to the ground plane, Lin and Chen (1994). Figure 3.12 below shows how the parasitic capacitances are positioned in the drive.

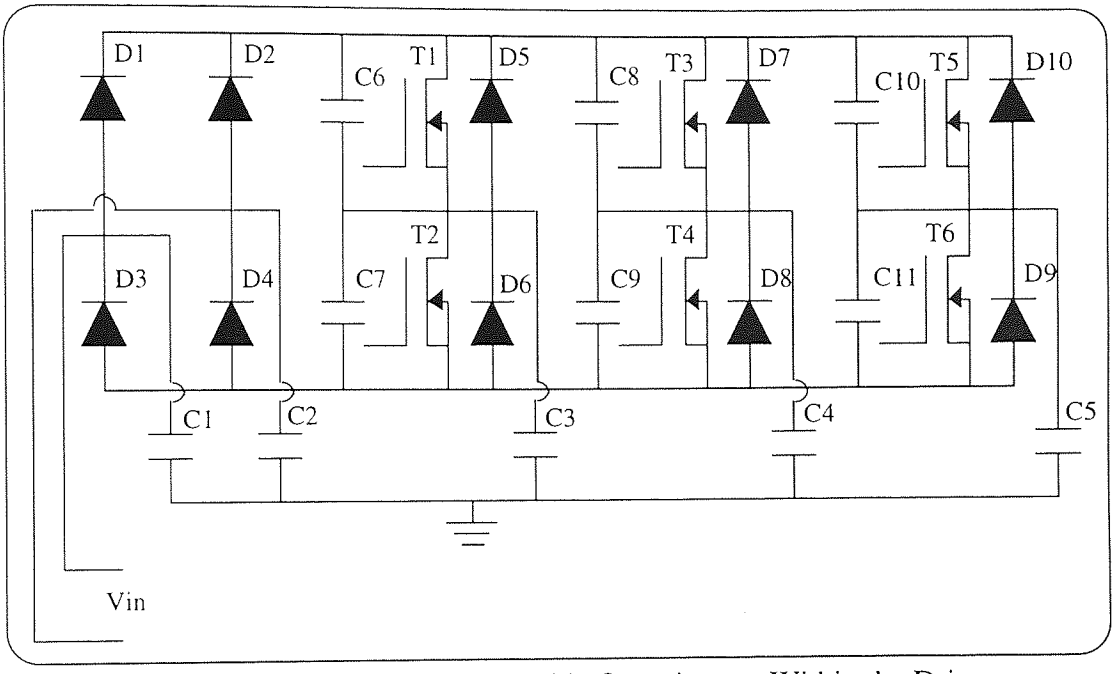

Figure 3.12: Position of the Parasitic Capacitances Within the Drive

In the above figure capacitors C1 and C2 correspond to the capacitances between the bridge rectifier and ground and they have a value of 120pF, capacitors C3, C4 and C5 correspond to the capacitances between the IGBT pairs and ground and they have values of 165pF. The capacitors C6, C7, C8, C9, C10 and C11 correspond to the internal capacitances of the IGBT module and they have values of 1.75nF.

All of the parasitic capacitances values were measured as there was no obvious way in which to calculate them.

3.7 The Complete Circuit Model

The final circuit model consisted of all the elements that have been discussed previously in this chapter. A complete diagram of the circuit model can be seen in Figure 3.13 below, and the net list that was put into the SABER circuit simulator can be seen in

appendix A5.1.

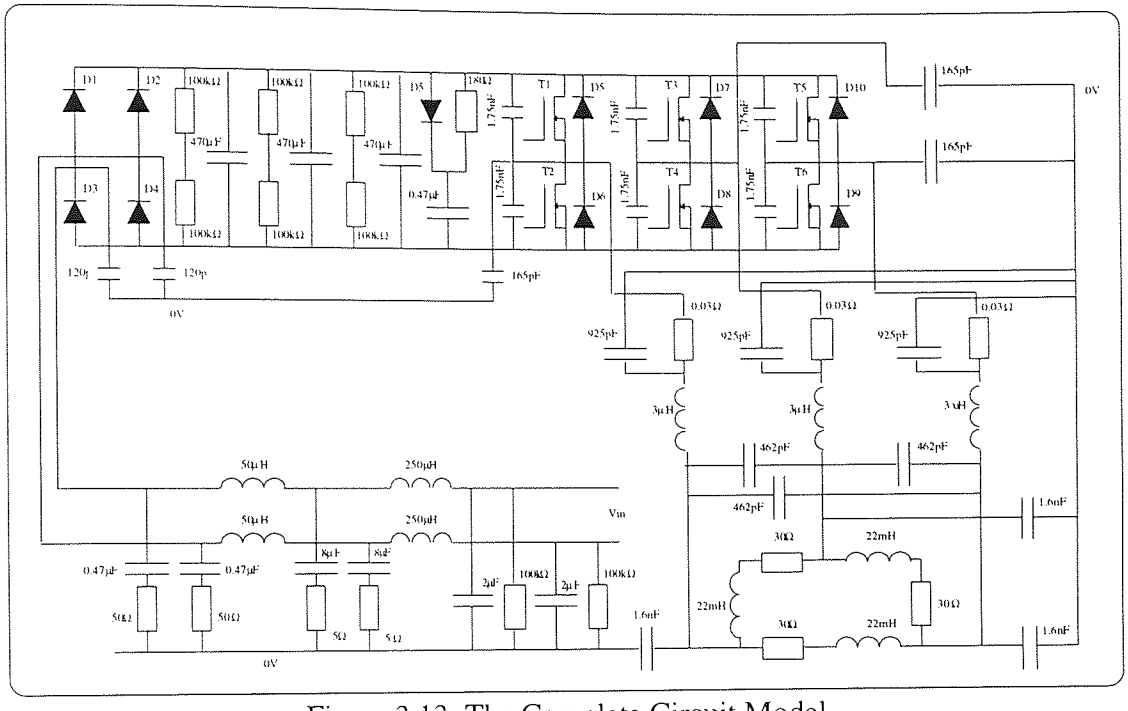

Figure 3.13: The Complete Circuit Model

3.8 Circuit Model Results

The circuit was modelled to generate two separate sets of results, the first set being the current and voltage sources which were used to confirm the validity of the model and to generate a radiated emissions model. The second set of results were the conducted emissions which were measured across the 50Ω impedance in the LISN.

3.8.1 Model Validation

The model was validated by measuring the dv/dt's and di/dt's at two important points in the circuit, and then comparing these values to the model values. The points that were chosen were on the DC link, between the smoothing capacitors and the IGBT module (nodes 3 and 101 on the net list in appendix A5.1), and on the transmission line to the motor (nodes 19, 22 and 25 on the net list in appendix A5.1). These points were chosen as it was felt they would give representative measurements.

The model results for the current and voltage waveforms can be seen along with

measured values in the following graphs, Figures 3.14 to 3.17. The modelled values need to be multiplied by $\sqrt{2}$ to give peak values.

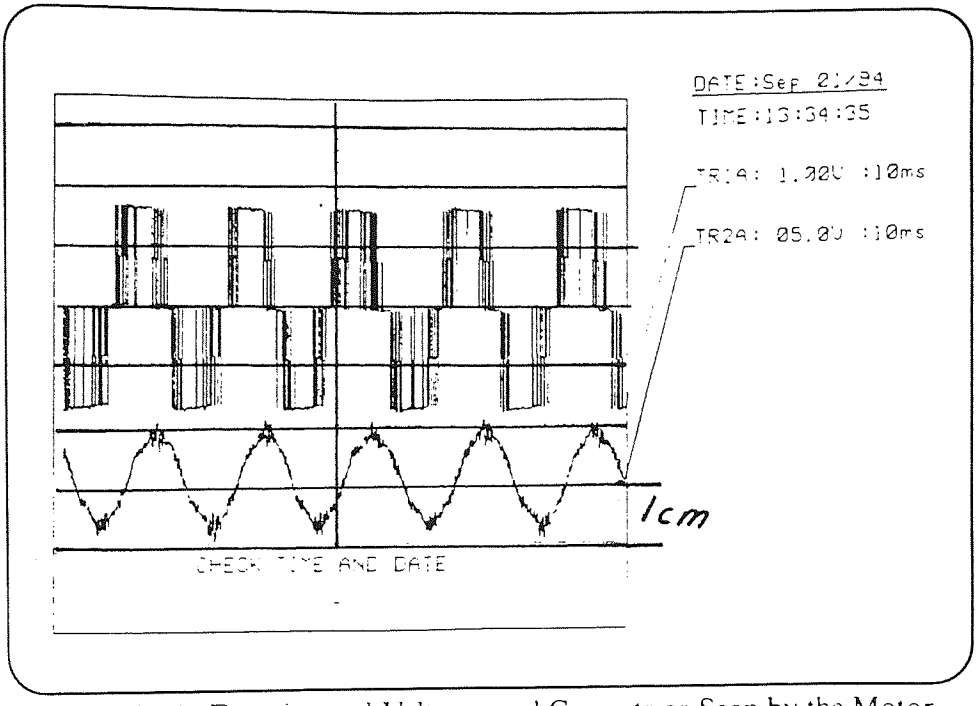

Figure 3.14: Experimental Voltages and Currents as Seen by the Motor

To obtain the values of the voltage in the above plot, the height trace 1A in cm must be multiplied by 200, which will give the peak value:

$$\text{Voltage (V)} = \text{TR1A} \times 200 \qquad \text{(eq3.8.1)}$$

With the current, the height trace 2A in cm must be multiplied by 2 to give values in amperes, and again this will give peak which are:

$$\text{Current (A)} = \text{TR2A} \times 2 \qquad \text{(eq3.8.2)}$$

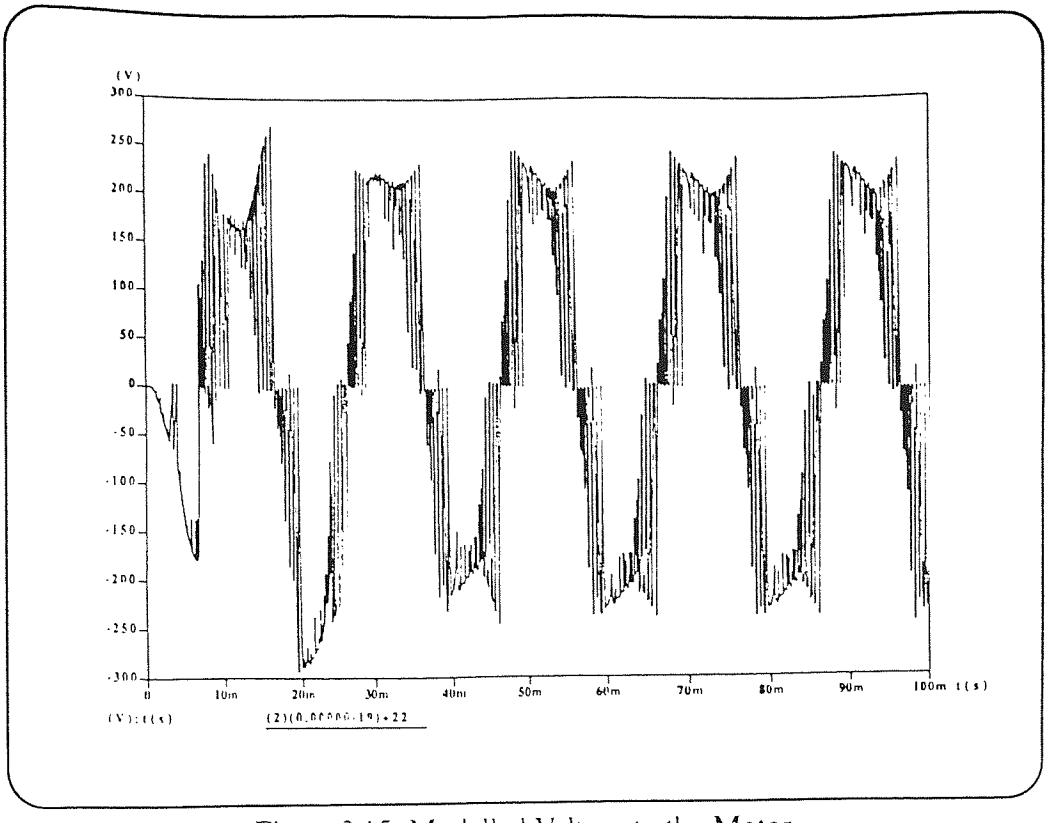

Figure 3.15: Modelled Voltage to the Motor

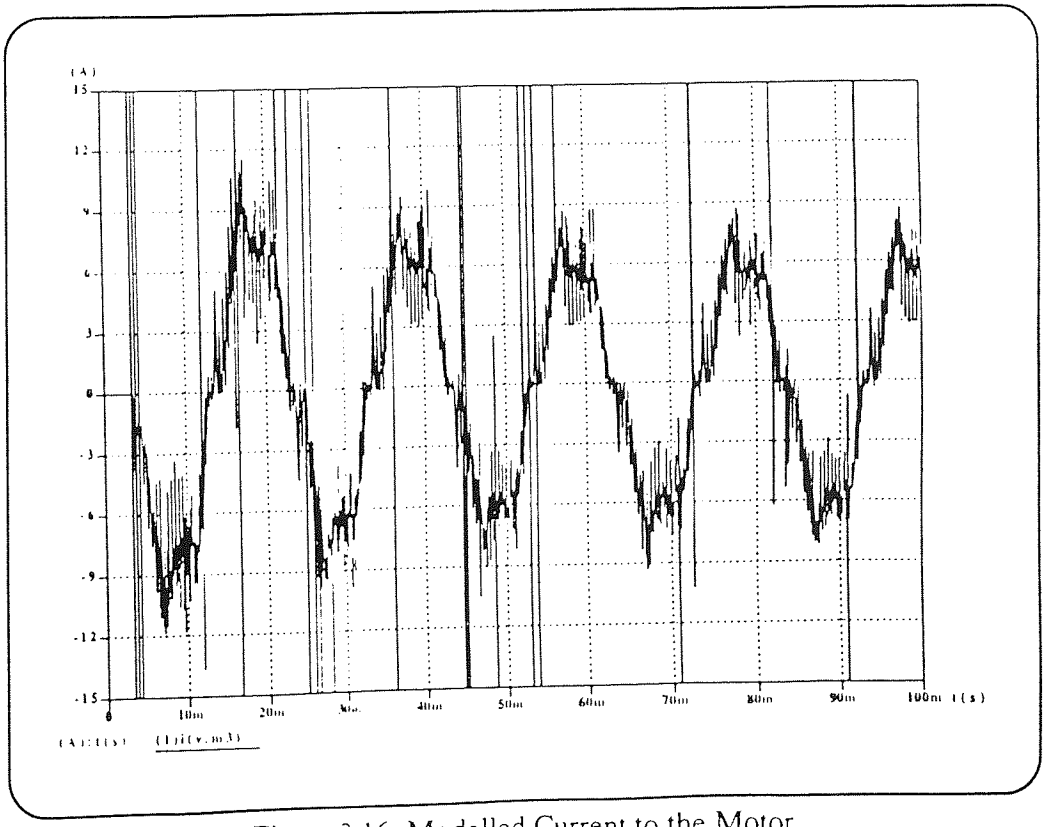

Figure 3.16: Modelled Current to the Motor

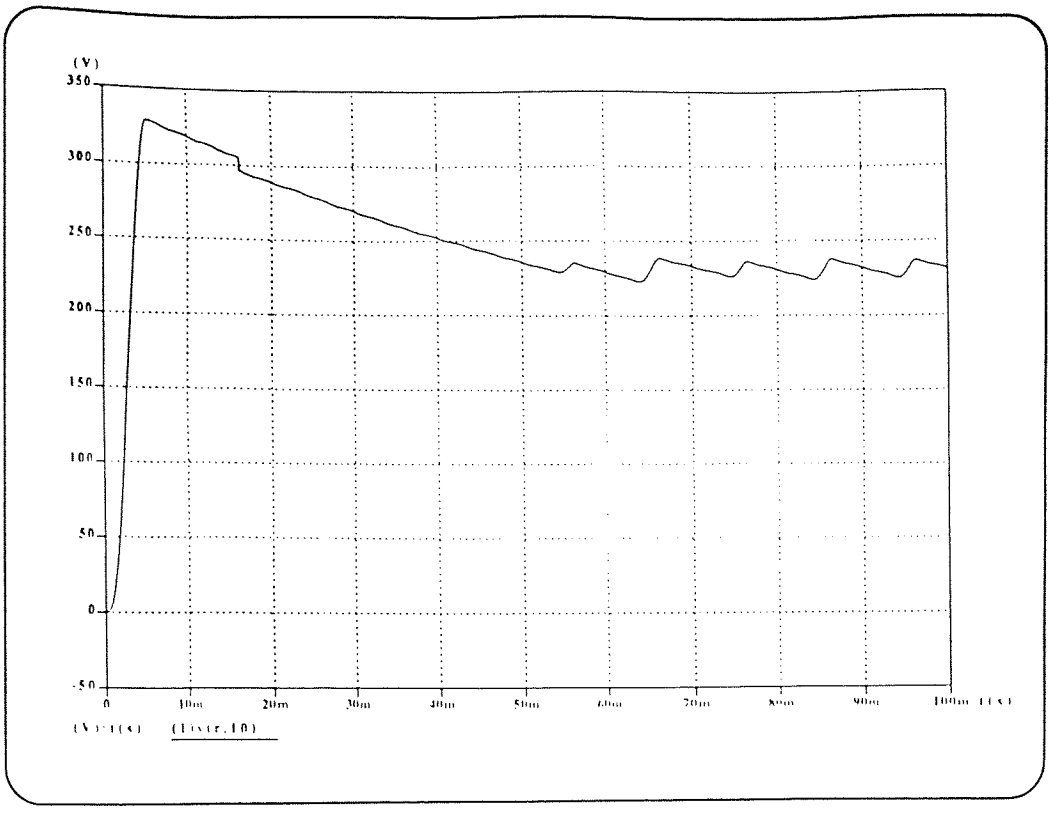

Figure 3.17: Modelled Voltage on the DC Link

As can be seen from the graphs the SABER simulation takes approximately 50ms to settle into steady state conditions. After the 50ms has elapsed both the currents and the voltages to the motor have magnitudes that are within 10% of the measured values. The frequencies of these two waveforms are also the same as the measured results, which is what was expected as the frequency of the waveform is dependent on the switching of the IGBT's which in the model were switched in the same manner as the actual device. The small spikes that are occurring on the current waveform are believed to be due to the switching of the IGBT's, and a similar effect does occur on the measured results. With the voltage waveform there is a certain amount of overshoot at each end of the PWM waveforms, even though this does not strictly occur it was ignored because the synthesised sine wave was still evident in the waveform. Similarly the large spikes (in excess of 15A) which can be seen on the current waveform do not exist in practice, and were probably due to some mathematical error in the circuit model.

The DC link voltage was accurate to within 3% of the measured values after the initial 50ms had elapsed. The slight ripple that was evident on the DC link voltage is due to the smoothing capacitors charging and discharging throughout the cycle, and this ripple

was witnessed when the DC link voltage was measured.

3.8.2 Conducted Emissions

As was said previously the second purpose of the circuit model was to predict the conducted emissions from the drive on the power cable. The experimental setup that was used for the measurements can be seen in Figure 3.18 below.

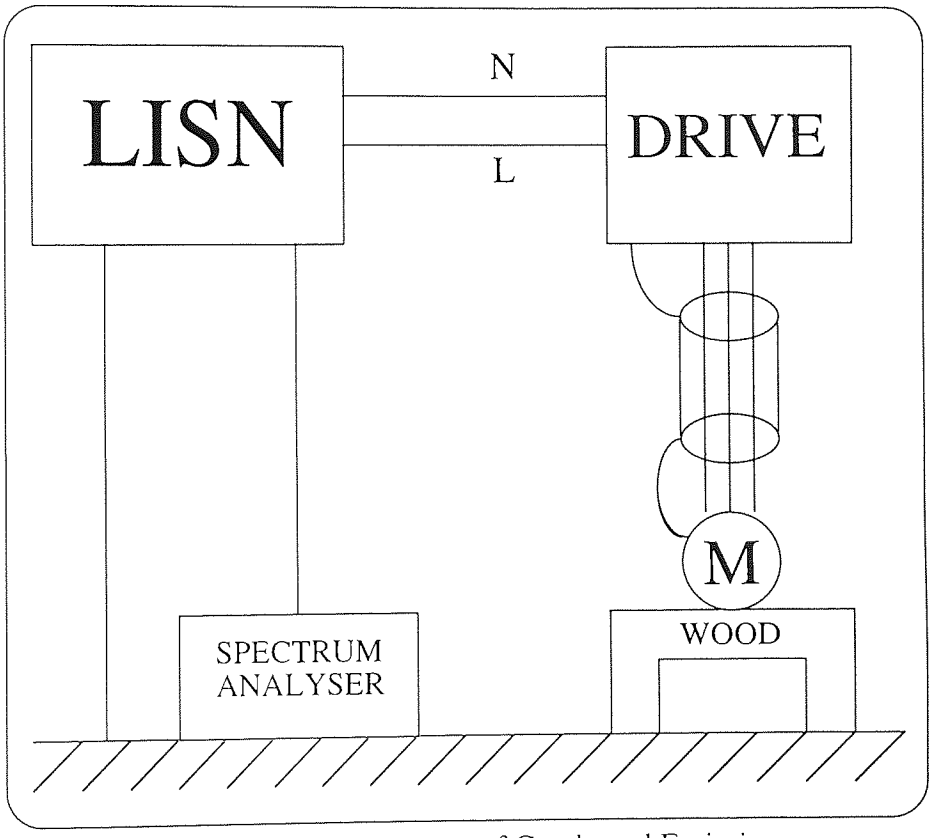

Figure 3.18: Measurement of Conducted Emissions

The spectrum analyser (Advantest R3261) which was connected across the 50Ω impedance in the LISN generated results in the 150kHz to 30MHz range which is the range that the EMC legislation for drives specifies. The results from this test can be seen in Figure 3.19, where the y-axis has units of dBμV and the x-axis is in a logarithmic scale in Hz.

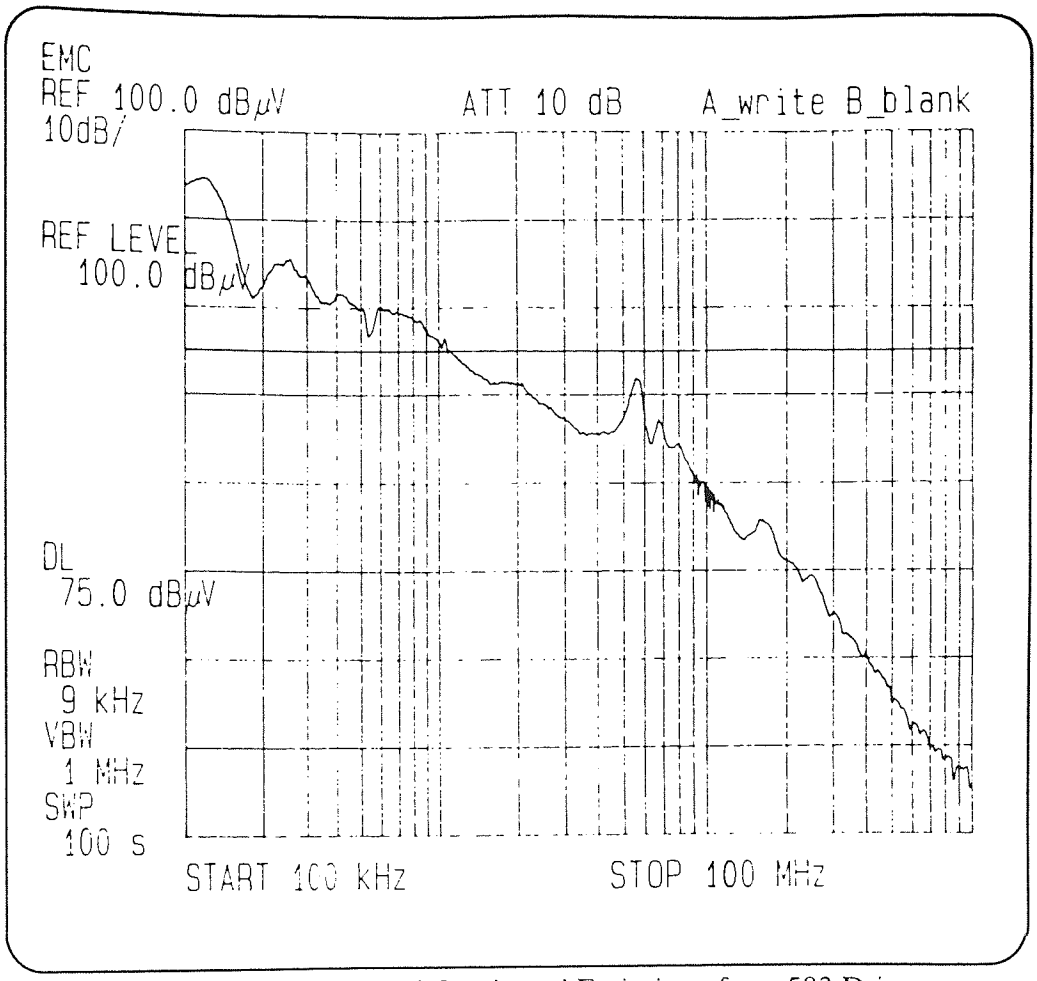

Figure 3.19: Experimental Conducted Emissions from 583 Drive.

When the conducted emissions were simulated in SABER they were initially in the time-domain and to convert them to the frequency-domain as is required by the EMC legislations, a Fourier transform was performed within the SABER simulator. The Fourier transform function within SABER is based on the fact that any periodic, piece-wise continuous, complex-valued function f(t), can be expressed as an infinite series (Fourier series) as shown in equation 3.8.1 below.

$$f(t) = a_0 + \sum_{n=1}^{\infty} a_n \cos(n\omega t) + \sum_{n=1}^{\infty} b_n \sin(n\omega t) \qquad \text{(eq3.8.3)}$$

where:

$$a_0 = \frac{1}{T}\int_{t}^{t+T} f(t)\,dt \qquad \text{(eq3.8.4)}$$

$$a_n = \frac{2}{T}\int_{t}^{t+T} f(t)\cos(n\,\omega\,t)\,dt \qquad \text{(eq3.8.5)}$$

$$b_n = \frac{2}{T}\int_{t}^{t+T} f(t)\sin(n\,\omega\,t)\,dt \qquad \text{(eq3.8.6)}$$

Where a_n and b_n are the spectral components of f(t), a_0 is the DC component of the waveform, ω is fundamental frequency in rad/s, and n=1 is the fundamental harmonic. The frequency of the fundamental harmonic is given by equation 3.8.7, where T is the time base of the periodic waveform, this frequency is known as the fundamental frequency.

$$f_0 = \frac{1}{T} \qquad \text{(eq3.8.7)}$$

In general it will only take the first few harmonics (eg 10) to represent the waveform in the frequency-domain to 95% accuracy. However the time period of the waveform modelled across the 50Ω resistor was 20ms. Giving a fundamental frequency of 50Hz. So to obtain the Fourier transform for the correct frequency range (150kHz to 30MHz) it was necessary to calculate about 750,000 harmonics.

The results obtained from this simulation can be seen in Figure 3.20, along with the measured results.

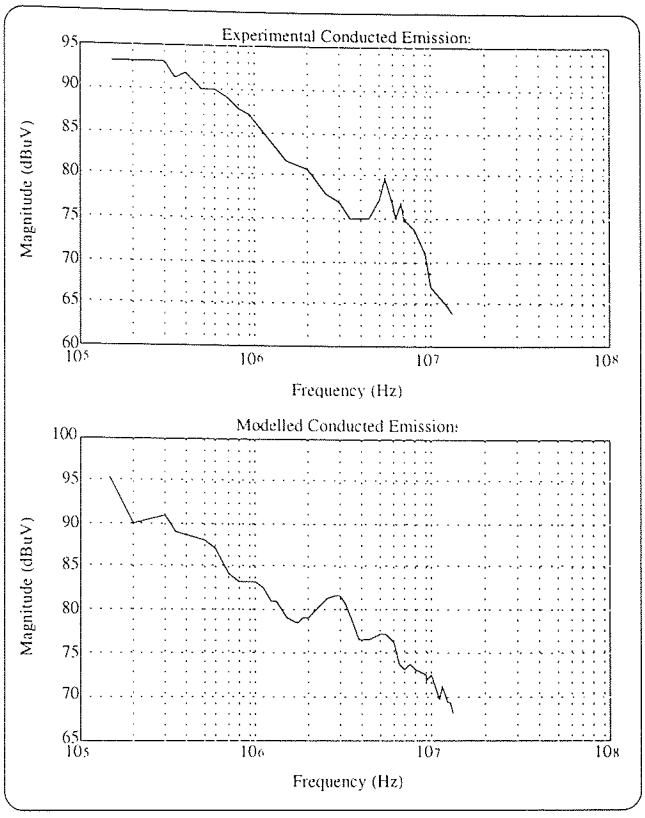

Figure 3.20: Comparison of Measured and Calculated Conducted Emissions

As can be seen from the above graphs the modelled emissions follow the experimental emissions very closely. The decay of both of the plots is -20dB/decade, and this decay starts to occur at 3.33MHz which is the frequency of the rise time of the IGBT's (t_r=300ns). The prominent peaks occurring at 3MHz on the modelled data and at 5MHz on the experimental data appear to be due to resonances of the inductances and the capacitances of the shielded cable. Where the resonant frequency is defined by:

$$f_r = \frac{1}{2\pi\sqrt{LC}} \qquad \text{(eq5.8.6)}$$

Table 3.2 shows the calculated values for the resonant frequency using both the experimental and the calculated values for the inductances and the capacitances of the shielded cable. As can be seen from Table 3.2 it is not obvious which combination of inductance and capacitance is causing the resonance. As both the combinations are so close to the values in the experimental and modelled data it was suspected that the resonance was actually due to a combination of the two values calculated.

Parameters Used	f_r from calculated values of L and C	f_r from measured values of L and C
L and C	4.3 MHz	4.7 MHz
L and C_n	3.0 MHz	3.1 MHz

Table 3.2: Comparison of the Resonant Frequencies of the Shielded Cable

Where:

L - Inductances of the lines (H)

C - Capacitance between the lines (F)

C_n - Capacitance between the lines and the shield (F)

The errors between the experimental and the modelled data can be seen in Figure 3.21. It can be seen that the errors ranged between -6dB and 6dB.

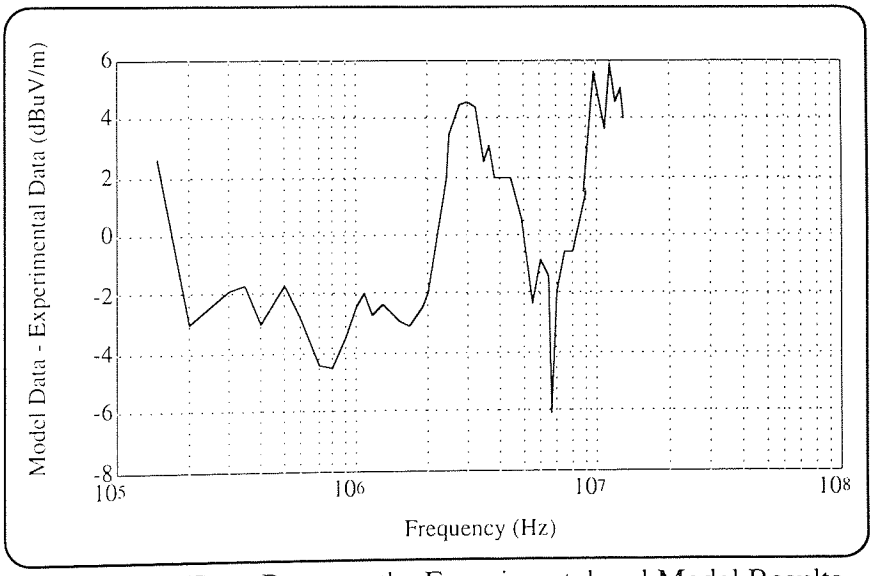

Figure 3.21: Error Between the Experimental and Model Results

3.9 Simplified Drive Model

As the IGBT's in the drive were only being used as switches, a second simulation was run where the IGBT's were replaced by single-pole single-throw switches with a diode in series to prevent the current flow from being bidirectional. The switches were

switched in exactly the same manner as the IGBT's, ie with a 1.8kHz PWM waveform. The configuration of the switches can seen in Figure 3.22 below.

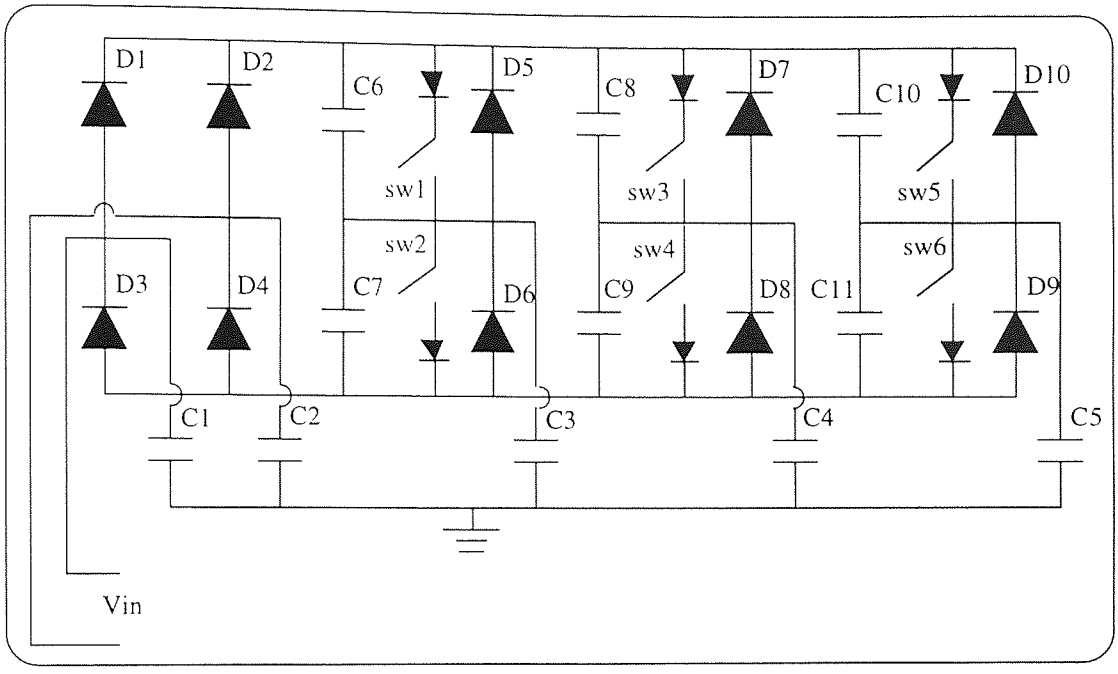

Figure 3.22: Configuration of the Switches in the Simplified Drive Model

The results obtained with these new switches were identical to the ones obtained with the IGBT's, but the model ran 30% faster with the switches. So ultimately this shows that in all the previous simulations the SABER simulator was using the IGBT model as complex switch.

3.10 Summary

This chapter presented a circuit model of the 583 drive set up in the SABER simulator. The model took account of all the elements on the power electronics side of the drive, the shielded cable that connects the drive to the motor, the line impedance stabilising network, the electric motor used in all the tests and also a number of parasitic capacitances that existed within the motor. Specific attention was paid to the modelling of the IGBT's and diodes within the drive, and accurate models of both of these components were produced using the SABER simulator. The model produced voltage and current sources at a number of points around the drive which were used for the prediction of the radiated emissions from the drive. The model was also used to predict

the conducted emissions, which are measured across a 50Ω impedance between the power cable and ground. When the modelled conducted emissions were compared to the measured values an error of +/- 6dB was found to exist. It was found out that the SABER IGBT model was operating as a complex switch, so a new IGBT model was developed using a single-pole single-throw switch with a diode in series to prevent the current flow from being unidirectional. This new IGBT model produced results for the voltage and current sources that were identical to the results obtained using SABER's complex IGBT model. The advantage of the new model was that the simulations ran 30% faster.

Chapter 4

Measurement of Radiated Emissions

4.1 Introduction

As the second part of the work involved generating a method for predicting the radiated emissions from the 583 drive, it was necessary to obtain a set of accurate and repeatable experimental results. This caused a number of problems, the main one being that radiated emissions are highly dependent on the experimental setup. For example the manner in which a cable is coiled can drastically affect a set of results. Lesser problems include the weather, which can influence the way in which the radiation is transmitted through space. The weather can also affect the values of the terrestrial electromagnetic field, which generally has values of 30A/m (magnetic field) and 100V/m (electric field). Finally background radiation emanating from devices such as mobile phones and the spark plugs of internal combustion engines will cause high frequency spikes, and require the experiment to be repeated.

4.2 Experimental Setup and Procedure

The measurements were made using an Open Area Test Site (OATS), so the results obtained corresponded to the current EMC legislations. All the tests were done on a ground plane, which was constructed from wire mesh with a hole size of less than 3cm. The antenna and the drive were placed a distance of 10m apart on the ground plane. The drive, which was not contained in a box, was bolted to a wooden back plate 0.6m above the ground plane, and the antenna was at a height of 1m. The motor was placed next to drive 0.1m above the ground plane. The shielded cable was coiled next to the motor 0.1m above the ground plane. Figure 4.1 below shows the experimental setup.

The measuring device used was a Bi-Log antenna, which is a combined antenna that enables EMC emission testing to be carried out over the required frequency range (30MHz to 1000MHz) without having to use both a Bi-Conical antenna (25MHz to 300MHz) and a Log-Periodic Antenna (150MHz to 1000MHz) to cover the frequency range. The results were recorded using a quasi-peak spectrum analyser (Advantest R3261), with a sweep rate of 1s per 100kHz.

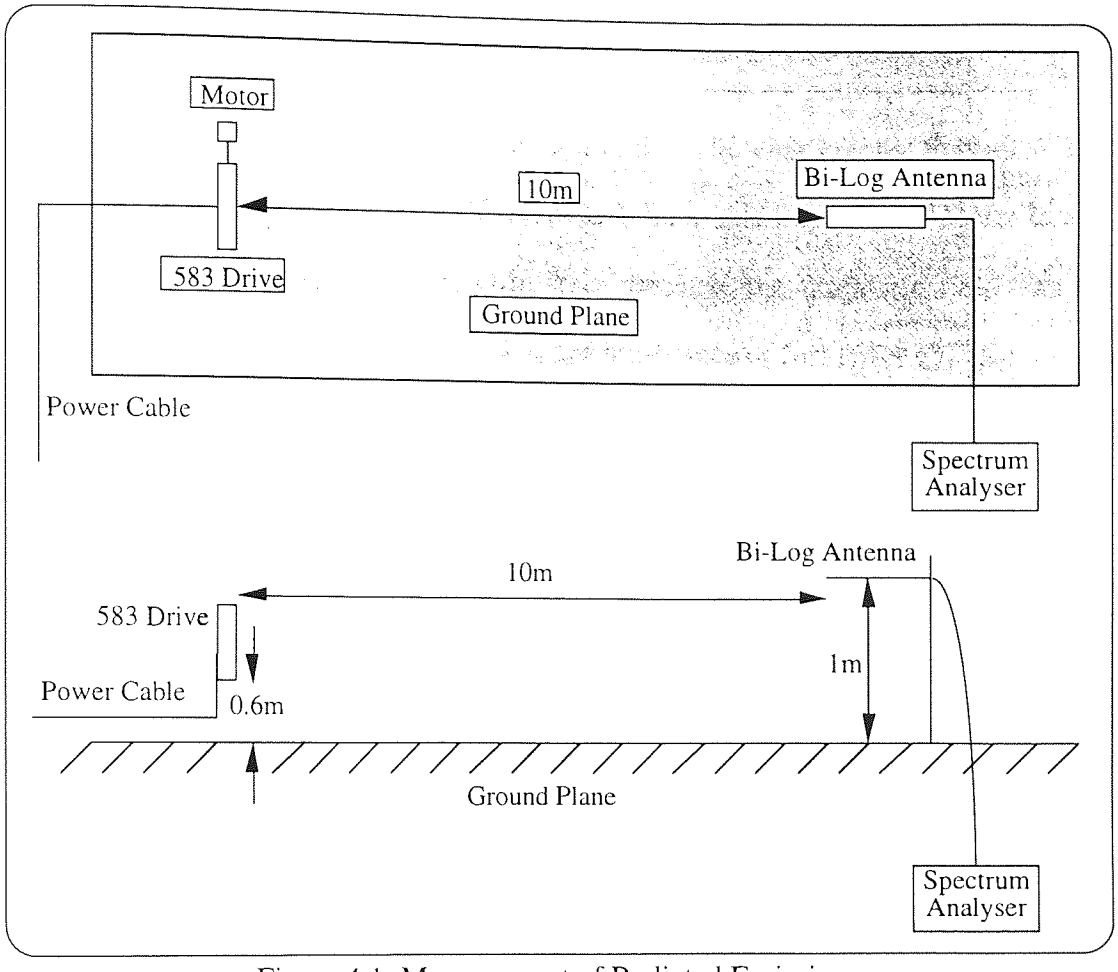

Figure 4.1: Measurement of Radiated Emissions

The experimental procedure covered the frequency range 30-300MHz, with the antenna in both the vertical and horizontal positions.

The reason that the radiation was only measured over the frequency range 30MHz to 300MHz is that above 200MHz the radiation from the drive was insignificant (i.e. below 10dBμV/m = 3μV/m).

The actual radiation emanating from the drive can be determined by subtracting the background radiation from the plot containing both the drive and the background radiation.

4.3 Results

The results from the experiments can be seen in the following graphs, Figures 4.2 to 4.7, where the y-axis has units of dBμV/m and the x-axis has units of MHz. It was only necessary to measure the electric field, because the magnetic field can be determined by dividing the electric field by the impedance of free space (377Ω), as the measurements are made in the far field.

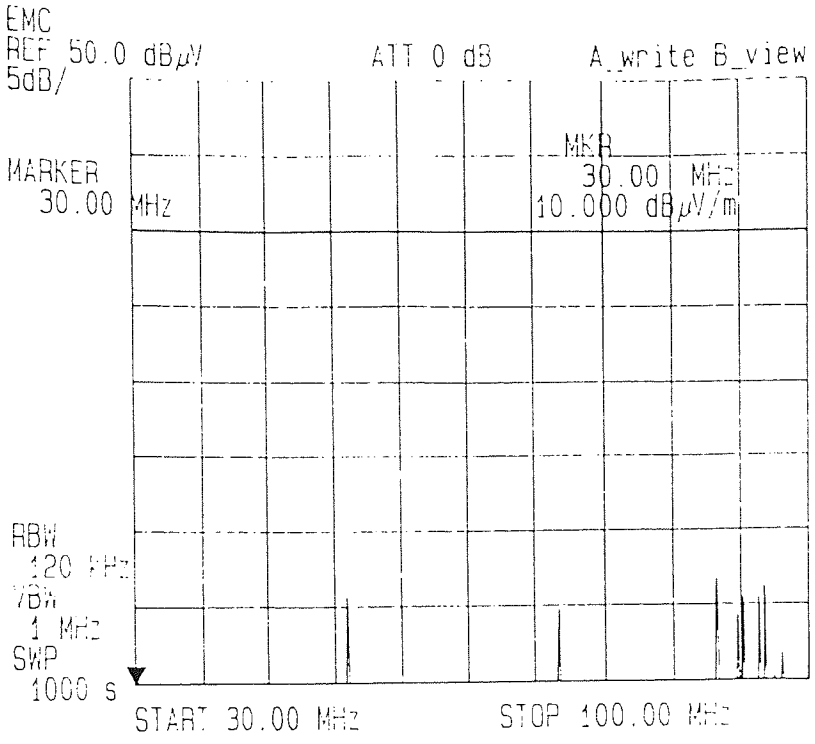

a: Background Radiation

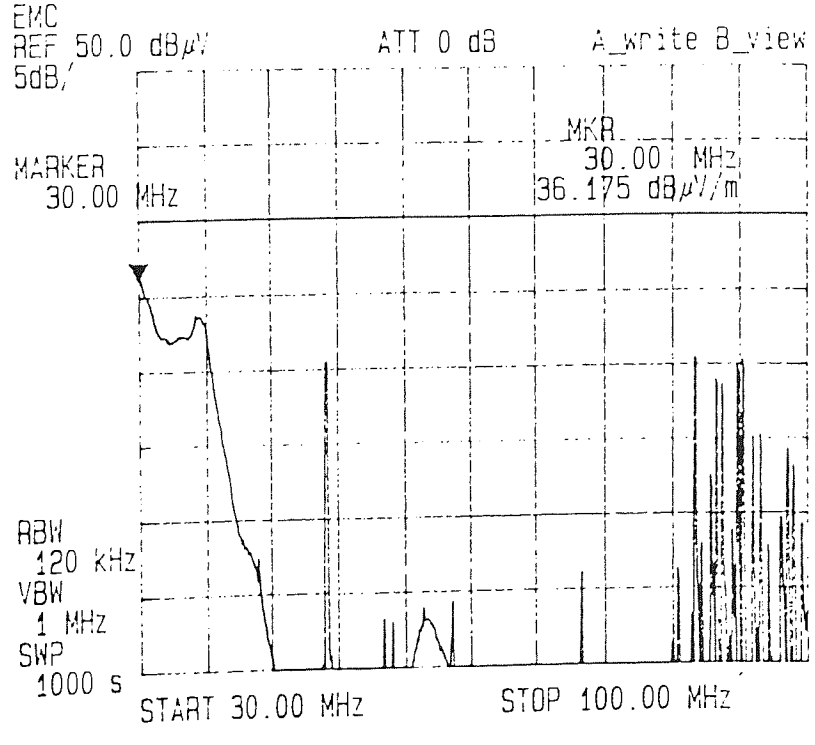

b: Drive Plus Background Radiation

Figure 4.2: Electromagnetic Radiation With the Antenna Horizontal (30 - 100MHz)

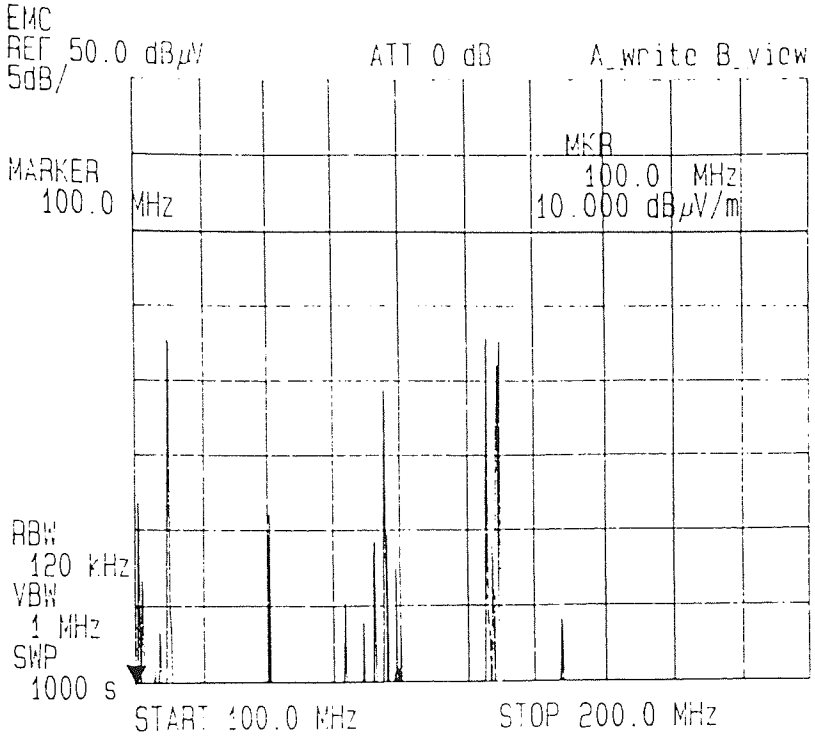

a: Background Radiation

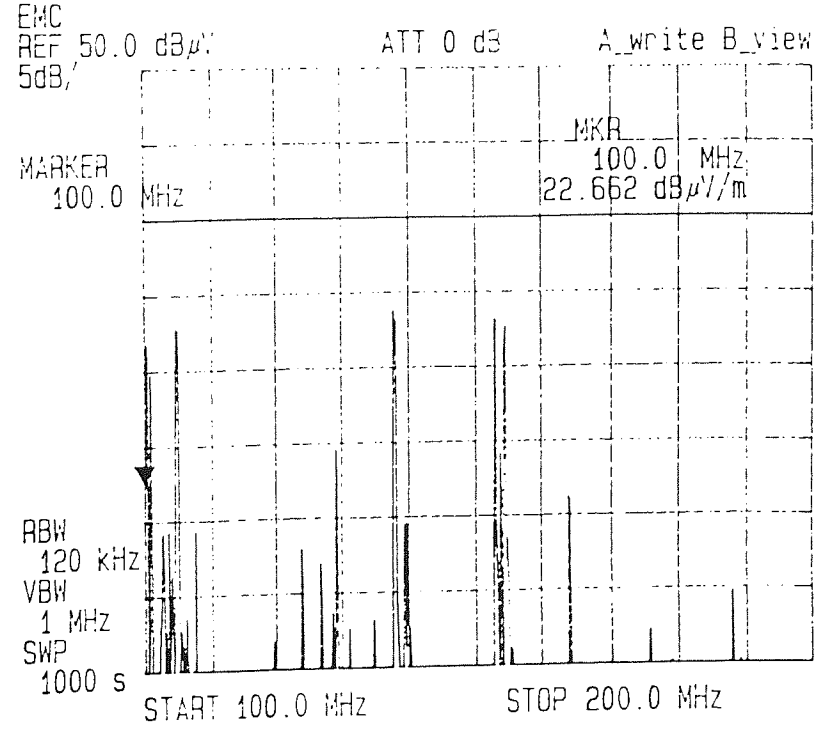

b: Drive Plus Background Radiation

Figure 4.3: Electromagnetic Radiation With the Antenna Horizontal (100 - 200MHz)

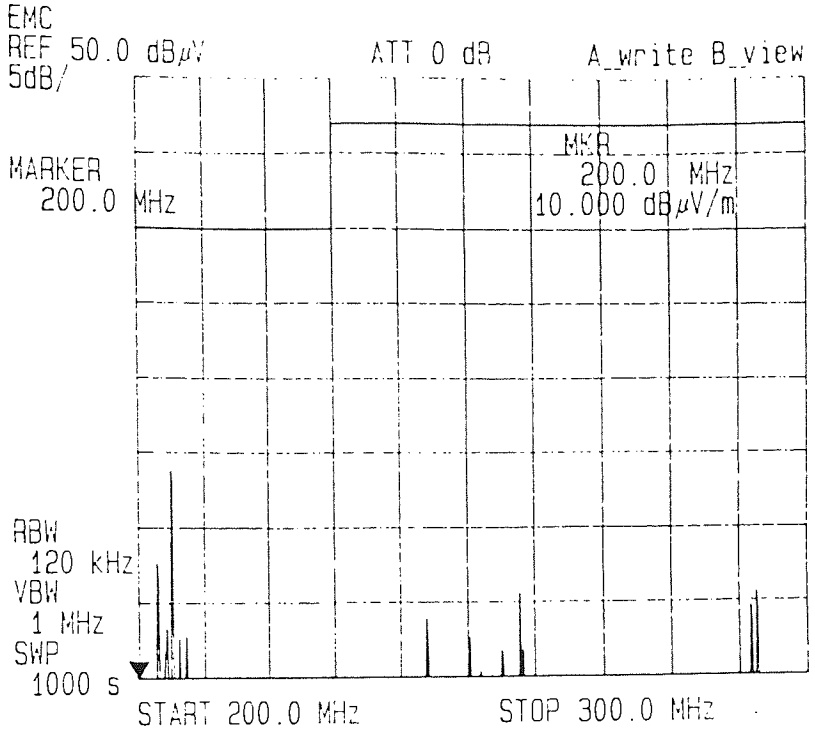

a: Background Radiation

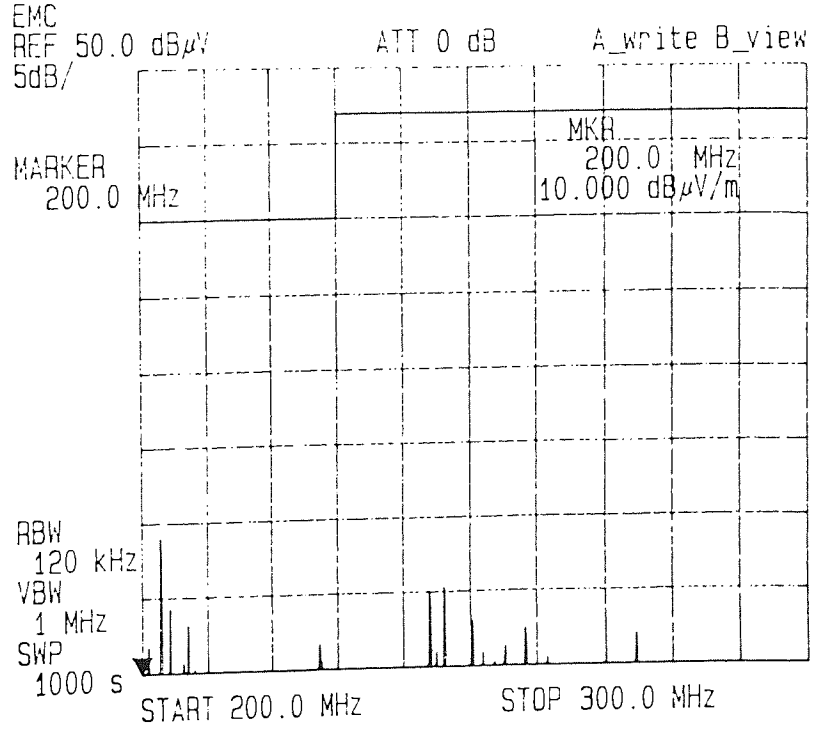

b: Drive Plus Background Radiation

Figure 4.4: Electromagnetic Radiation With the Antenna Horizontal (200 - 300MHz)

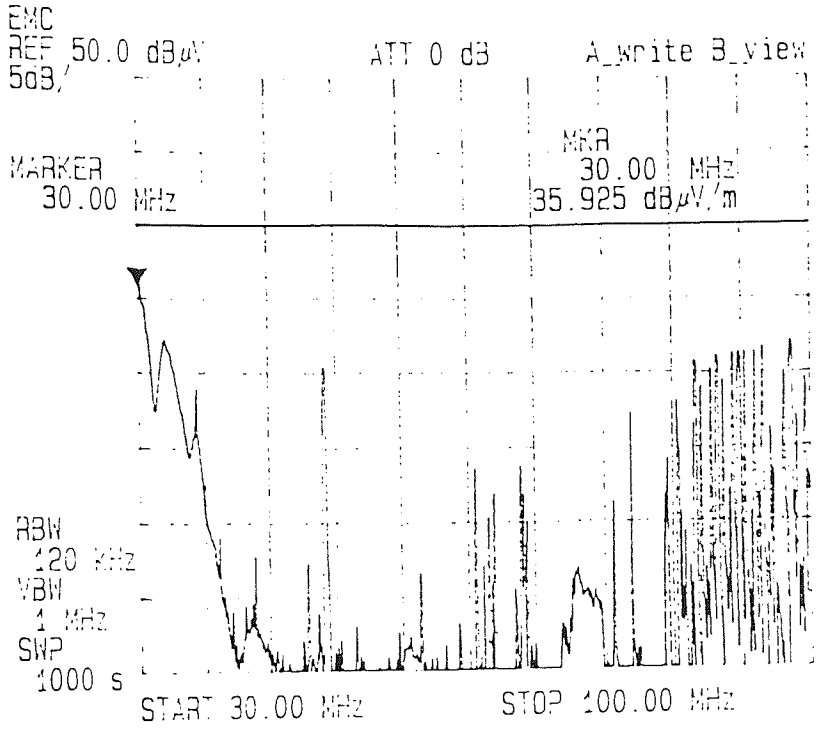

a: Background Radiation

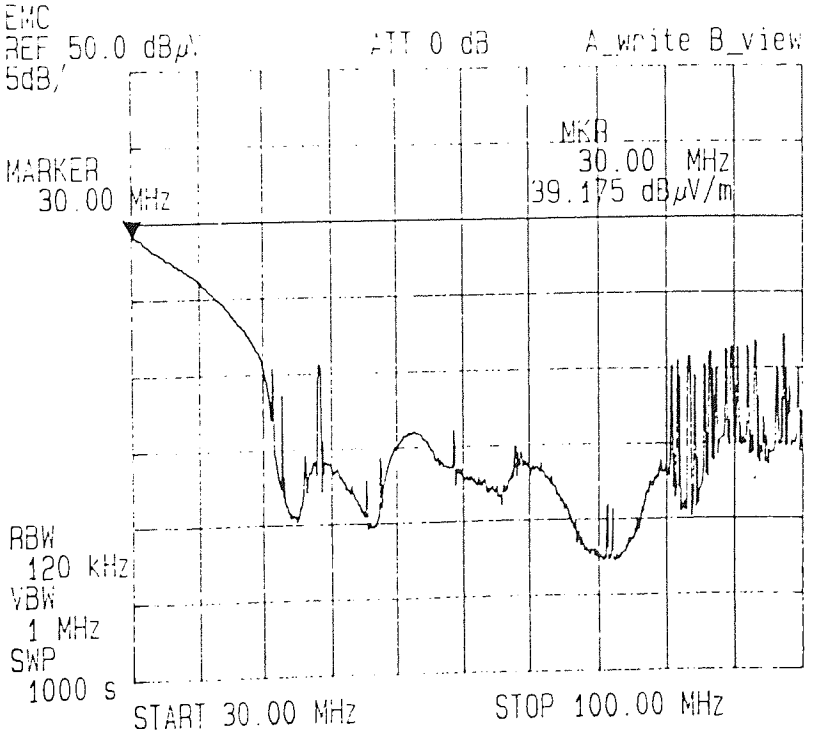

b: Drive Plus Background Radiation

Figure 4.5: Electromagnetic Radiation With the Antenna Vertical (30 - 100MHz)

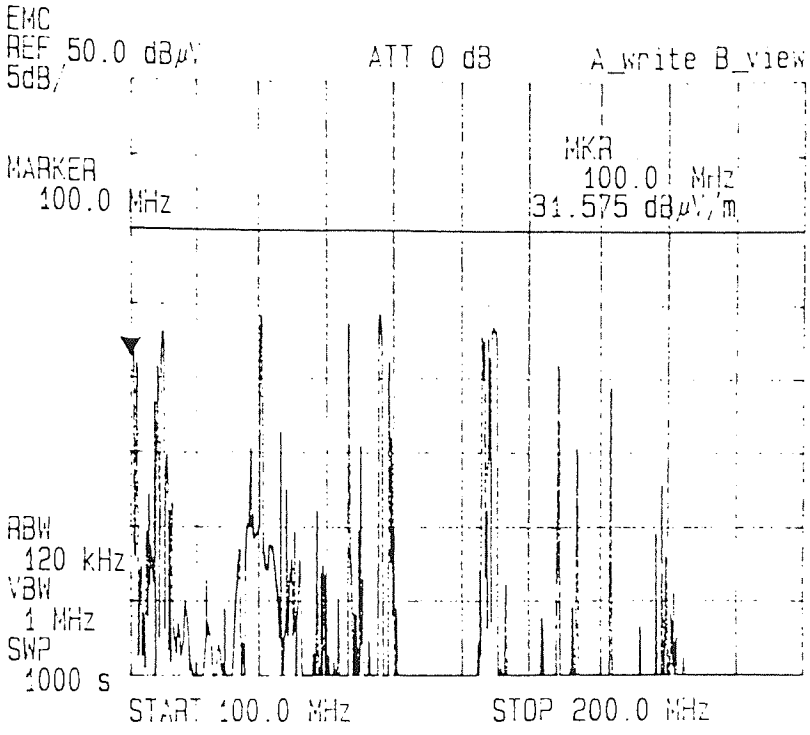

a: Background Radiation

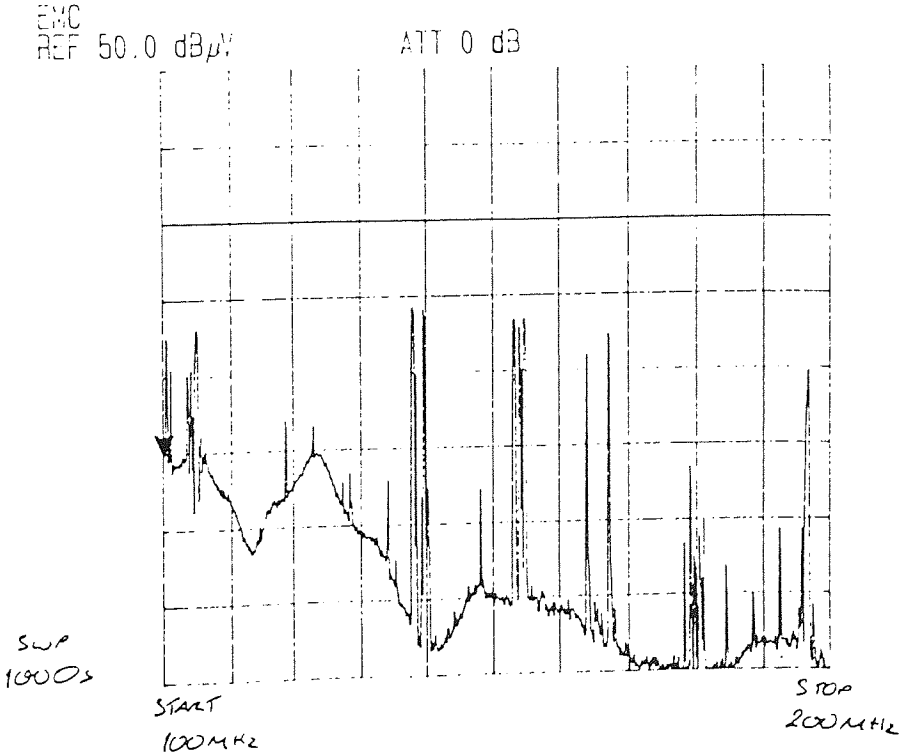

b: Drive Plus Background Radiation

Figure 4.6: Electromagnetic Radiation With the Antenna Vertical (100 - 200MHz)

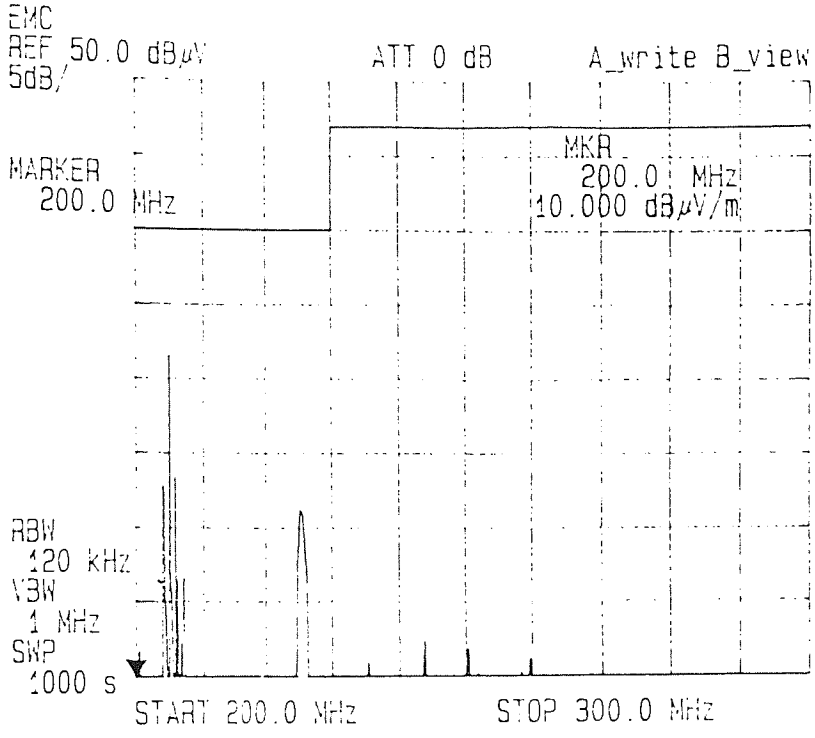

a: Background Radiation

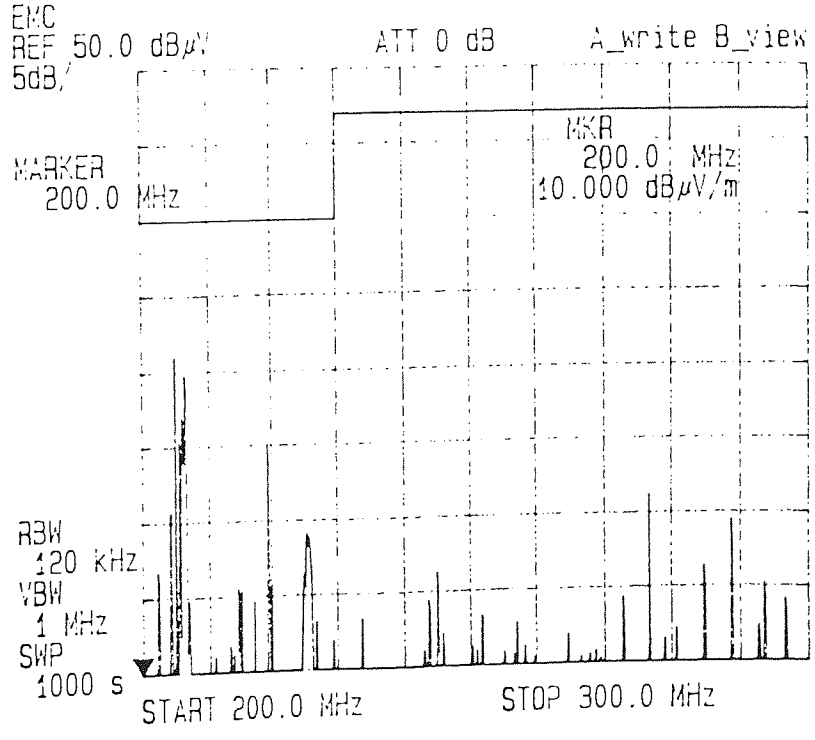

b: Drive Plus Background Radiation

Figure 4.7: Electromagnetic Radiation with the Antenna Vertical (200 - 300MHz)

The following two graphs, Figure 4.8, show the actual radiation from the drive when the antenna is both vertical and horizontal. This was obtained by subtracting the background radiation from the total radiation. The graphs only show the frequency ranges for which significant levels of radiation were measured (ie above 10dBμV/m = 3.16μV/m).

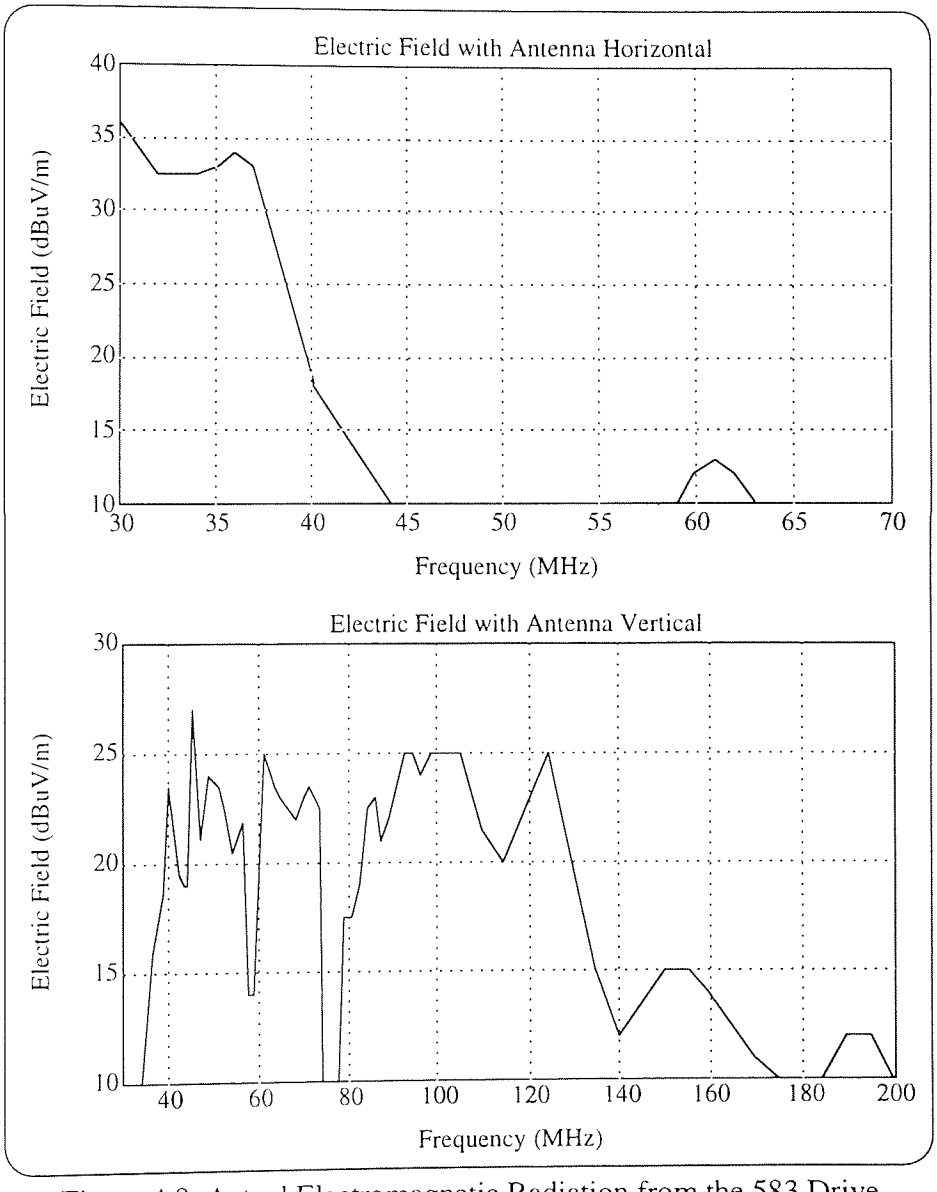

Figure 4.8: Actual Electromagnetic Radiation from the 583 Drive

The background radiation with the antenna vertical and horizontal consists of a series of spikes at set frequencies. This is because the background radiation is predominantly due to intentional interference, eg television and radio signals. Some of the peaks which

are evident in the background scans but not when the drive is switched on may be due to mobile phones or other equipment which generates electromagnetic waves in the desired frequency range (30-300MHz). From Figure 4.8 it can be seen that the majority of the radiation is measured when the antenna is vertical. The reason for this is that the majority of the emissions from the drive are in the vertical polarisation, for example the shielded cable drops down vertically to where the remainder of the cable is coiled.

As can be seen from the above graphs, Figure 4.8, the electromagnetic radiation falls to insignificant levels (ie below 10dBμV/m = 3.16μV/m) above 200MHz when the antenna is vertical and above 65MHz when the antenna is horizontal. It can also be seen that the majority of the radiation is detected when the antenna is in the vertical position. The graph shown below, Figure 4.9, is the modulus of the above two plots, and this was calculated from the following equation:

$$E_{mod} = \sqrt{E^2_{vert} + E^2_{horz}} \qquad \text{(eq4.3.1)}$$

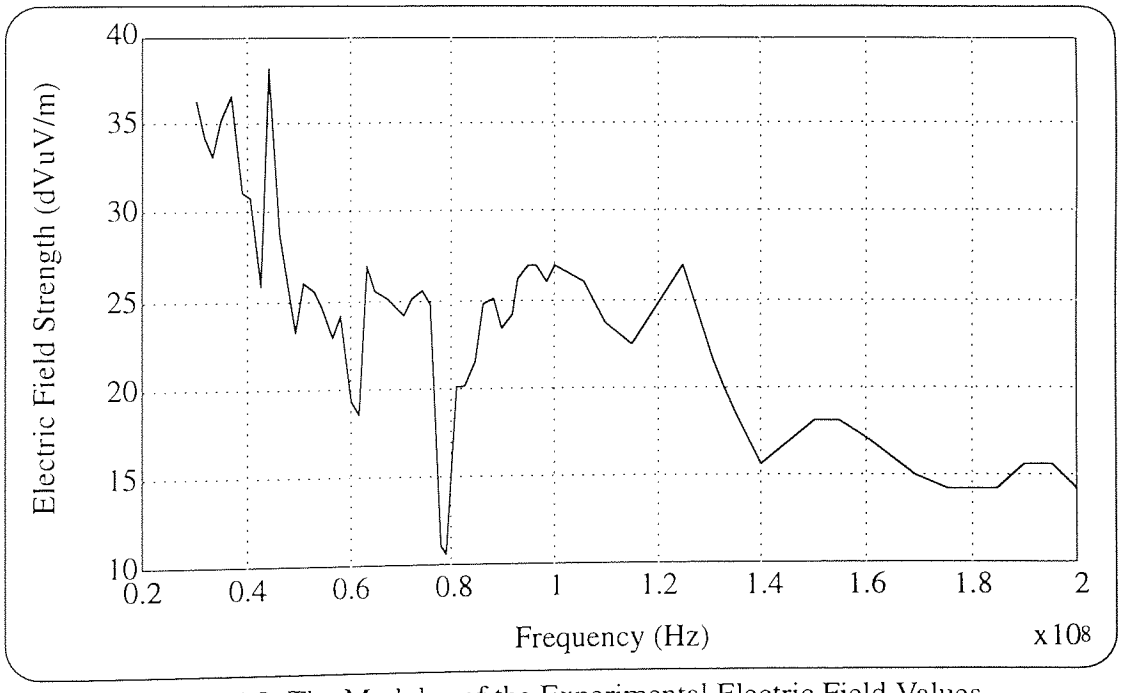

Figure 4.9: The Modulus of the Experimental Electric Field Values

The above plot was redrawn with a smooth curve passing through as many points as possible, as it was felt that the majority of the spikes present on the curve were due to the background radiation rather than what the drive was generating. The results of this can be seen in Figure 4.10.

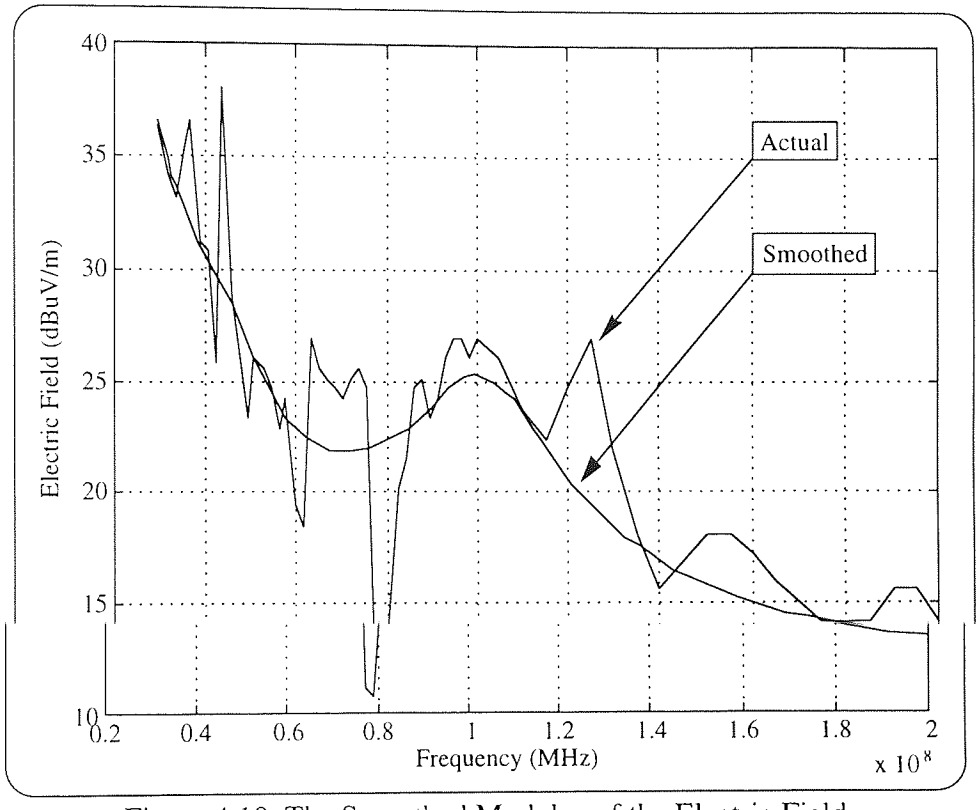

Figure 4.10: The Smoothed Modulus of the Electric Field

4.4 Experimental Problems

There were four difficulties encountered in the measurement of the electric fields. The first of these being that the results are highly dependent on the setup, and the chances are that if the experiment was repeated, a different set of results would be obtained. The error due to the setup can be minimised by attempting to place the drive, antenna and cables in the same position on the mesh at the same height. Even so it is not guaranteed that the results will be repeatable and Williams (1994) said that the repeatability of a good open area test site is in the order of +/-10dB. Also the measurement uncertainty of a good open area test site is in the region of +/-5dB.

Secondly the measurements of the background emissions and of the emissions with the drive switched on were made at different times on the same day (maximum difference was two hours). It is not known what the level of background radiation is at the time the measurements were made, but as the background measurements were made on the same day as the actual measurements, they were assumed to be the same.

The third problem with the test, was associated with its location. Ideally it should have been situated on a piece of flat ground, at a distance of several wavelengths from any obstructions to the radiation. In fact the ground plane was situated in a car park, in close proximity to overhead power cables, a metal framed building and a road, and any one of these items could have had an affect on the results, but the background measurements should have eliminated these problems.

The final problem concerned whether the noise measured from the drive was actually from the drive or from the motor. As the author knew of no way of determining whether the noise was coming from the drive or the motor it was assumed that all the noise came from the drive and the cables. This was a reasonable assumption as the motor casing was made from cast iron and should in theory prevent any radiation generated within the motor from reaching the antenna.

4.5 Summary

This chapter presented the test rig used for measuring the radiated emissions from the drive, along with the procedure used in making the measurements. The results obtained from the test rig were presented, with the antenna in both the vertical and the horizontal position. The results for the antenna in the vertical and the horizontal positions where combined to give the modulus of the results. Finally a number of problems associated with the test rig and its inability to produce repeatable results were identified.

Chapter 5

Finite Element Modelling

5.1 Introduction

The second part of this research was to determine a method to predict the electromagnetic radiation emanating from the 583 drive. Two methods for predicting this were considered. The first method, which is the subject of this chapter, is Finite Element Analysis (FEA). The second method, which is discussed in chapter 6, is Transmission Line Matrix (TLM) modelling.

The basic idea behind this part of the work was to set up a physical model of the drive which, unlike the SABER model, would take into account the physical dimensions of the drive and the various cables associated with it. The sources that were developed previously using the SABER model were then dropped onto this physical model and the radiated field calculated using the finite element package.

The FEA package available was PC-OPERA (Vector Fields (1995)), which is a two dimensional FEA package. A two dimensional package was used as it was thought that it would be feasible to produce a model of the drive in two-dimensions that would correctly predict the radiated emissions. Ultimately it was thought that it would be quicker to build a model of the drive in two-dimensions rather than building a complete three dimensional model whilst still producing data within acceptable limits of accuracy.

A description of PC-OPERA can be found in appendix A2.2.

5.2 The Finite Element Method

The finite element method is a numerical technique in which the equations governing the problem are represented in a matrix format and are then solved to determine the solutions to the problem.

There are basically four stages in generating and solving a finite element model, which are:

1. PHYSICAL MODEL: this is where the problem is defined in terms of its geometry, materials etc.
2. MATHEMATICAL MODEL: the decisions concerning solution potential and boundary conditions, as well taking advantage of any symmetry.
3. NUMERICAL MODEL: the discretisation of the geometry and the choice of interpolation functions.
4. ALGEBRAIC MODEL: the equations are solved to give a solution to the initial problem.

The physical model will consist of the geometry of the device being modelled, along with the material properties. The physical boundaries of the problem must also be considered at this point. Any sources that are present in the device will also be included in this stage. A source will generally take the form of a voltage or a current, but current density and charge density may also be used. Laroussi & Costache (1993) presented a finite element model where the sources used took the form of a measured value of the electric field in the near field, which was then used to generate the electric field in the far field. Figure 5.1 shows the physical model of a single pcb track on a dielectric substrate in two dimensions, the physical boundary in this case would be taken as the metal box surrounding the system.

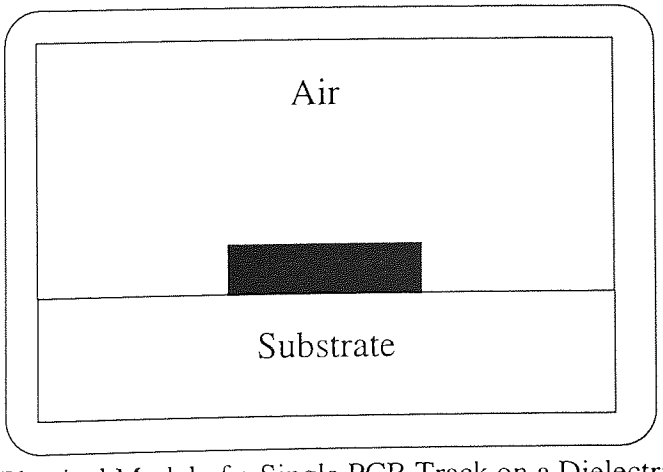

Figure 5.1: Physical Model of a Single PCB Track on a Dielectric Substrate

The model is then turned into a mathematical representation by firstly taking advantage of the symmetry of the problem so only half of it has to be modelled, see Figure 5.2. Since the potential is related to the field strength by:

$$E = -\nabla V \qquad \text{(eq5.2.1)}$$

Where:

E - is the field strength

V - is the potential

The potential must be set at one point in the problem at least, to make the solution unique.

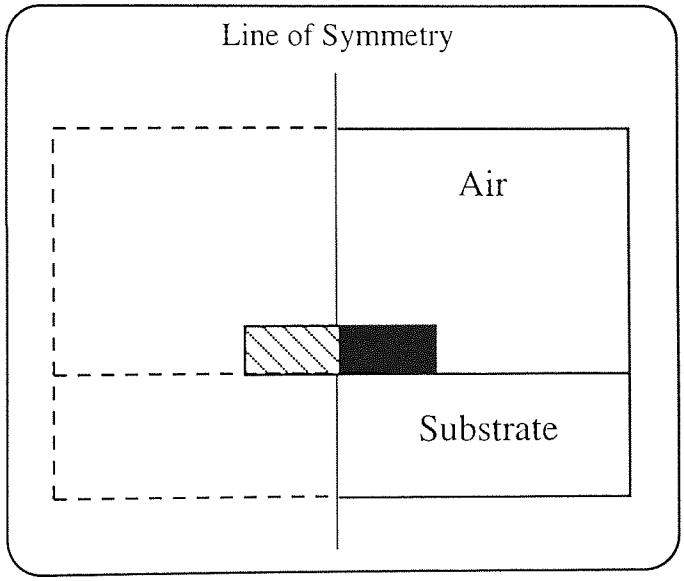

Figure 5.2: Physical Model of a Single PCB Track on a Dielectric Substrate Taking Account of the symmetry of the problem

The boundary conditions must also be set at this stage, and they are an essential part of the finite element process as they limit the physical size of the problem. The actual choice of boundary conditions is critical as they will significantly affect any results obtained. The boundary conditions that were available within PC-OPERA were:

1. Setting the potential (V) on the boundary to a specific value.
2. Setting the derivative of the potential (V) on the boundary to zero.

The discretisation of the geometry involves breaking the problem area down into a number of elements, which are normally triangular in shape for two-dimensional nodes, see Figure 5.3, and for three-dimensional problems they are normally tetrahedral shaped. The interpolation is how the potential changes between the nodes, the two functions that are normally used are linear and quadratic. Quadratic interpolation is the more accurate of the two, but will generally take longer to run.

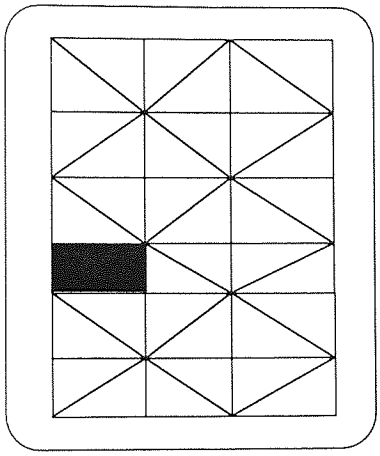

Figure 5.3: Discretised Geometry of a Single PCB Track on a Dielectric Substrate

The algebraic model is where all the above stages are combined together to generate a set of simultaneous equations, one for each node. The coefficients of these equations are then combined together to form the following matrices:

$$[K] \{ U \} = \{ F \} \qquad \text{(eq5.2.2)}$$

where:

[K] - is the stiffness matrix, which represents the shape and medium of the problem

{ U } - is the vector of unknown voltages or currents

{ F } - is the vector of the voltage or current sources

These equations will then be solved, and if the problem is non-linear this would be repeated until convergence is reached

5.2.1 Two-Dimensional FEA versus Three-Dimensional FEA

There are two types of finite element model, the first being two-dimensional where everything is modelled in a plane and the plane which is not modelled is assumed to have infinite thickness, see Figure 5.4. The second type is three-dimensional, which is where the actual problem geometry is modelled three-dimensionally.

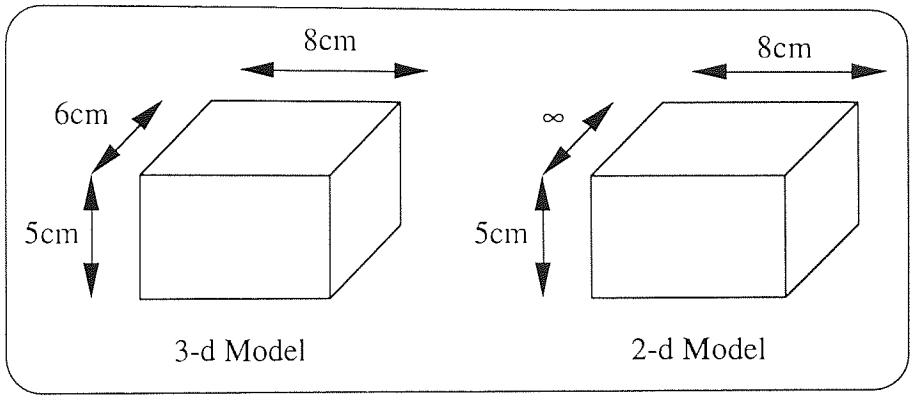

Figure 5.4: Graphical representation of a cube in 2-d and 3-d

A two-dimensional model is usually simpler to set-up and much quicker to solve than a three-dimensional one, but a three-dimensional model will generally give more accurate results. The reason for this being that an electromagnetic field is not a two-dimensional concept, and when the field is modelled in two-dimensions one of the planes of the field is assumed to be insignificant.

Two-dimensional finite element analysis has been used successfully in the modelling of devices that possess some sort of symmetry, eg electric motors and transformers. Boglietti et al (1990) showed how two-dimensional finite element analysis could be applied to the analysis of a brushless dc motor.

5.3 Physical Model Structure

As the finite element package chosen was two-dimensional, the issue of which plane or section through the drive should be modelled was raised. The section that was taken was chosen because it passed through the areas of the drive which were most likely to be producing significant levels of radiation, and also through the point in space where

the field was measured. This section thus allowed the finite element model of the drive to generate the maximum amount of emissions, and also for the results obtained to correspond with the measured values for the emissions from the drive. With the 583 drive these areas appeared to be the following:

1. The IGBT's which were switched with a PWM waveform at 1.6kHz.
2. The shielded cable which connected the motor to the drive. Radiation was still able to escape from the open ends of the cable and also from the common mode currents which were flowing in the shield.
3. The short lengths of cable which connected the IGBT's to the shielded cable.
4. The DC link, which had a high frequency component due to the switching of the IGBT's.

The motor was not modelled as it was assumed that it would produce minimal radiation as it was contained within a cast iron casing which in theory would prevent any radiation generated within the motor from reaching the antenna.

The control board of the 583 had a switching frequency of 12MHz, but it was thought that the radiation developed by the control board would be insignificant as the currents involved were so low.

The architecture of the 583 drive was such that the above four components listed above could be modelled in a single plane. The only change made to the architecture was that the shielded cable was modelled as being laid out in a straight line, whereas in practice it was coiled. The reason for this change was the difficulty in producing a realistic model in two-dimensions of the coiled cable, and also to retain the mesh accuracy.

The second point that had to be considered when producing the finite element model was that it had to conform to the test rig used to make the radiated measurements (see chapter 4 for details). This did not cause any problems as the architecture of the test rig leant itself to being modelled in two dimensions, see Figure 5.5 below.

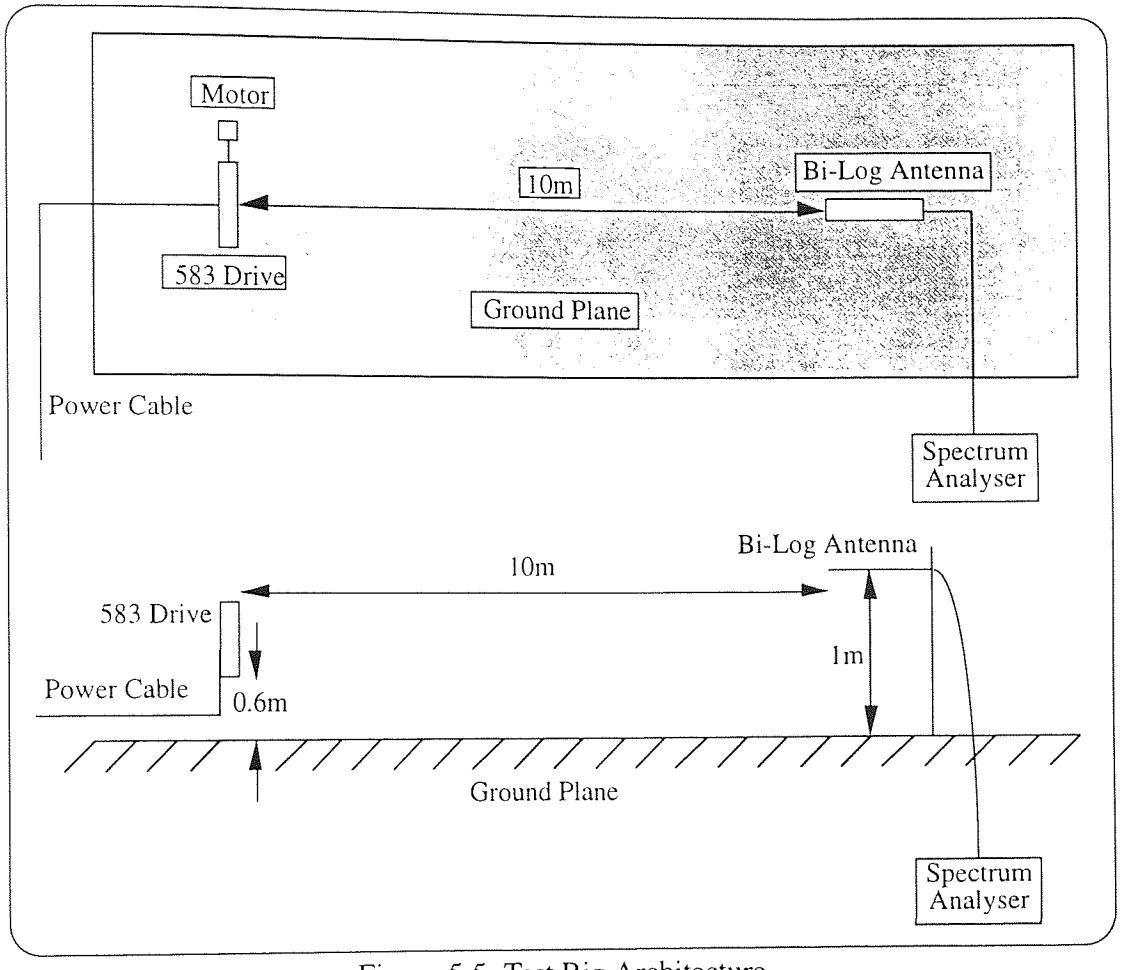

Figure 5.5: Test Rig Architecture

5.3.1 Shielded Cable and the Ground Plane

The shielded cable used in the experimental work consisted of four stranded copper cables enclosed in a steel mesh, see Figure 5.6. The four wires are used as the three phases to the motor and the earth. As there should be no current flowing down the earth wire, only three of the wires were modelled. The wire model was constructed from a rectangle of size 2.5×10^{-3}m by 5m with the properties of copper (ie $\mu_r=1$ and $\varepsilon_r=1$), a length of 5m was chosen because this was what was used in the experimental work. The entire cable was modelled by one of these wires, which was excited with the summation of the currents flowing down the wires.

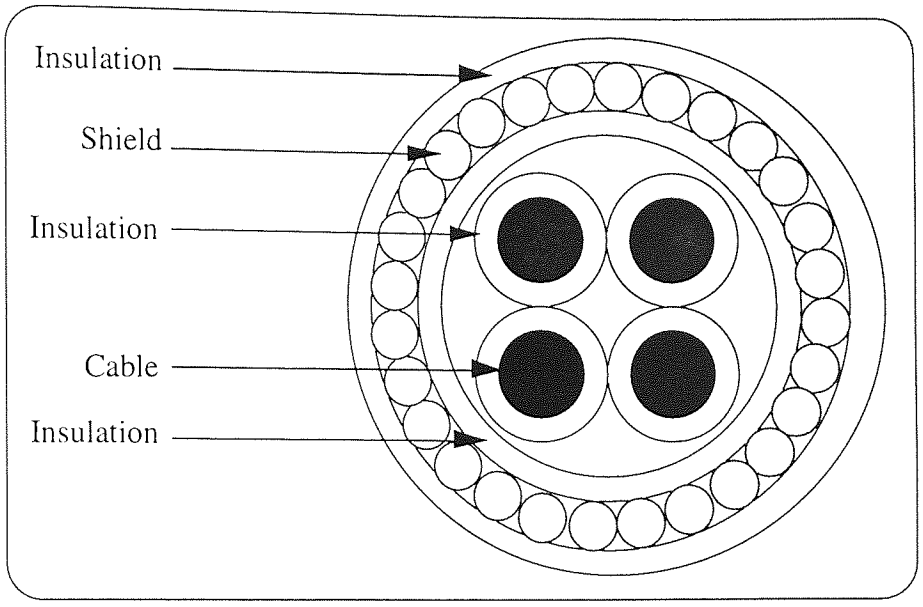

Figure 5.6: Structure of the Shielded Cable

The shield has two purposes, which are:

1. To prevent external electromagnetic fields from influencing the signals carried on the wires.
2. To prevent radiation generated by the internal cables from reaching any external equipment.

The shield will allow a certain amount of the radiation to pass through it, as it is constructed from a steel braid, but it will only be the very high frequency (ie above 100GHz) components that will pass through it, as the holes in the braid are very small (ie less than than a mm). This can be ignored in this model as the highest frequency of interest is 300MHz. As the shield is connected to ground it is an important path for the common mode currents which in turn play an important part in the generation of the radiation.

To reproduce this situation in the finite element model two methods were considered. The first method was to apply boundary conditions to the edges of the cable model, however this method was rejected as it allowed no way of applying the common mode currents to the model. The second method, which was the one that was used, was to place two strips on the outside edges of the cable model and to give these strips the properties of steel (ie μ_r=2000 and ε_r=1). However this method did have certain

drawbacks as the two extra thin strips dramatically increased the number of nodes and elements required, and hence increased the simulation time, and the solution errors. The effect of the shielded cable model is for the fields to be deflected away from it and to squirt into and out of the ends of the cable where there is no shield. The insulation on the cable was not modelled as it was made of plastic and would be transparent to the radiation generated by the sources.

The ground plane used during the experimental work was modelled by applying the boundary condition of the tangential and normal electric and magnetic fields equating to zero at the point in the model where the ground plane would have been.

5.3.2 The 583 Drive

As stated above there were three areas of the drive that were likely to produce significant emissions:

1. The IGBT's which were switching in a PWM waveform at 1.6kHz.
2. The short lengths of cable which connected the IGBT's to the shielded cable.
3. The DC link, which had a high component due to switching of the IGBT's.

A fourth area of the drive was also modelled which would not radiate, but would have an effect on the radiation. This being the heat sink, which was constructed form a piece of aluminium, and would in theory absorb some of the radiation and reflect the remainder of the radiation that was incident upon it.

The models for the DC link and the cables connecting the IGBT's to the shielded cable were modelled in a similar way to the cables in the previous section, by modelling them as an area in the finite element mesh with the same physical sizes and relevant material properties. The material properties used being:

1. DC Link, μ_r=1 and ε_r=1 (copper).

2. Cable between the IGBT's and the shielded cable, μ_r=1 and ε_r=1 (copper).

As with the shielded cable model the insulation on the wires was ignored as it would be transparent to the fields generated.

The IGBT's were modelled as a rectangle of size 1.5cm x 2cm, which was the actual size of a third of the IGBT stack used in the 583 drive. The material properties applied to this area were for an ideal conductor (μ_r=1 and ε_r=1), as the actual materials within the IGBT stack were not known.

The heat sink was modelled as a rectangle of size 5cm x 22.5 cm, which was the outside dimensions of the heat sink. The reason that the individual fins were not modelled was that to model each fin would have caused a significant rise in the amount of nodes and elements as each fin would have required a fine mesh to model it to the required accuracy. This mesh would have significantly slowed the model down. Also it was not thought that the fins on the heat sink would not have a large effect on the final solution as they faced away from the antenna. The material properties used for the heat sink were for aluminium (μ_r=1 and ε_r=1).

The detail of the model of the drive can be seen in Figure 5.7.

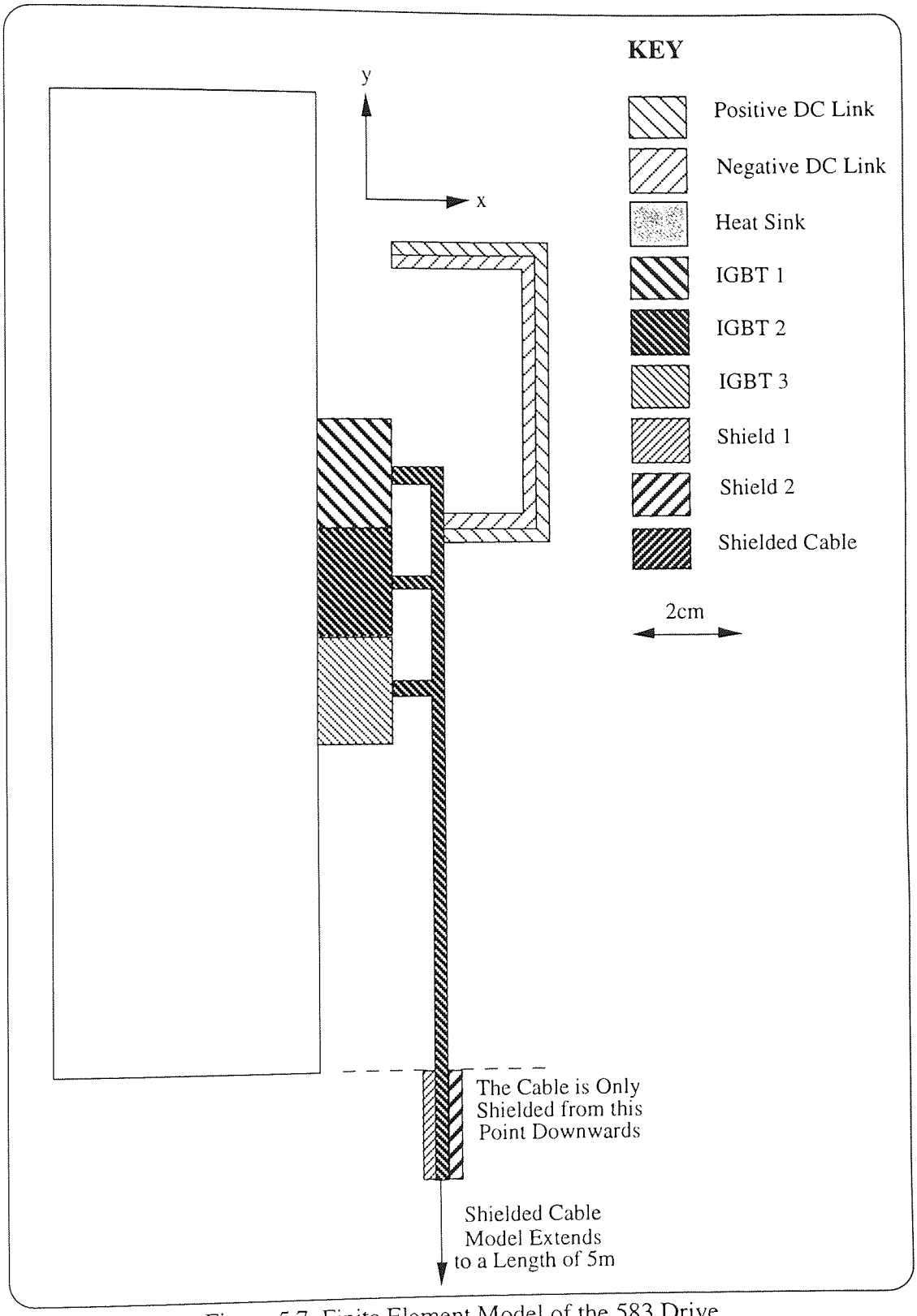

Figure 5.7: Finite Element Model of the 583 Drive

5.3.3 Boundary Conditions

In reality the finite element problem to be solved has infinite size (ie the electromagnetic waves can propagate away from the drive without being reflected back towards the drive). In practice it is not possible to model an infinite system, so the physical size of the problem had to be constrained with boundary conditions.

Boundary conditions have two purposes in finite element analysis, these being:
1. They limit the physical size of the problem so that it becomes computationally manageable.
2. Partial differential equations as used in finite element analysis have an infinite number of solutions. The boundary conditions set initial values which limits the number of possible solutions.

Electromagnetic fields are rarely contained in a closed domain (ie in a steel box with no openings), so they will actually propagate to great distances from the source. In practice at distances greater than a few wavelengths any changes to the far field will not affect the field near the source. The problem boundaries were extended to 15m on each side of the drive, and it was assumed that the boundary conditions at this distance from the drive would have a minimal effect on the solution.

Another method that was used to reduce the effect that the boundaries have on the solution is 'ballooning', this is where rings of increasing element sizes surround the areas of interest and minimise the effect that the boundary has on the problem area. Figure 5.8 shows how this technique was used. Although on the actual model five rings of increasing element size were used.

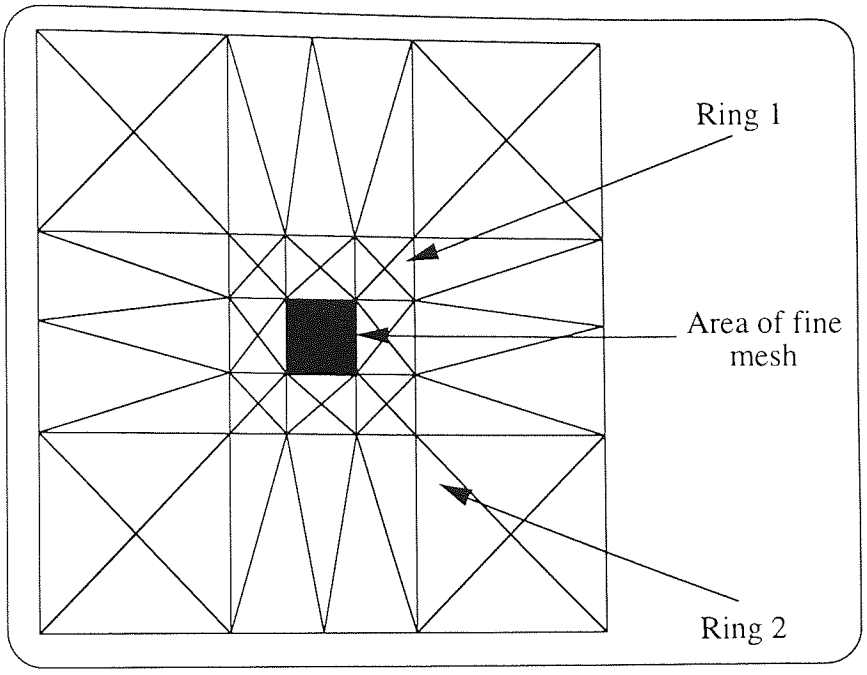

Figure 5.8: Ballooning

The field in the finite element problem was monitored at a distance of 3m from the drive rather than the 10m used during the experimental work, this again reduced the effect that the boundary conditions would have on the solution by not taking measurements in close proximity to the boundaries, as the solution boundaries were set at a distance of 15m from the drive.

The results from the finite element analysis, which were calculated in the near field, were transferred to a distance of 10m by taking advantage of the fact that the field strengths are inversely proportional to the distance from the source. This relationship comes from:

$$H_{3m}\,(dB) \propto \frac{1}{r_{3m}} \propto -9.54\,(dB) \qquad \text{(eq5.3.1)}$$

$$H_{10m}\,(dB) \propto \frac{1}{r_{10m}} \propto -20\,(dB) \qquad \text{(eq5.3.2)}$$

Subtracting (eq5.3.2) from (eq5.3.1) gives:

$$H_{3m}(dB) - H_{10m}(dB) = (-9.54(dB)) - (-20(dB)) = 10.46(dB) \qquad \text{(eq5.3.3)}$$

$$H_{10m(dB)} = H_{3m(dB)} - 10.46(dB) \quad \text{(eq5.3.4)}$$

Equation 5.3.4 was applied to all the results obtained from the finite element model to transfer them from a distance of 3m to a distance of 10m from the drive.

As already discussed in section 5.3.1, boundary conditions were used to describe the reflecting ground plane. Even though these boundary conditions were situated in close proximity to the drive it did not matter as they were intended to affect the field around the drive. Boundary conditions were also applied on all four outer edges of the problem. The boundary condition chosen was for the normal components of the fields to be zero.

5.3.4 Sources

The finite element model was excited with the current sources generated from the SABER model (see chapter 3), all the sources were in the time-base. The model was excited in 7 regions, these being:

1. Positive DC link.
2. Negative DC link.
3-5. The three IGBT's.
6. The single cable representing the three phases within the shielded cable.
7. The steel shield on the shielded cable (ie the common mode currents).

The sources used for the positive DC link can be seen in Figure 5.9. A corresponding signal was applied to the negative DC link. As the system was modelled with the motor running freely, i.e near zero load, the average current on the dc link sums to zero.

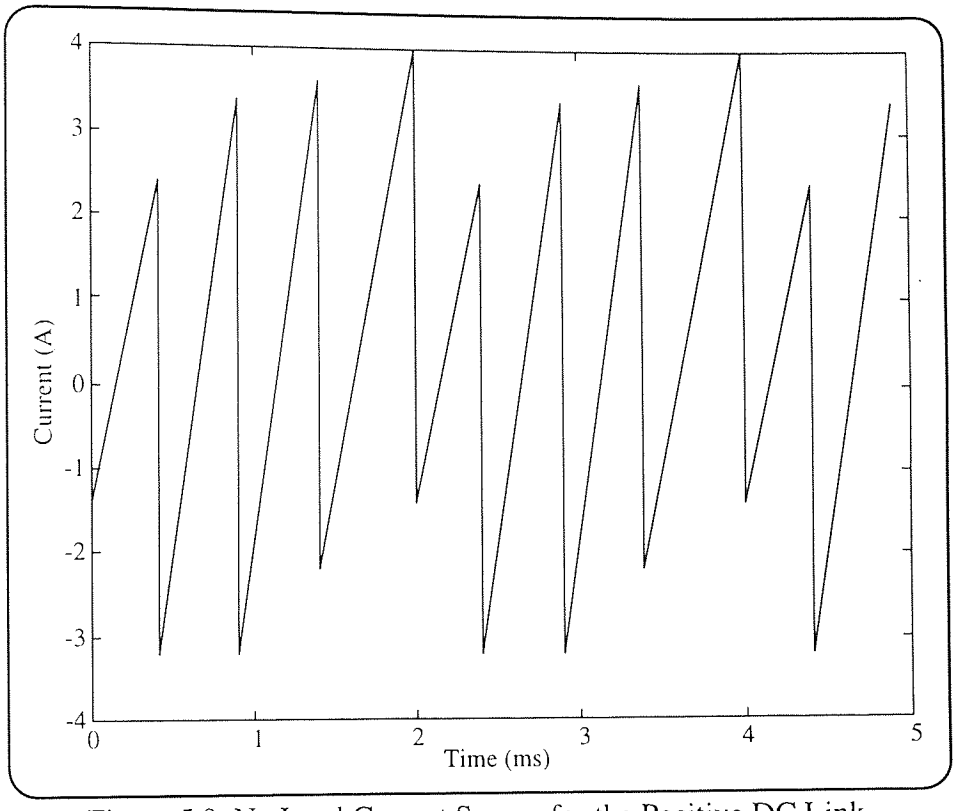

Figure 5.9: No Load Current Source for the Positive DC Link

The signal lines in the shielded cable was excited with the difference of the three currents that were being sent to the motor, and each current was 120^{o} out of phase. The difference of the motor current can be seen in Figure 5.10 below. The large number of spikes which were evident on the modelled waveform were also ignored because in reality these spikes are not so prominent.

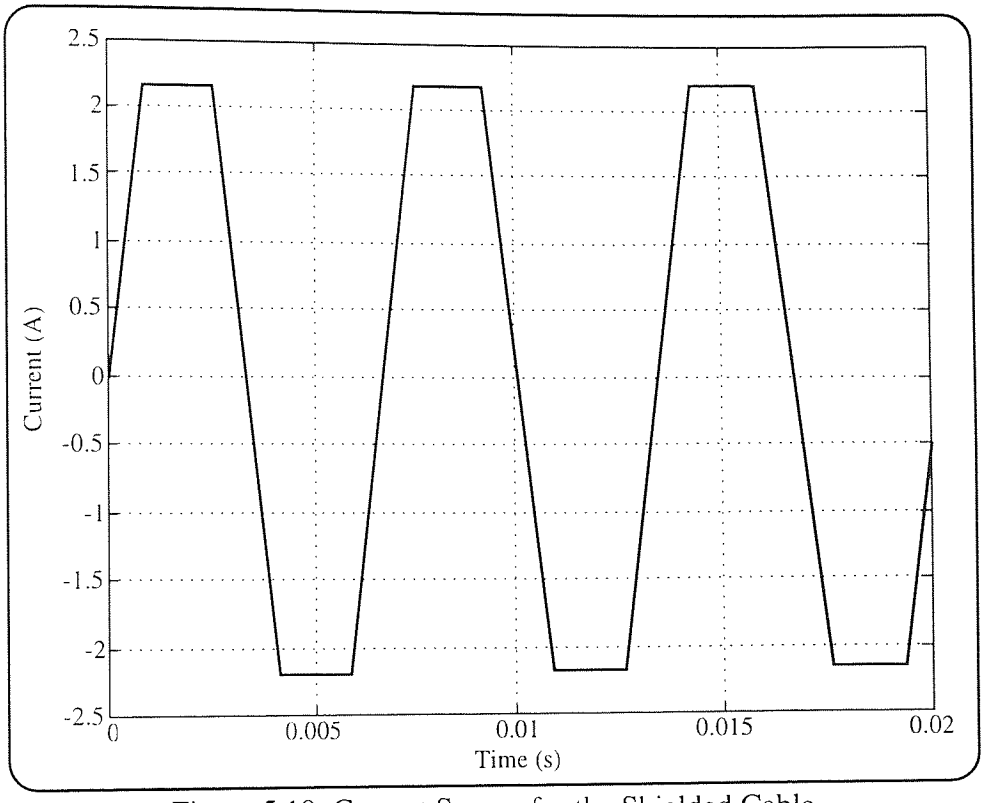

Figure 5.10: Current Source for the Shielded Cable

The IGBT's were excited with the current waveform that each IGBT generated as it was switched on and off with the PWM waveform. As with the shielded cable, each IGBT was 120^{o} out of phase. One phase of the IGBT current source can be seen in Figure 5.11. Again this waveform was generated using the SABER model presented in chapter 3.

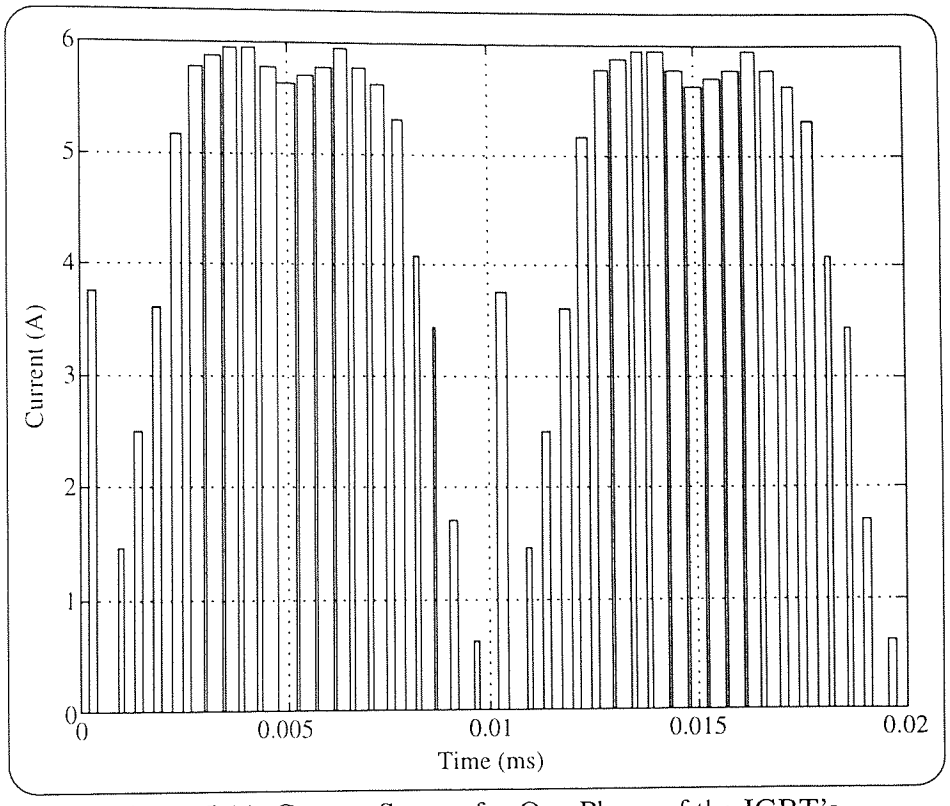

Figure 5.11: Current Source for One Phase of the IGBT's

The steel shield was excited with the common mode currents that were generated from the SABER model (section 3.7). These currents were what was deemed to be flowing in the shield of the shielded cable. As can be seen from Figure 5.12 the common mode currents have very high frequencies so are more likely to be responsible for the emissions than the lower frequency differential mode currents which are present in the IGBT's, the signal lines etc.

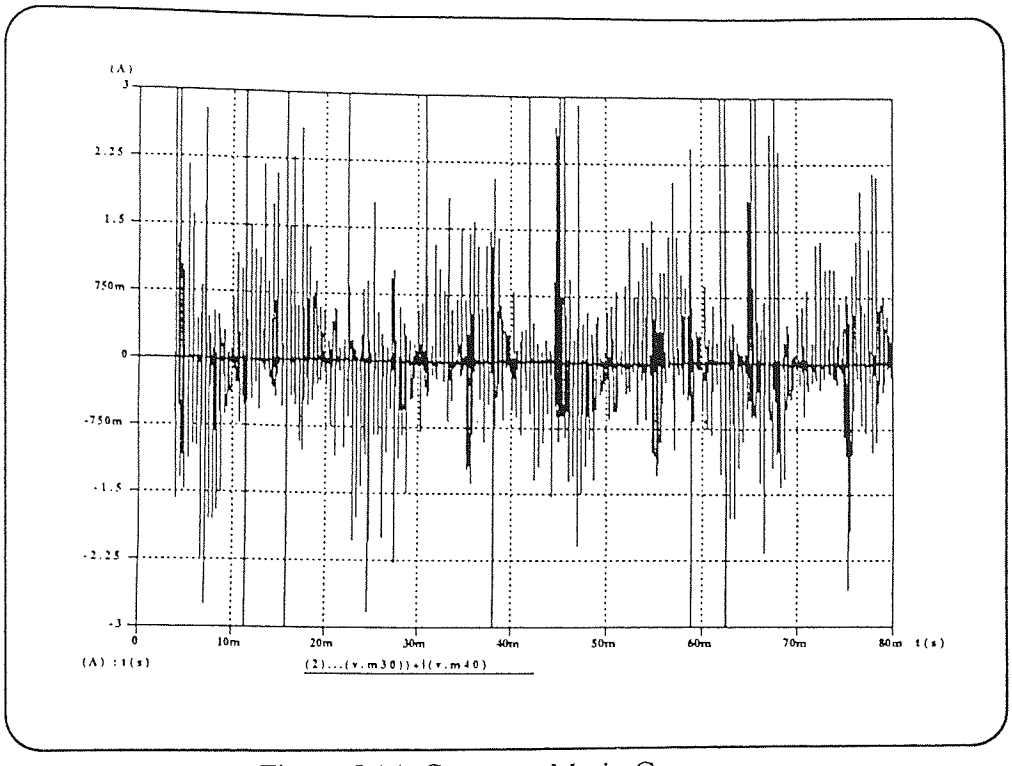

Figure 5.14: Common Mode Currents

5.4 Finite Element Simulations

The finite element model that was run had the following characteristics data:

Quadratic Elements - Each element (triangle) had six nodes, one at each of the corners and one at the mid-point of each side.

XY Symmetry - No symmetry has been taken advantage of in the model.

Vector Potential - Magnetic vector potential was used to calculate the fields rather than magnetic scalar potential as the regions of interest in the problem were not source free.

Magnetic Fields - Magnetic fields were calculated rather than electric fields, due to the fact that the sources that were used to excite the problem had units of A/m^2.

Simulation Time - Time taken to create and solve the equations was 315s.

3082 Elements - Number of elements (triangles) to model the system.

6225 Nodes - Number of nodes used to define the elements.

25 Regions - Number of separate ares that make up the model.

The reason that magnetic fields were used, was that the source units were in terms of current. For electric fields the source unit was in terms of charge and it was easier to determine the sources calculated using the SABER model in terms of the currents flowing in the circuit. The magnetic fields were converted into electric fields using the following equation, which takes advantage of the fact that when the field being measured is in the far field the electric field is related to the magnetic field by the impedance of free space (377Ω):

$$E(V/m) = H(A/m) \times 377\Omega \qquad \text{(eq5.4.1)}$$

When the electric field is in units of dBμV/m and the magnetic field is in units of dBμA/m equation 5.4.1 becomes:

$$E(dB\mu V/m) = H(dB\mu A/m) + 51.5 \qquad \text{(eq5.4.2)}$$

The package PC-OPERA calculates two error values, which are related to the field values and the mesh. The field values obtained from the finite element problem are calculated by differentiating the solution, this gives elemental values of the field and these values are averaged to give a smoothly varying field across the problem area, see Figure 5.13. Figure 5.13A shows the elemental values of the field of a problem, Figures 5.13B and C show how these field values would be averaged over the problem to produce a smoothly varying field over the whole area. The RMS error is a measure of the difference between the averaged and the elemental values, the weighted error takes into account the area of the elements when calculating the error. The values that were obtained for the above two errors were:

RMS error over the whole problem = 2.21%

Weighted RMS error = 0.22%

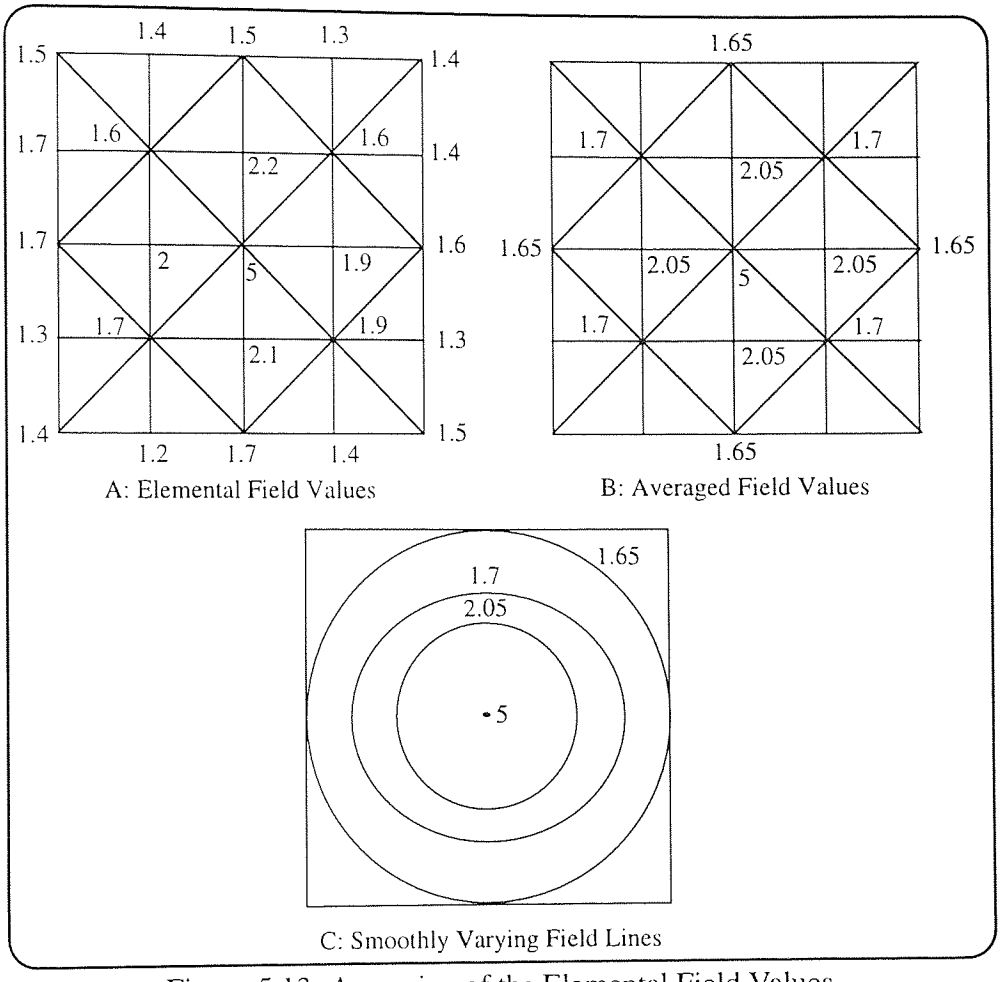

Figure 5.13: Averaging of the Elemental Field Values

The finite element model was run for a total time of 10ms, and this time corresponded to one cycle of the drive. A total of 303 time steps (t_{step} = 33μs) were taken for the initial simulation. The purpose of this simulation was to determine the approximate shape and the frequency of the electromagnetic wave. An assumption was made that at each time step the problem being solved could be approximated by a static solution. So the simulations were run as a series of static solutions at different times.

As the modelled results were in the time-domain and the experimental results in the frequency-domain, it was necessary to transfer the finite element results from the time-base to the frequency-base. A Fourier transform was used to make this conversion. The theory for the Fourier transform used can be found in section 3.8.2.

As was stated in section 3.8.2 it will only take the first few harmonics (eg 10) to represent the waveform in the frequency-domain to 95% accuracy. However the time period of the waveform from the finite element model was 3.33ms. Giving a fundamental frequency of 300Hz. So to obtain the Fourier transform for the correct frequency range (30MHz to 200MHz) it was necessary to calculate about 600,000 harmonics. Figure 5.14 shows the electric and magnetic fields in the frequency range 30MHz to 200MHz, the difference between the electric and magnetic fields corresponds to equation 5.4.2.

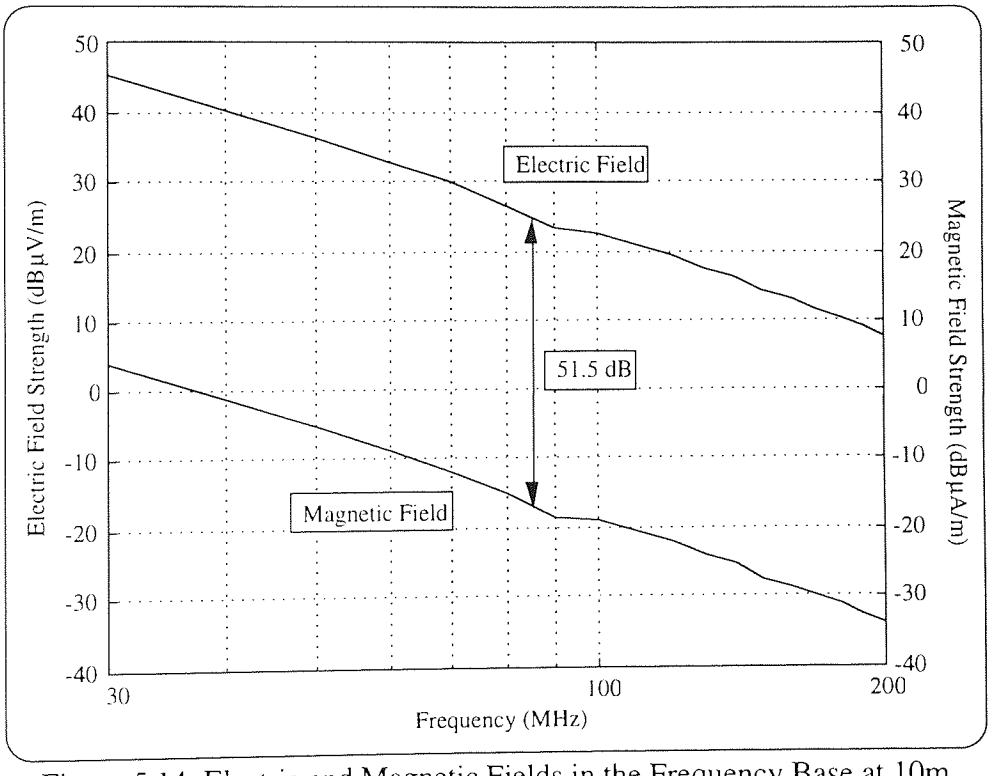

Figure 5.14: Electric and Magnetic Fields in the Frequency Base at 10m

A second set of finite element simulations were run, but this time the only sources that were applied were those for the shielded cable and also the common mode currents that were flowing in the shield. The reason for this was that it was suspected that the shielded cable would be a more efficient source of radiation than the drive. The shielded cable is electrically long (total line length is greater than a tenth of a wavelength), when compared to the frequencies of interest (at 30MHz λ = 10m and at 200MHz λ = 1.5m), so it behaves as a monopole antenna which is an efficient source

of emissions. The drive is electrically short (total line length is less than a tenth of a wavelength), when compared to the frequencies of interest, so it is a less efficient source of radiation, hence the majority of the radiation is likely to be produced by the shielded cable rather than the drive. It was also shown in the simulation with the only the shielded cable being excited that the primary source of the radiation was the common mode currents which were flowing in the shield. The reason for this is that the common mode currents are not balanced like the differential mode currents so the fields produced by them do not sum to zero, see Figure 5.15. The simulations with only the shielded cable being excited showed that the majority (95%) of the radiation was due to the currents flowing in the shielded cable and the common mode currents flowing in the shield.

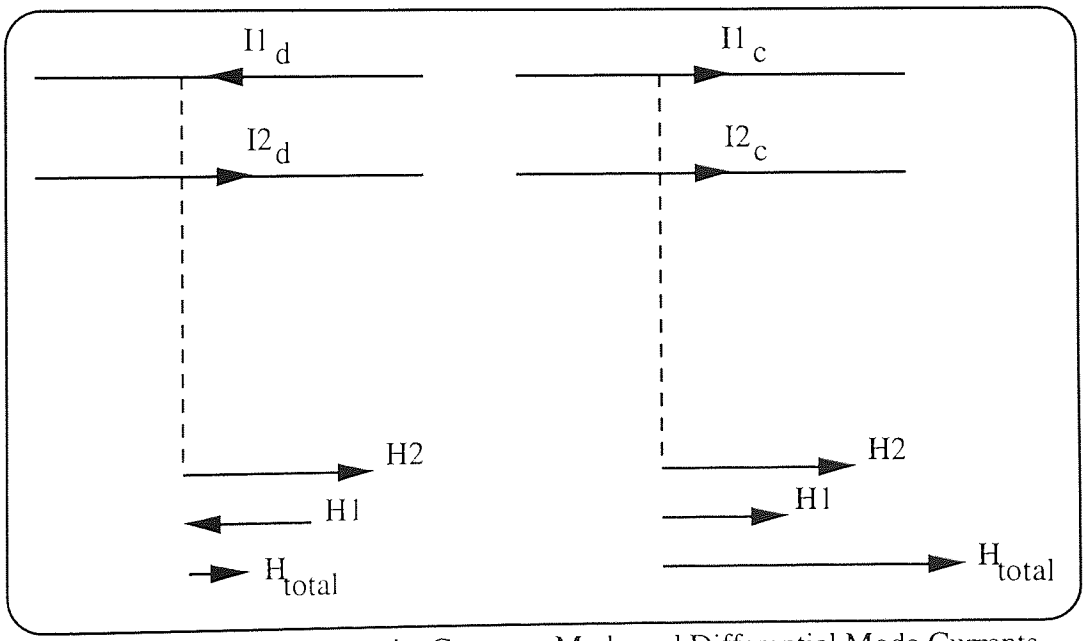

Figure 5.15: Fields Due to the Common Mode and Differential Mode Currents

5.4.1 FEA Results

The results obtained from the finite element model were compared to the measured values of the radiated field in the frequency range (30MHz to 200MHz), this comparison can be seen in Figure 5.16.

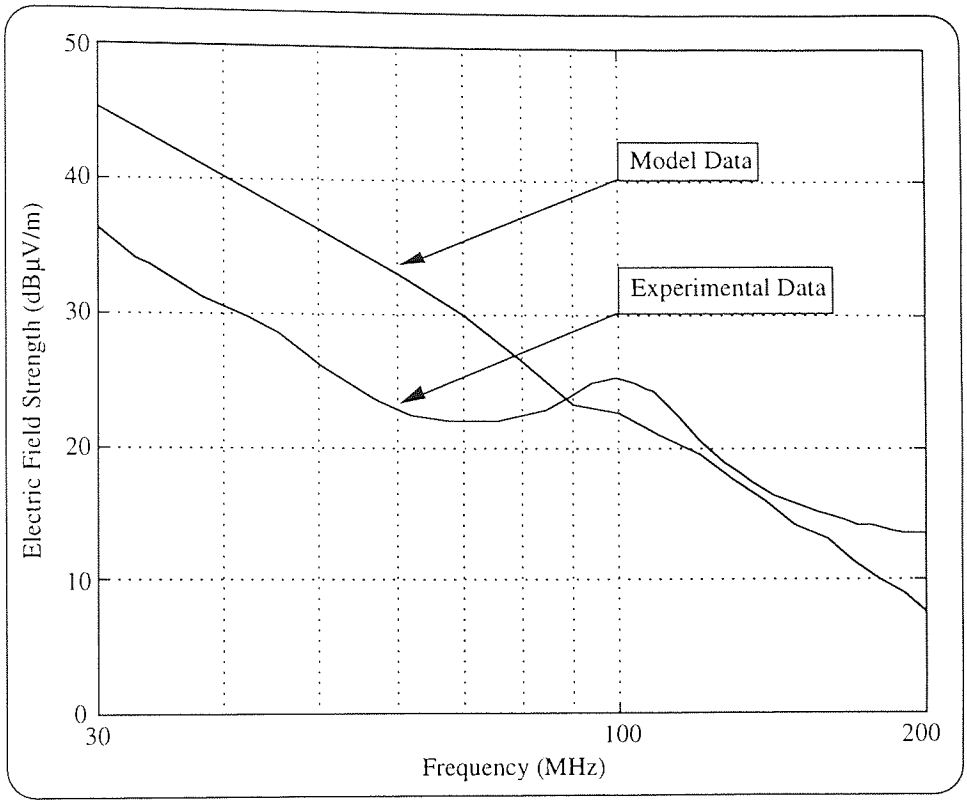

Figure 5.16: Comparison of Measured and Modelled Values for the Electric Field

As can be seen from the above graph, the modelled and the measured values both decrease in value by approximately -40dB/decade. The maximum error between the two sets of values is +10dB and -6dB, see Figure 5.17. The large error between the measured and modelled values is justified because of the measurement procedure (see chapter 4), which does not produce results which are 100% accurate and it is also highly unlikely that the same results would be obtained if the experiment was repeated. Therefore the modelled values can only be used as a guide to the level of the actual emissions.

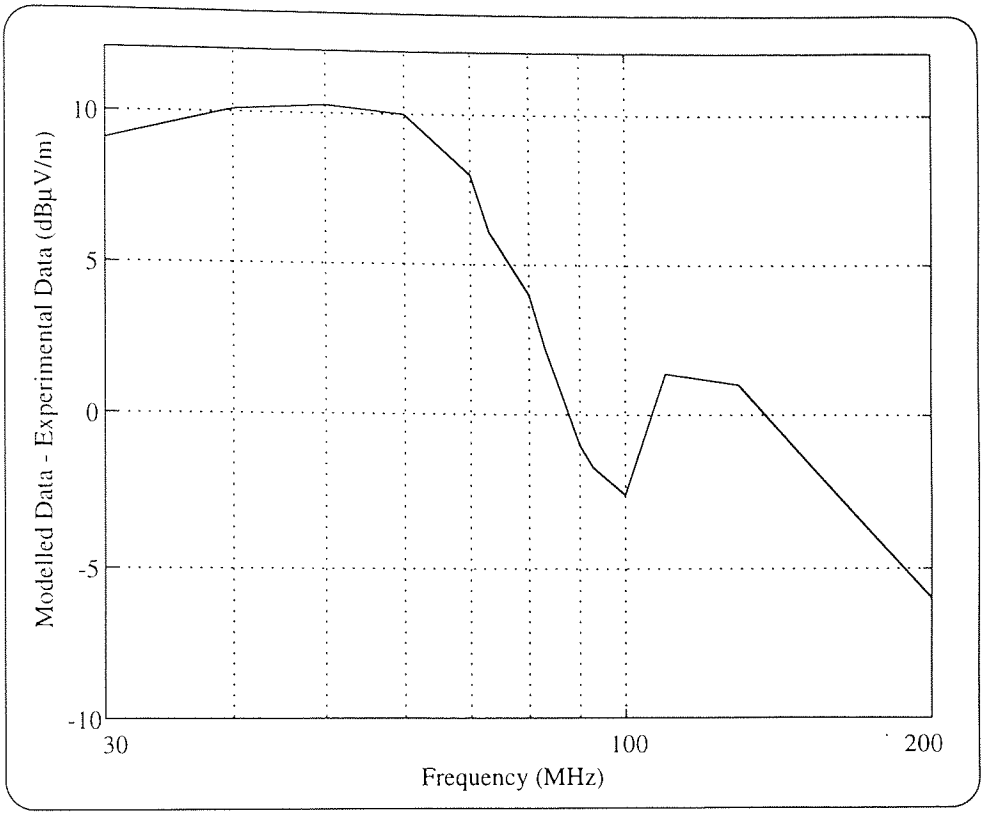

Figure 5.17: Error Between Measured and Modelled Values of the Radiated Field

As the results discussed above were generated from the model that only took account of the radiation generated by the shielded cable, this shows that it is feasible to obtain results for the radiation from the drive, which are comparable to the measured results to within +10dB and -6dB, by only modelling the shielded cable which connects the drive to the motor. However as the experimental results are assumed to only be repeatable to within +/-10dB, the model results may be more accurate than the measured results. This further justifies what was previously said about the model results can only be used as a guide to the level of emissions from a drive. If a more accurate model is required it is necessary to model the drive, ie the components and the tracking on the PCB, but this will result in models which take longer to set up and also longer to run.

5.5 Problems With Two-Dimensional Finite Element Modelling

A number of problems with the two-dimensional method were identified, during the modelling and the simulation of the 583 drive. The first being that the problem is assumed to be infinitely thick in the z-direction whereas in reality the system has a finite

thickness in the z-direction. This can be seen in Figure 5.20 where in the three-dimensional model the wire has a finite length in the z-direction, but in the two-dimensional model the wire has infinite length in the z-direction.

The second problem was that the currents were forced to flow either in or out of the page (z-direction) rather than across it (x or y-directions), and in reality the currents do not flow in the z-direction as they flow down the wires (i.e in the y-direction in the model). This is also shown in Figure 5.18 where the current can flow in the x, y or z-direction in the three-dimensional model, but in the two-dimensional model it can only flow in the z-direction.

Using a two-dimensional finite element package meant that only one plane of the problem could be modelled, with the 583 drive the simulation outcome suggests that a two-dimensional package can give acceptable results. However not all problems are going to be able to be modelled in a single plane, and when this problem occurs a three-dimensional package will have to be used. In theory this problem could be overcome by modelling a number of different planes and then extrapolating between them to determine the values of the fields, but this could make relatively simple problems highly complicated and time consuming to solve.

It was only possible to predict the fields in the x and y-directions when using two-dimensional finite element theory, in practice it is desirable to know the field values in all three directions. The only solution to this problem is to model the drive using a three-dimensional package.

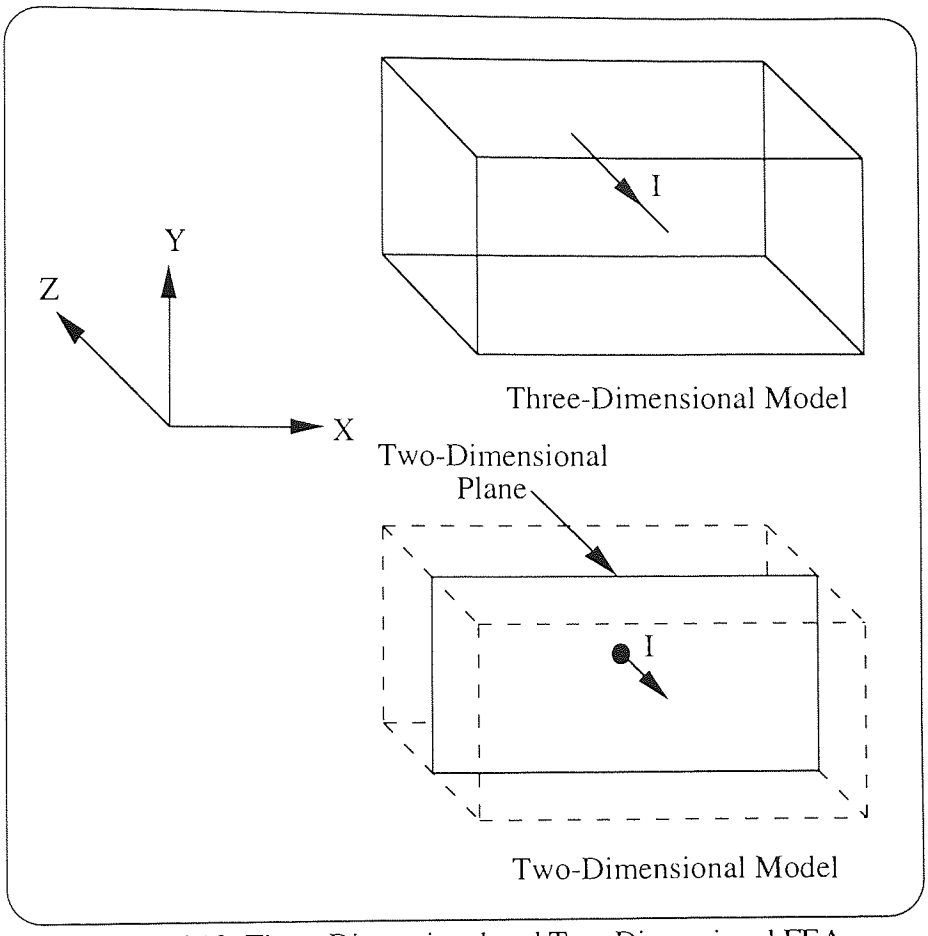

Figure 5.18: Three-Dimensional and Two-Dimensional FEA

5.6 Summary

This chapter presented a physical model of the 583 drive set up in a two-dimensional finite element package, PC-OPERA. The structure of the model took into account the areas of the drive that were most likely to radiate, as well as the structure of the test rig used to measure the radiated emissions.The parts of the drive which were included in the model were the IGBT's, the DC link and the shielded cable which connected the drive to the motor. The sources which were used to excite the model were taken from the SABER model which was previously developed in chapter 3, and were in the time base. The model was run as a series of static problems at different times, and this resulted in a waveform in the time base of the radiated emissions. The emissions in the time-domain were converted to the frequency-domain by performing a Fourier transform on the waveform. The electric field was calculated in the frequency range 30MHz to 200MHz. When the modelled electric field was compared to the measured

values an error of +10dB and -6dB was found to exist. Due to the fact that the measurement cannot produce result that are accurate and repeatable, the modelled values can only be used as a guide to the level of the actual emissions. Finally it was determined from the finite element model that the majority (95%) of the radiation was coming from the shielded cable, which was excited with the currents that the motor sees and also the common mode currents that were present in the shield that connected the drive to the motor.

The finite element modelling has shown that it is feasible to obtain results for the radiation from the drive, which are accurate to within +10dB and -6dB, by only modelling the shielded cable which connects the drive to the motor in two-dimensions. If a more accurate model is required it will be necessary to model the actual drive using a three-dimensional model, and to include the components used in the drive and also the tracking on the PCB. The trade off will be that this will result in models which take longer to set up and also longer to run.

Chapter 6

Transmission Line Matrix Modelling

6.1 Introduction

As was said in the previous chapter, the second part of this research was to determine a method of accurately predicting the electromagnetic radiation from variable speed drives. The first method, that has already been discussed was two-dimensional finite element analysis.

The second technique that was applied to predict the electromagnetic radiation, was the Transmission Line Matrix (TLM) method, and the obvious advantage that this had over finite elements was that it was a time-domain based method which was more suited to the sources used to excite the model which were in the time base.

Due to the fact that there is no commercial TLM modelling package available, the method was programmed using the language C++.

6.2 The Transmission Line Matrix Method

The transmission line matrix method was developed by Johns & Beurle (1971) as a new method for solving two-dimensional field scattering problems. The method is based on Huygens (1690) model of wave propagation which proposed that a wave front consists of a number of secondary radiators which generate spherical wavelets. These wavelets then form a new wave front which also generates spherical wavelets, and the cycle is reproduced to allow the wave to propagate through space and time.

The transmission line matrix method models space and any objects contained in the space as a grid of transmission lines constructed from inductors and capacitors whose values are determined from the permeabilities (inductance) and permittivities (capacitance) of the material being modelled. The fields in the space are modelled as either currents (magnetic) or voltages (electric) which propagate through the grid in the same way as an electromagnetic wave propagates through space. These currents and voltages are then analogous to the magnetic and electric fields respectively.

6.3 Basic Two-Dimensional TLM Theory

The basic two-dimensional series TLM node can be seen in Figure 6.1. The size of the node (Δl) is related to the time (Δt) taken for an electromagnetic pulse to travel from one node to the next by the expression:

$$\Delta t = \frac{\Delta l}{\sqrt{2}\, c} \qquad \text{(eq6.3.1)}$$

Where c is the speed of light in the in the material, and is determined by the equation:

$$c = \frac{1}{\sqrt{\varepsilon_o \mu_o}} = 299.86 \times 10^6 \text{ m/s} \qquad \text{(eq6.3.2)}$$

Where:

ε_o = permittivity of free space = 8.85×10^{-12} F/m

μ_o = permeability of free space = $4\pi \times 10^{-7}$ H/m

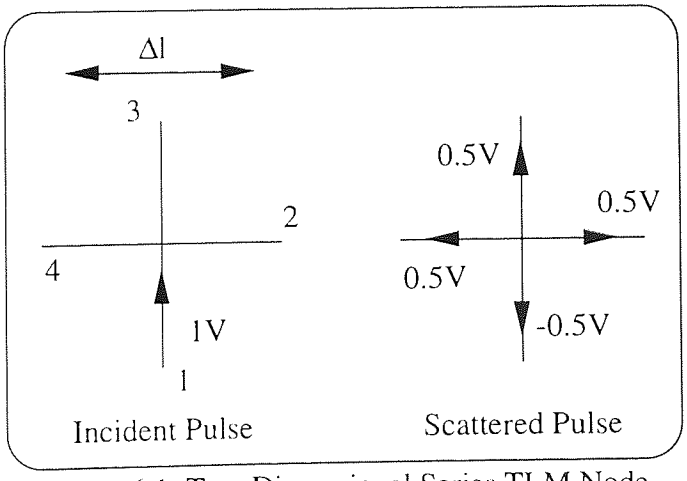

Figure 6.1: Two-Dimensional Series TLM Node

Figure 6.1 also shows how an incident pulse of unit value would be scattered when it reached the node, and this scattering can be represented by the following equation:

$$[V]^r = 0.5\,[S]\,[V]^i \qquad \text{(eq6.3.3)}$$

Where $[V]^i$ is the vector of the incident pulses and $[V]^r$ is the vector of the reflected pulses. The scattering matrix [S] takes the following form, for homogeneous materials:

$$S = \begin{bmatrix} -1 & 1 & 1 & 1 \\ 1 & -1 & 1 & 1 \\ 1 & 1 & -1 & 1 \\ 1 & 1 & 1 & -1 \end{bmatrix} \qquad \text{(eq6.3.4)}$$

As was previously said the basic building block for a two-dimensional TLM network is shown in Figure 6.1, the equivalent circuit model of this node can be seen in Figure 6.2, and it consists of 4 inductors each of value $L\Delta l / 2$ and a capacitor of value $2C\Delta l$. It can be shown by comparing the field equations to the voltage and current changes in the x and z directions that the following equivalences, Hoefer & So (1992), are true:

$$E_y \equiv V_y \qquad \text{(eq6.3.5)}$$

$$H_Z \equiv I_X \qquad \text{(eq6.3.6)}$$

$$H_X \equiv -I_Z \qquad \text{(eq6.3.7)}$$

$$\mu_n \equiv L \qquad \text{(eq6.3.8)}$$

$$\varepsilon_n \equiv 2C \qquad \text{(eq6.3.9)}$$

Where the subscript n denotes a parameter associated with a node.

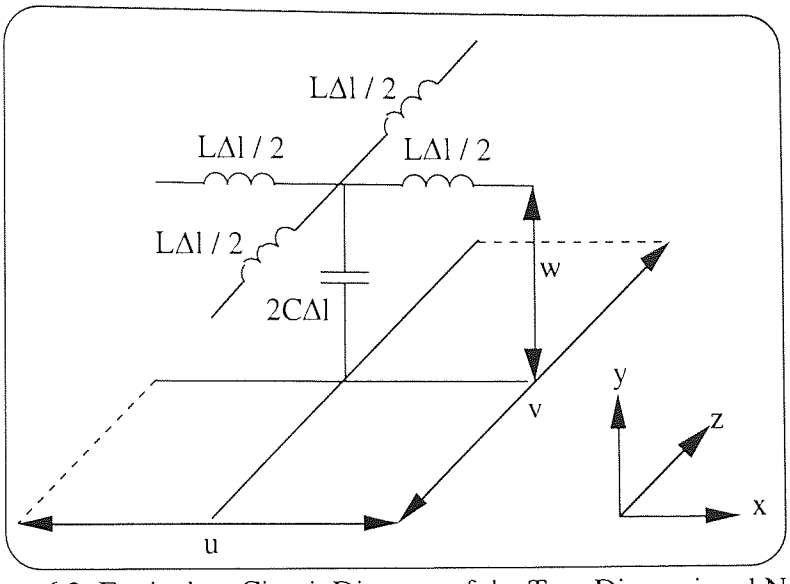

Figure 6.2: Equivalent Circuit Diagram of the Two-Dimensional Node

It is possible to model lossy inhomogeneous materials by the inclusion of a loss stub on the node to account for the changes in the permeability and permittivity of the material, these stubs having a length equal to $0.5\Delta l$. The inclusion of these stubs causes each node to have 5 pulses on it rather than 4, and the scattering matrix becomes:

$$s = \frac{1}{y}\begin{bmatrix} 2-y & 2 & 2 & 2 & 2y_o \\ 2 & 2-y & 2 & 2 & 2y_o \\ 2 & 2 & 2-y & 2 & 2y_o \\ 2 & 2 & 2 & 2-y & 2y_o \\ 2 & 2 & 2 & 2 & 2y_o-y \end{bmatrix} \qquad \text{(eq6.3.10)}$$

where:

$$y = 4 + y_o + g_o \qquad \text{(eq6.3.11)}$$

$$y_o = 4\,(\varepsilon_r - 1) \qquad \text{(eq6.3.12)}$$

$$g_o = \sigma Z_o \Delta l \sqrt{2} \qquad \text{(eq6.3.13)}$$

Where:

g_o - normalised characteristic conductance

y_o - normalised characteristic admittance

Δl - node size (m)

ε_r - relative permittivity

Z_o - wave impedance (377Ω)

σ - conductivity (S/m)

As was said previously the electric and magnetic fields are related to the voltages and the currents on the mesh, the only difference being with the inhomogeneous materials that the loss stubs have to be taken into account when calculating the fields.

6.4 Three-Dimensional TLM Modelling

Three-dimensional TLM theory is essentially the same as the two-dimensional theory. The node that was used for all the programs was the symmetrical condensed node described by Johns (1987). Figure 6.3 shows the symmetrical condensed node without stubs, with the notation that will be used for the rest of this chapter. The node basically consists of two transmission lines in each direction (x, y and z), so that the polarisations in any direction of propagation do not couple with each other.

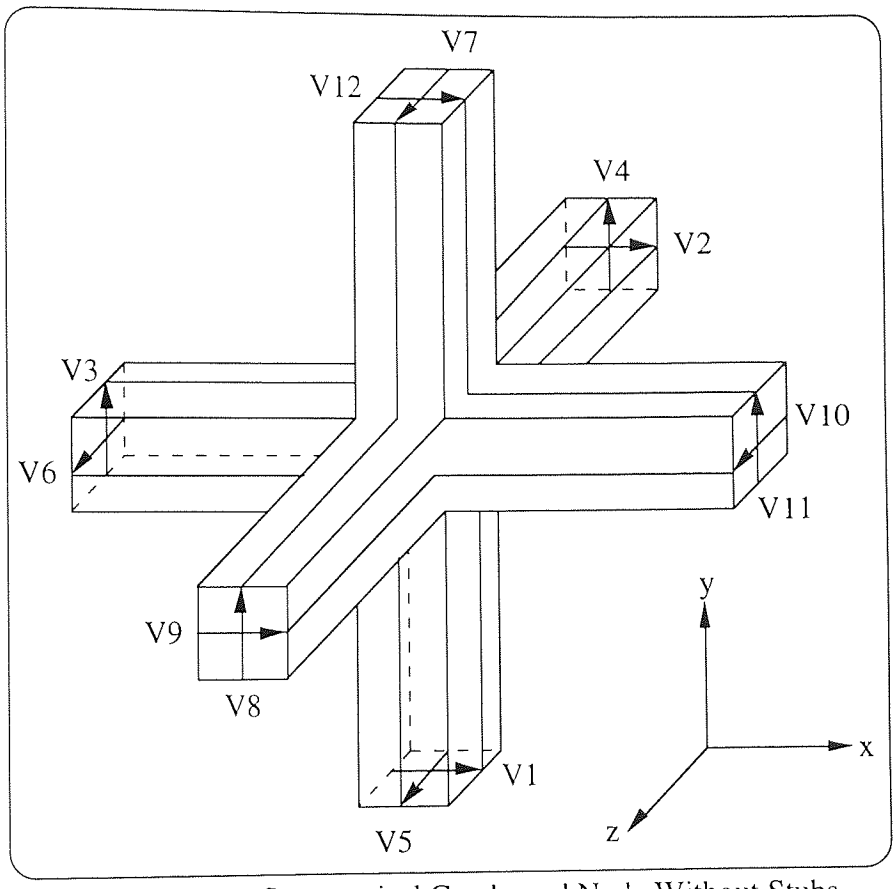

Figure 6.3: The Symmetrical Condensed Node Without Stubs

As with the two-dimensional node it is possible to model losses in materials by the inclusion of stubs on the node. A total of six stubs are needed (numbered V13 to V18) to couple with both the electric and magnetic fields in x, y and z directions. The electric field stubs (V13 to V15) are open circuit and add capacitance to the node, whereas the magnetic stubs (V16 to V18) are closed circuit and add inductance to the node. So the scattering matrix becomes:

$$
s = \begin{bmatrix}
a & b & d & & & & & b & & -d & c & g & & & & & i \\
b & a & & & & d & & & c & -d & & b & g & & & -i & \\
d & & a & b & & & & b & & & c & -d & & g & & & -i \\
 & & b & a & d & & -d & c & & & b & & & g & & i & \\
 & & & d & a & b & c & -d & & b & & & & & g & -i & \\
 & d & & & b & a & b & & -d & c & & & & & g & & i \\
 & & & -d & c & b & a & d & & b & & & & & g & i & \\
 & & b & c & -d & & d & a & & & b & & & g & & -i & \\
b & c & & & & -d & & & a & d & & b & g & & & & i \\
 & -d & & & b & c & d & & & d & a & & & & & g & & -i \\
-d & & & c & b & & & & b & & & a & d & & g & & & i \\
c & b & -d & & & & & & & b & & & d & a & g & & & -i \\
e & e & & & & & & & & e & & & & e & h & & & \\
 & & & e & e & & & & e & & & e & & & & h & & \\
 & & & & & e & e & e & & & e & & & & & h & & \\
 & & & & f & -f & & f & -f & & & & & & & & j & \\
 & & -f & & & & f & & & f & -f & & & & & & & j \\
f & & & -f & & & & & & & & f & -f & & & & & & j
\end{bmatrix}
\qquad \text{(eq6.4.1)}
$$

where:

$$
a = \frac{-Y}{2(4+Y)} + \frac{Z}{2(4+Z)} \qquad \text{(eq6.4.2)}
$$

$$
b = \frac{4}{2(4+Y)} \qquad \text{(eq6.4.3)}
$$

$$
c = \frac{-Y}{2(4+Y)} - \frac{Z}{2(4+Z)} \qquad \text{(eq6.4.4)}
$$

$$
d = \frac{4}{2(4+Z)} \qquad \text{(eq6.4.5)}
$$

$$
e = b \qquad \text{(eq6.4.6)}
$$

$$
f = Z\,d \qquad \text{(eq6.4.7)}
$$

$$
g = Y\,b \qquad \text{(eq6.4.8)}
$$

$$
h = \frac{(Y-4)}{(Y+4)} \qquad \text{(eq6.4.9)}
$$

$$
i = d \qquad \text{(eq6.4.10)}
$$

$$
j = \frac{(4-Z)}{(4+Z)} \qquad \text{(eq6.4.11)}
$$

$$Y = \frac{2\,\varepsilon_r}{c\,\Delta t}\,\Delta l - 4 \qquad \text{(eq6.4.12)}$$

$$Z = \frac{2\,\mu_r}{c\,\Delta t}\,\Delta l - 4 \qquad \text{(eq6.4.13)}$$

Where:

c - speed of light (299.86 x 10^6 m/s)

Δl - node size (m)

Δt - time step (s)

Y - normalised characteristic admittance

Z - normalised characteristic impedance

ε_o - permittivity of free space (8.885 x 10^{-12}F/m)

ε_r - relative permittivity

μ_o - permeability of free space (4π x 10^{-7}H/m)

μ_r - relative permeability

The electric (E) and magnetic (H) fields can be calculated by determining the total voltage in the relevant direction and then dividing this by the node size (Δl). This can be done in all three directions and the following equations, Christopoulos (1995), for electric and magnetic fields are found:

$$E_x = \frac{2\,(V^i_1 + V^i_2 + V^i_9 + V^i_{12} + Y_x\,V^i_{13})}{\Delta l\,(4 + Y_x)} \qquad \text{(eq6.4.14)}$$

$$E_y = \frac{2\,(V^i_3 + V^i_4 + V^i_8 + V^i_{11} + Y_y\,V^i_{14})}{\Delta l\,(4 + Y_y)} \qquad \text{(eq6.4.15)}$$

$$E_z = \frac{2\,(V^i_5 + V^i_6 + V^i_7 + V^i_{10} + Y_z\,V^i_{15})}{\Delta l\,(4 + Y_z)} \qquad \text{(eq6.4.16)}$$

$$H_x = \frac{2\,(V^i_4 - V^i_5 + V^i_7 - V^i_8 - V^i_{16})}{Z_o\,\Delta l\,(4 + Z_x)} \qquad \text{(eq6.4.17)}$$

$$H_y = \frac{2\,(-V^i_2 + V^i_6 + V^i_9 - V^i_{10} - V^i_{17})}{Z_o\,\Delta l\,(4 + Z_y)} \qquad \text{(eq6.4.18)}$$

$$H_z = \frac{2\,(V^i_1 - V^i_3 + V^i_{11} - V^i_{12} - V^i_{18})}{Z_o\,\Delta l\,(4 + Z_z)} \qquad \text{(eq6.4.19)}$$

Where the units of V are dependent on whether currents or voltages are used for the sources. The above equations for the field values assume that the units are volts. If currents are used then all the field values need to be multiplied by the impedance of free space ($Z_o = 377\Omega$) to give the correct values.

As with finite element analysis TLM modelling also needs boundaries to limit the physical size of the problem so that it becomes computationally manageable. There were two types of boundaries that were used in the TLM modelling of the drive these being perfectly reflecting boundaries and absorbing boundaries.

Perfectly reflecting boundaries consist of electric and magnetic walls, that is walls with zero or infinite impedance. To model these boundaries the pulses are returned to the node of origin with equal sign (magnetic wall) or opposite sign (electric wall), if the pulses simulates an electric field. If the pulses represent a magnetic field then the pulses are returned to the node of origin with equal sign (electric wall) or opposite sign (magnetic wall).

Absorbing boundaries are modelled by a wall of intrinsic impedance equal to the mesh, that is the reflection coefficient, r, becomes:

$$r = \frac{\frac{Z_o}{\sqrt{2}} - Z_o}{\frac{Z_o}{\sqrt{2}} + Z_o} = \frac{1 - \sqrt{2}}{1 + \sqrt{2}} = -0.1716 \qquad \text{(eq6.4.20)}$$

All the boundaries are placed halfway between two nodes so that the synchronisation of the mesh is preserved.

6.5 Wire Modelling Techniques

There are three methods that can be used:

1. A constant fine mesh over the whole problem area, where the node size is the same size or smaller than the diameter of the wire.
2. A graded mesh as describe by Al-Mukhtar *et al* (1981), as shown in Figure 6.4
3. A multi-grided mesh as described by Herring & Christopoulos (1994), as shown in Figure 6.4
4. A wire node which allows wires to be modelled in mesh where Δl is greater than the wire diameter as described by Naylor & Christopoulos (1990).

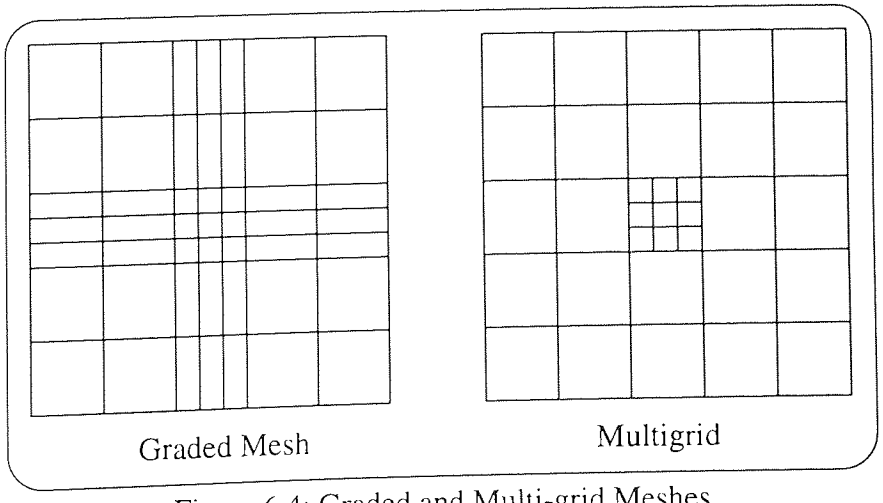

Figure 6.4: Graded and Multi-grid Meshes

Each method has its advantages and disadvantages. A constant mesh is the simplest to use, but it has the disadvantage that the smallest detail (eg the wire diameter) in the problem dictates the node size, and this ultimately prevents this method from being used for very large problems. The use of a graded mesh overcomes the problem of being able to define small detail and still solve relatively large problems, but it has the disadvantage that one area of detail will affect a large proportion of the coarse mesh. Obviously the more areas of fine detail there are the less coarse the coarse mesh will be. The multi-grid method, although being the hardest to implement, solves the disadvantages of the first two methods, by including a fine mesh within the coarse mesh, and the only interactions between the two meshes is when the pulses are transferred between the fine and coarse meshes. The wire node, solves the problem by applying a coarse mesh over the whole problem, and using special nodes to describe the wire which allow the mesh size to be greater than the wire diameter.

The multi-grid method and the wire nodes were both implemented in the three-dimensional TLM model, and the theory for these methods can be seen in the following two sections. A two-dimensional model using the graded mesh technique was written using MATLAB and this can seen in appendix A7.1. The theory for this method can be seen in appendix A6.

6.5.1 Multi-Grid Implementation

The main problems with the implementation of the multi-grid method is the transference of the pulses between the different sized grids, and also the synchronisation of the pulses throughout the mesh.

The second problem is the easiest one to solve as it is a function of the ratio of the meshes. For example Figure 6.5 shows a mesh where the coarse mesh is twice the size of the fine mesh, so for every single pulse on the coarse mesh there must be eight fine pulses.

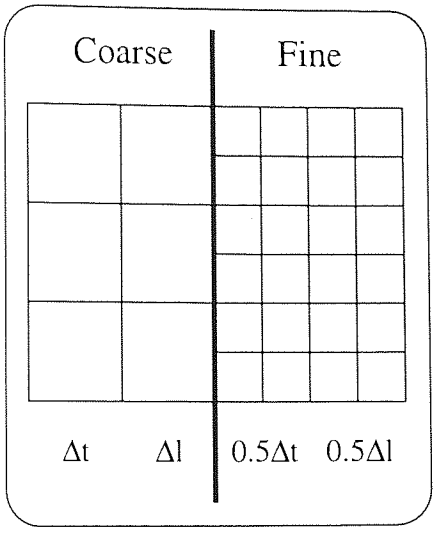

Figure 6.5: Comparison of Fine and Coarse Meshes

The rest of the work concerning the implementation of the multi-grid method will be done assuming that the fine mesh is half the size of the coarse mesh, i.e. a 2:1 reduction.

The major problem as was stated at the beginning of this section is the transference of the pulses between the meshes whilst still retaining the accuracy of the method. As Herring & Christopoulos (1994) stated this accuracy can be ensured by the implementation of a number of interface conditions:

1. Charge conservation.
2. Energy Conservation.
3. No Reflection, i.e. the interface is transparent to the adjacent nodes.
4. Zero time delay.

To fulfil the first constraint (charge conservation) the charge on the boundary of the fine mesh has got to equal the charge on the boundary of the coarse mesh. This is the same as ensuring the continuity of the field across the boundary, i.e. the field leaving the coarse mesh must be the same as the field entering the coarse mesh. Continuing on from this it can be deduced that the charge conservation across the boundary is the same as saying:

$$\frac{1}{p_c t_c} \sum_{j=1}^{n_j} V_{c_j} = \frac{1}{p_f t_f} \sum_{k=1}^{n_k} V_{f_k} \qquad \text{(eq6.5.1)}$$

Where:

n_i - number of pulses in each direction

p_i - the number of lines across the direction of polarisation

s_i - the number of lines along the direction of polarisation

t_i - the number of time steps before conversion

subscripts:

c - coarse mesh

f - fine mesh

j - number of pulses of the coarse mesh before conversion

k - number of pulses of the fine mesh before conversion

The number of pulses before conversion, n_i, can be calculated from $n_i=p_i t_i$ for two dimensional meshes, and $n_i=s_i p_i t_i$ for three dimensional meshes. Where the value t_i represents the the number of time steps before conversion.

The second constraint (energy conservation) means that the energy of the pulses leaving the fine mesh is related to the energy of the pulses leaving the coarse mesh by a constant α. The constraint of energy conservation is enforced when:

$$\sum_{j=1}^{n_j} V^2_{c_j} = \alpha \sum_{k=1}^{n_k} V^2_{f_k} \qquad \text{(eq6.5.2)}$$

The constant α is determined by solving of equations 6.51 and 6.52.

The third constraint (no reflections) is achieved by running the coarse to fine and the fine to coarse conversion procedures separately. This means that when a pulse is converted from the coarse mesh to the fine mesh, the only reflections will be due to the scattering at the nodes in the fine mesh, the same thing will happen when a pulse is

converted from the fine mesh to the coarse mesh except that the scattering will occur in the coarse mesh. If both pulses were converted at the same time then the coarse to fine conversion will depend on the value of the pulse leaving the fine mesh and visa versa.

The fourth constraint (zero delay) is related to the program structure and the order in which the calculations are carried out, for example in the 2:1 reduction ratio the calculations would be done in the following order:

1. Calculation of the pulses on the fine mesh.
2. Transferal of the pulses on the fine mesh to the coarse mesh.
3. Calculation of the pulses on the fine mesh.
4. Calculation of the pulses on the coarse mesh.
5. Transferal of the pulses on the coarse mesh to the fine mesh.

There are a number of different ways in which the pulses can be converted between the different meshes, and these can be seen in Herring (1993) and Herring & Christopoulos (1994). The method that was implemented was where the constraint of energy conservation is ignored, the reason that this can be done is that in practice this will only start to produce errors in the solution at frequencies above the cut off frequency, ie:

$$f_{\text{cut off}} = \frac{(\mu_o \varepsilon_o)^{-0.5}}{4\,\Delta l} \qquad \text{(eq6.5.3)}$$

In reality this method ensures that the average value of electric field due to a set of pulses incident upon the coarse/fine mesh boundary is the same as when the new pulses are transferred onto the other side of the boundary. The conversion process that was used was as follows:

Coarse to Fine.

$$V_{c_j} = \frac{1}{s_c\, Pf\, t_f} \sum_{k=1}^{n_f} V_{f_k}, \text{ for } j=1, 2, \ldots n_c \qquad \text{(eq6.5.4)}$$

Fine to Coarse.

$$V_{f_j} = \frac{1}{s_f P_c t_c} \sum_{k=1}^{n_c} V_{c_k}, \text{ for } j=1, 2, \ldots n_f \qquad \text{(eq6.5.5)}$$

With the 2:1 reduction ratio Table 6.1 shows the constants for the coarse and fine meshes and eq6.5.6 and 6.5.7 show the equations used for transferring the pulses between the meshes.

Parameter \ Mesh	Coarse	Fine
s	1	2
p	1	2
t	1	2
n = s p t	1	8

Table 6.1: Parameters for the 2:1 Reduction

Coarse to Fine:

$$V_{f_j} = \frac{1}{2} V_c, \text{ for } j=1, 2, \ldots 8 \qquad \text{(eq6.5.6)}$$

Fine to Coarse:

$$V_c = \frac{1}{4} \sum_{k=1}^{8} V_{f_k} \qquad \text{(eq6.5.7)}$$

The calculation order that was used is the same as the one described previously.

6.5.2 Wire Node Implementation

The wire node is a special node that models a wire passing through the node in the x, y or z-direction. The wire node also allows the node size to be greater than the wire

radius, hence it is possible to model thin wires using a relatively coarse mesh. Figure 6.6 shows the wire node with the wire in the z-direction.

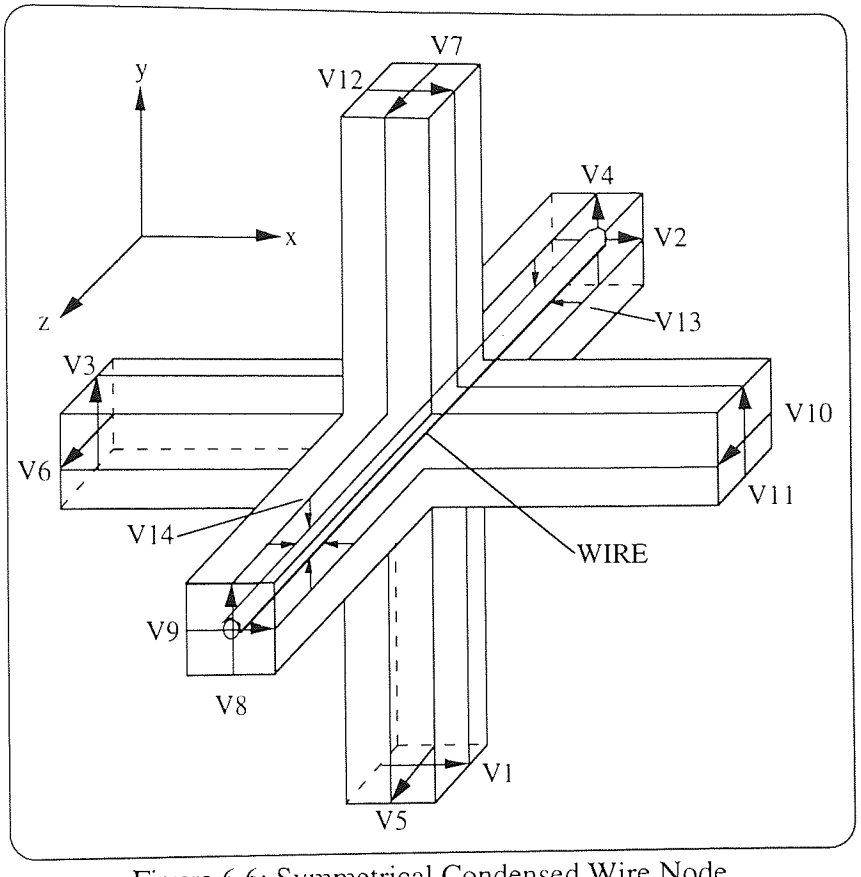

Figure 6.6: Symmetrical Condensed Wire Node

The wire node scatters the pulses in the same way as the symmetrical condensed node, the only difference being that it has two extra stubs (V13 and V14) to model the wire-like properties within the node. As with the symmetrical condensed node it is possible to represent the scattering within the node as a matrix (s_{wire}), and the matrix for the z-direction can be seen in equation 6.5.8. There are corresponding matrices for the x and y-directions.

$$
{}^{s}wire_{z} = \begin{bmatrix}
 & 0.5 & 0.5 & & & & & 0.5 & & -0.5 & & & \\
0.5 & & & & & 0.5 & & & -0.5 & & 0.5 & & \\
0.5 & & & 0.5 & & & 0.5 & & & & -0.5 & & \\
 & & 0.5 & & 0.5 & & -0.5 & & & 0.5 & & & \\
 & & & 0.5 & -a & b & -a & -0.5 & & b & & Yb & Yb \\
 & 0.5 & & & b & -a & b & & -0.5 & -a & & Yb & Yb \\
 & & & -0.5 & -a & b & -a & 0.5 & & b & & Yb & Yb \\
 & & 0.5 & & -0.5 & & 0.5 & & & & 0.5 & & \\
0.5 & & & & & -0.5 & & & & 0.5 & & 0.5 & \\
 & -0.5 & & & b & -a & b & & 0.5 & -a & & Yb & Yb \\
-0.5 & & & 0.5 & & & & 0.5 & & & & 0.5 & \\
 & 0.5 & -0.5 & & & & & & 0.5 & & 0.5 & & \\
 & & & & b & b & b & & & b & & Yb & -2b \\
 & & & & b & b & b & & & b & & -2b & Yb
\end{bmatrix}
\qquad \text{(eq6.5.8)}
$$

$$
Y = \frac{2\, Z_o \sqrt{\varepsilon_r}}{60 \ln\left(\frac{0.54\, \Delta l}{r}\right)} \qquad \text{(eq6.5.9)}
$$

$$
a = \frac{Y}{2\,(Y+2)} \qquad \text{(eq6.5.10)}
$$

$$
b = \frac{1}{Y+2} \qquad \text{(eq6.5.11)}
$$

Where:

ΔL - node size (m)

r - wire radius (m)

Y - normalised admittance of the wire

Z_o - wave impedance (377Ω)

ε_r - relative permittivity of the wire

6.5.3 Comparison of the Wire Node to the Multi-Grid Method

When the wire node and the multi-grid methods are compared it becomes apparent that each of the methods had different strengths and weaknesses, and if both both methods were implemented the final program would be computationally inefficient, and more complicated than was actually needed. Table 6.2 summarises how the two methods compare.

Multi-Grid Method	Wire Node Method
Easy to model fine detail and wires.	Can only model wires, but $\Delta l >> r$.
Requires two meshes, one coarse and one fine, hence more calculations per iteration, hence more memory.	Requires only one mesh, hence less memory.
Need to apply boundary conditions around the nodes that form the wire.	No extra calculations needed to model the wire.
Run times are higher, because the fine mesh requires more calculations.	Run times are shorter because there is only one coarse mesh.
Computationally difficult to program.	Computationally easier to program.
Highly inefficient.	More efficient than the multi-grid.

Table 6.2: Comparison of the Wire Node and Multi-Grid Methods

It can be seen from Table 6.2 that the wire node method is computationally more efficient than the multi-grid method. The only drawback of the wire node method being that it is confined to the modelling of wires, whereas the multi-grid method can model both wires and fine detail.

It was decided to implement the wire node method in the three-dimensional TLM model as this appeared to be the computationally more efficient of the two methods, and it was also considered possible to totally model the areas of interest in the 583 drive using only wires.

6.6 Program Structure

A TLM program was written to model the 583 drive using the techniques outlined in the previous sections. The program used the three-dimensional symmetrically condensed node with stubs. The program had the following features:

1. The ability to model inhomogeneous media.
2. The ability to model boundaries as either perfectly reflecting or absorbing.
3. The ability to model thin wires using a special wire node.
4. User defined number of input/output points.

A flow chart showing the calculation procedure used in the program can be seen in Figure 6.7. The program listing for the three-dimensional model produced using the TLM method can be seen in appendix A7.2.

The program was written using MATLAB 4.0 and also C++. The maximum mesh size that the model could support was 40 nodes x 40 nodes x 40 nodes, and a mesh this size took approximately 1300 seconds to perform a single iteration when written using MATLAB, but only 11 seconds when using C++. This time can be reduced by removing the stubs from the node, which results in a 20% reduction in the time for a single iteration.

The remainder of the TLM models were written using C++ as it was significantly quicker than MATLAB 4.0.

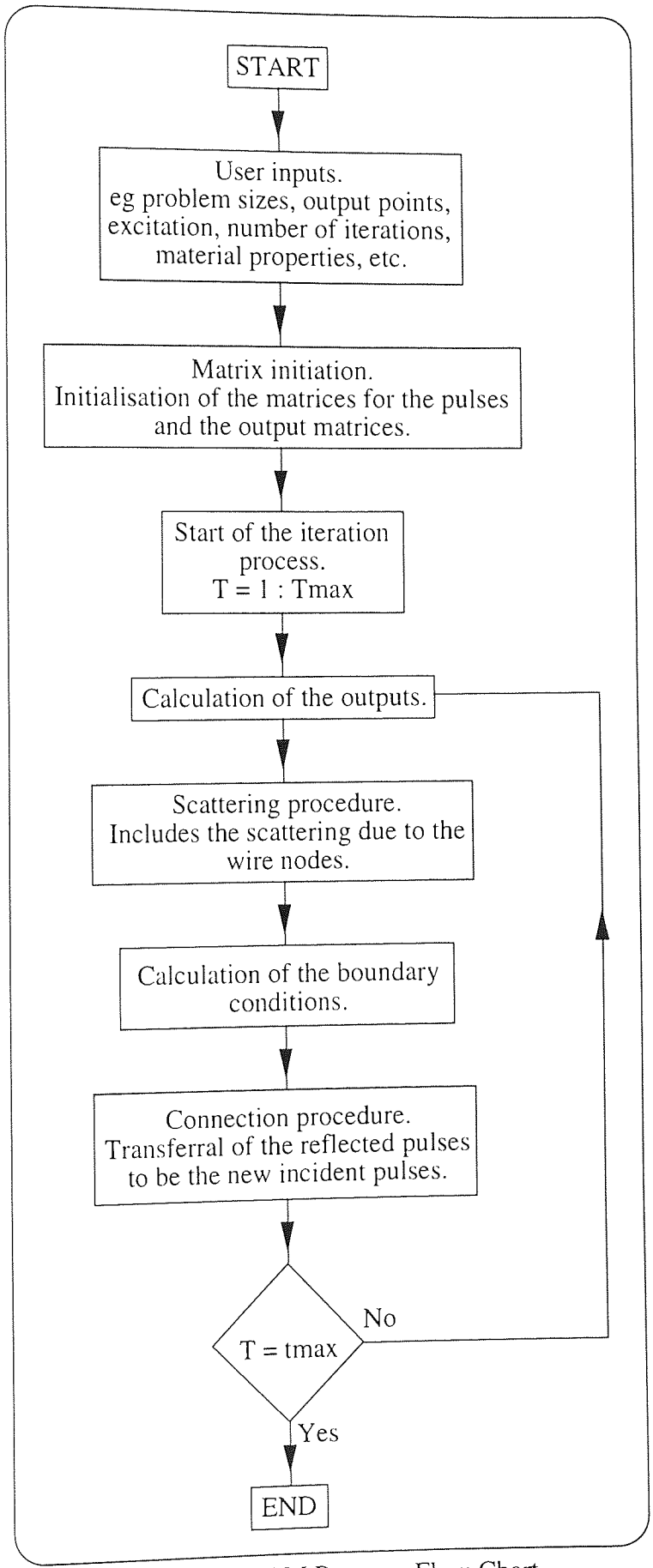

Figure 6.7: TLM Program Flow Chart

6.7 TLM Model Structure of the 583 Drive

As the TLM model that had been previously written used three-dimensional theory, it meant that the model of the drive could be far more realistic than the finite element model was in two-dimensions. In theory it was feasible to completely model the 583 drive and the test rig used to measure the radiation in three-dimensions. However it was not a viable solution due to the vast amount of computer memory required and the time to generate the model. So like the finite element model the TLM model only took account of the areas of the drive that were likely to produce the radiation, as well as only modelling a limited section of the test rig. The finite element model had previously identified the major radiation source in the drive to be the shielded cable, which connected the drive to the motor. It was decided that this would be the only area included in the TLM model.

Before the model could be generated the node size (Δl) had to be determined. The node size had to be small enough to model the features of the drive, and it also had to be as large as possible to minimise the physical size of the problem. A number of node sizes were considered, and these can be seen along with the corresponding cut off frequencies and time steps in Table 6.3. The cut-off frequencies were determined using equation 6.5.3 and the time steps using equation 6.3.1. The cut-off frequency needs to be above the highest frequency of interest (200MHz) to prevent errors from being introduced into the model. As can be seen from Table 6.3 when the node size extends above 0.3m the cut-off frequency drops below 200MHz, so the node size has to be either equal to or less than 0.3m. When the node size drops below 0.3m the number of nodes required to model the problem increases rapidly, and this increase is also reflected in the simulation times. So the node size for the modelling of the drive was set at 0.3m, which gave a cut-off frequency of 250MHz and a time step of size 0.707ns.

Δl (m)	$f_{cut\ off}$ (MHz)	Δt (ns)	No.of nodes per m^3
0.05	1500	0.118	8000
0.1	750	0.236	1000
0.25	300	0.589	64
0.3	250	0.707	37
0.5	150	1.179	8
1.0	75	2.357	1

Table 6.3: Node Sizes and Cut-Off Frequencies

To make the model as simple as possible the shielded cable was modelled as a single cable contained within the steel shield, whereas in reality there were three signal cables and one ground cable contained within the shield. The shield on the cable was modelled using boundary conditions to cause the pulses incident upon the shield to be reflected away, the boundary condition being that of a perfectly reflecting wall. As the cable was coiled during the measurement procedure, the model took account of this by modelling the cable as a combination of seventeen 'wire' nodes in the x, y and z-directions which gave a total wire length of 5.1m with the wire radius being set at 0.001m, see Figure 6.8.

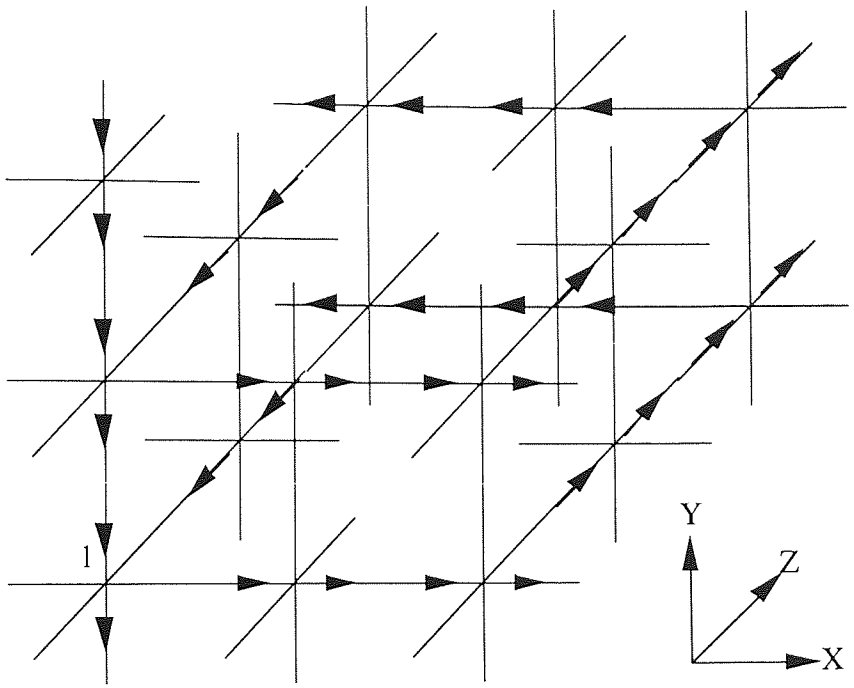

Reference Point (1)= 4, 2, 4

A: Arrangement of the Wire Nodes Used in the Cable Model

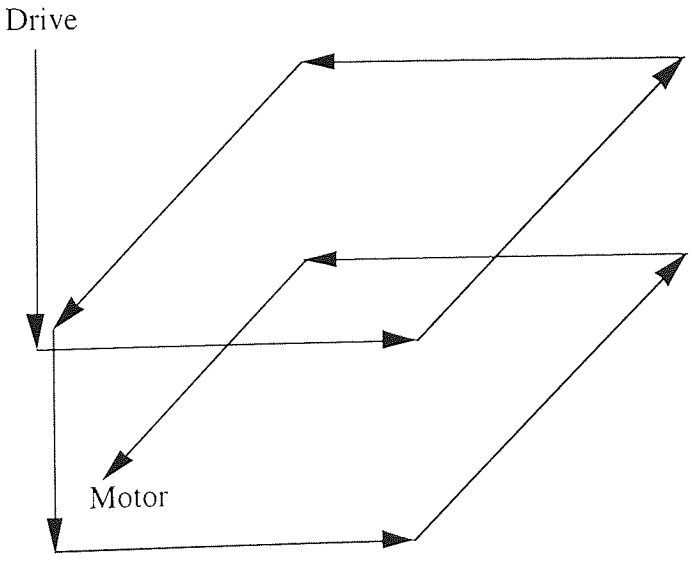

B: Physical Representation of the Cable Model

Figure 6.8: Shielded Cable Model Used in the TLM Model

The boundary conditions applied to the TLM model consisted of two types, the first type being perfectly reflecting boundaries which were used to model the shield on the shielded cable and the ground plane on which all the measurements were made. The

other boundaries were modelled using an absorbing boundary condition, the reason for this being that these boundaries were in fact infinite boundaries and hence all of the field will travel off into infinity.

Like the finite element model, the electric field was measured at a distance of 3m from the drive rather than the 10m used during the measurements. This was then converted into the 10m distance used during the measurements by use of the following equation:

$$E_{10m}(dB) = E_{3m}(dB) - 10.46(dB) \qquad \text{(eq6.7.1)}$$

A distance of 0.9m (three nodes) was placed between the measurement point and the boundaries to prevent the boundary conditions having an effect on the results. Ideally a much greater distance (ie 10m which is equivalent to 33 nodes) should be used, but due to limitations on computer space and time the model had to be made as small as possible. As was previously said the point where the field was measured was at a distance of 3m from the shielded cable model. The output was measured at a height of 0.9m above the ground plane, and the cable model was set at a height of 0.3m above the ground plane. This produced a model of size 17 x 7 x 9 nodes (5.1 x 2.1 x 2.7 m), see Figure 6.9, which took approximately a third of a second for a single time step.

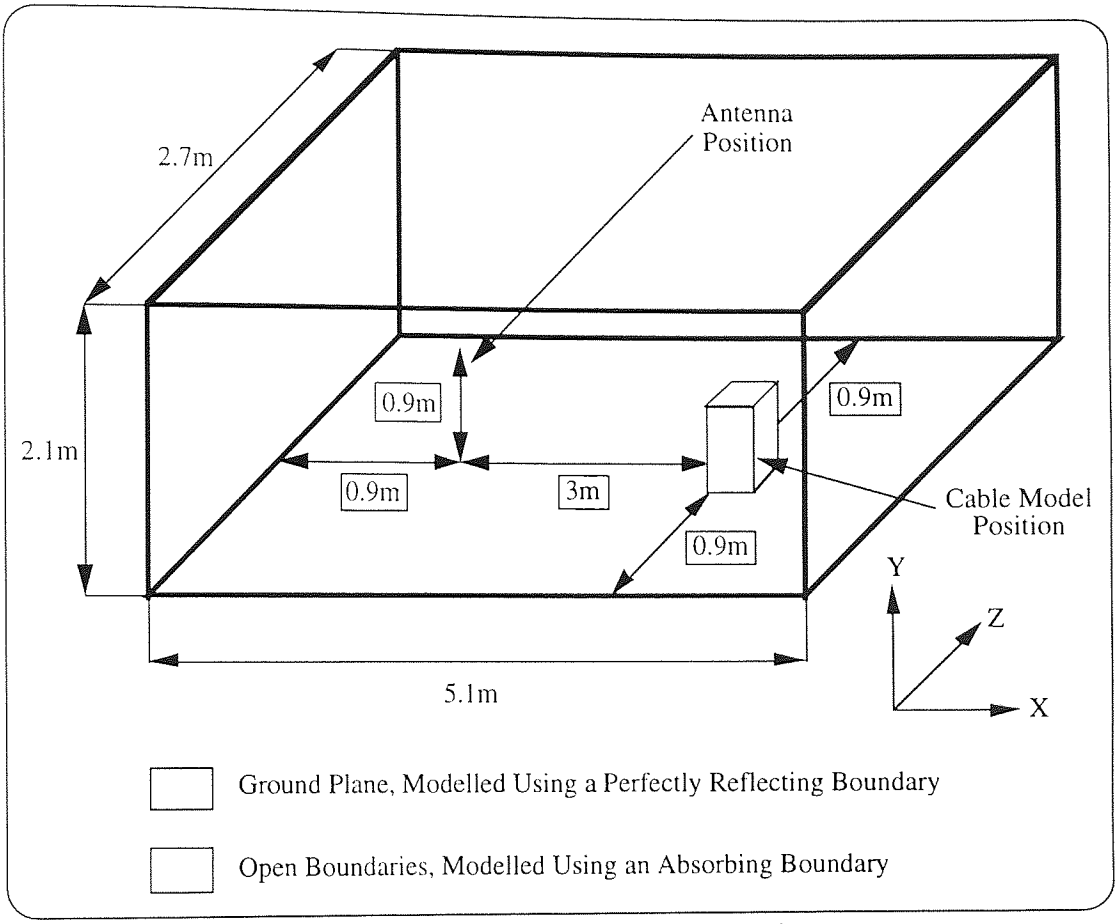

Figure 6.9: TLM Model of the 583 Drive

As with the finite element model the TLM model was excited with the current sources generated using the SABER model (see chapter 3). The only source used in the TLM model was that of the shielded cable, which consisted of the differences of the three currents flowing in the shielded cable, see Figure 6.10. The common mode currents which were flowing in the shield of the shielded cable cable could not be applied to the model because the large amount of time steps that the model would take meant that the same amount of points from the common mode waveform would also be required. As it was not a viable solution to write all the points in by hand and it was also not possible to write an equation to generate the values, the common mode currents could not be applied to the model. If the SABER model had produced a file with all the points for the waveform contained in it, it would have been possible to read the values in from the file and excite the model with them.

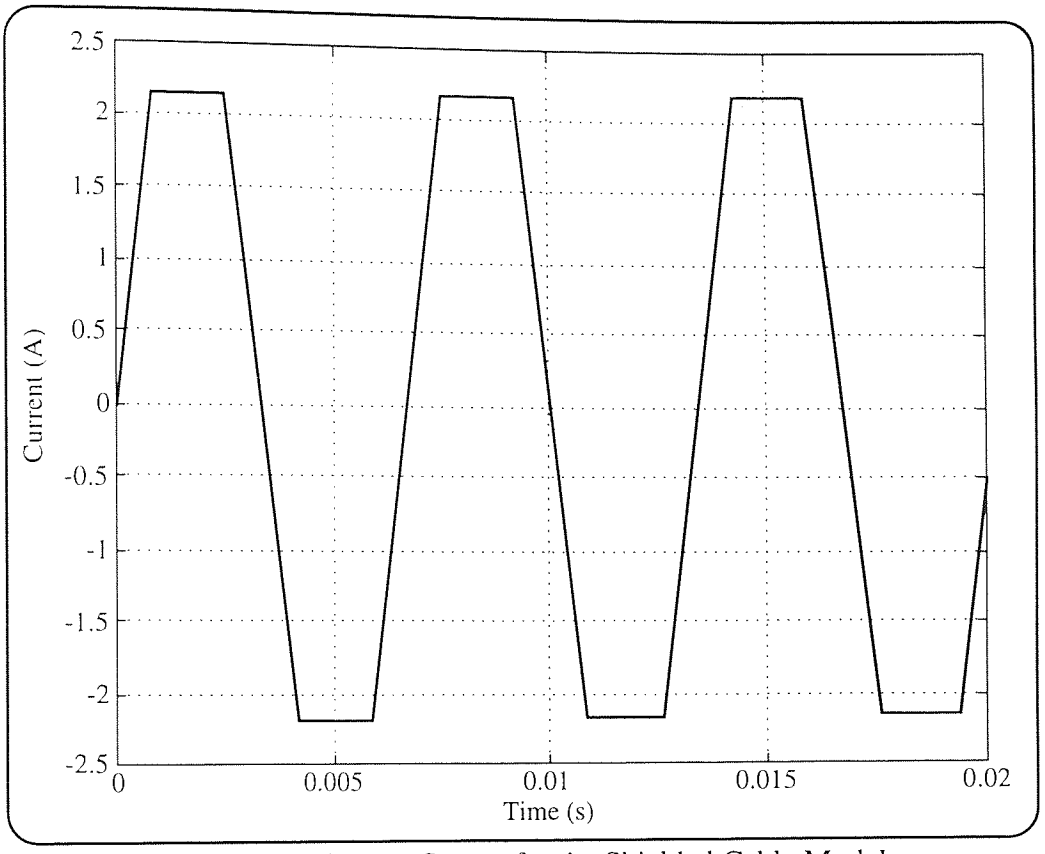

Figure 6.10: Current Source for the Shielded Cable Model

From Figure 6.10 it can be seen that the model needs to be run for a total time of 6.66ms, ie one complete cycle of the source waveform. The reason for this is so that the results obtained from the model cover a complete cycle of the source, if a complete cycle is obtained it is then possible to perform a Fourier transform on the results to obtain them in the frequency base. This time actually corresponds to 9.42 million iterations

6.8 Model Results

As it was not feasible to apply the common mode currents that were present in the shielded cable to the TLM model (see previous section for reasons), the TLM model was excited with the current that the motor would see (Figure 6.10). An identical set of simulations were also run using the previously generated finite element model, to allow a comparison between the two methods to be made.

The TLM model was run for a total time of 5ms (7.1 million time steps), and the output from the model was the electric fields in the x, y and z-directions. Figure 6.11 shows the outputs, measured at a distance of 3m and at a height of 0.9m from the cable, from the model in the first 106ns (150 time steps). It can be seen that the model takes approximately 100ns (141 time steps) to settle into steady state conditions. It also shows the small delay (8.485ns in the x-direction, 9.192ns in the y-direction and 7.778ns in the z-direction) before the electromagnetic wave generated by the wire model reaches the output point in the model.

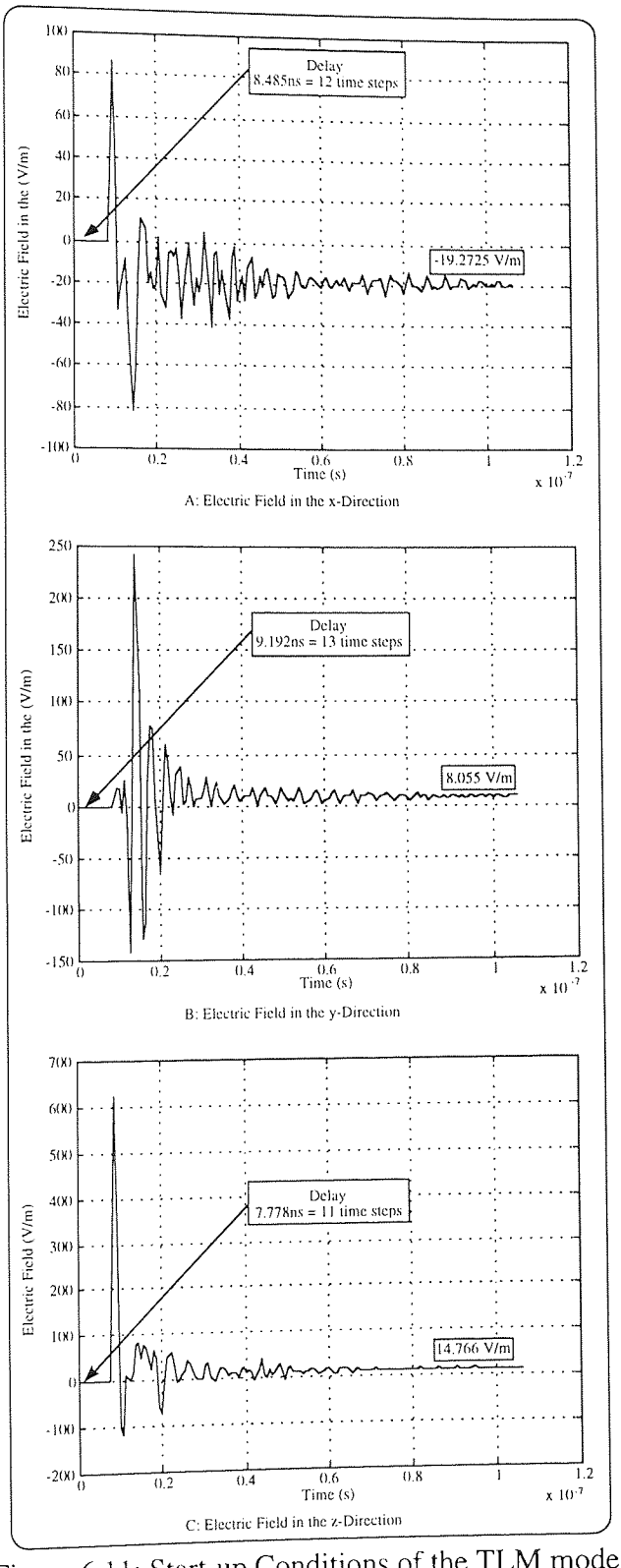

Figure 6.11: Start-up Conditions of the TLM model

Figure 6.12 shows the output from the TLM model in the x, y and z-directions.

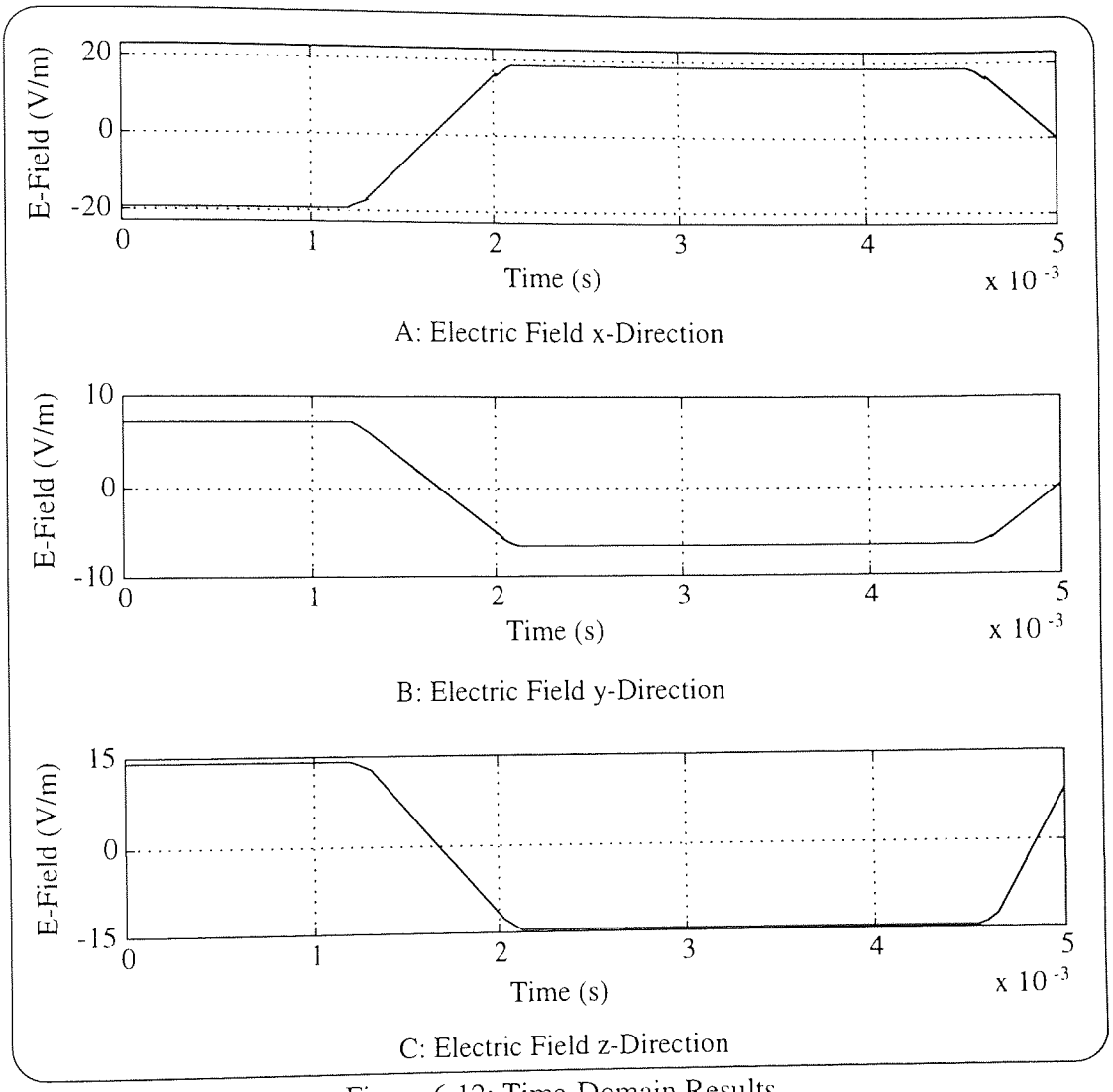

Figure 6.12: Time-Domain Results

Figure 6.13 shows the comparison between the TLM model and the finite element model, where the values plotted are the modulus of the results.

For the three-dimensional TLM model the modulus is equal to:

$$E_{mod} = \sqrt{E^2_x + E^2_y + E^2_z} \qquad \text{(eq6.8.1)}$$

For the two-dimensional finite element model the modulus is equal to:

$$E_{mod} = \sqrt{E^2_x + E^2_y} \qquad \text{(eq6.8.2)}$$

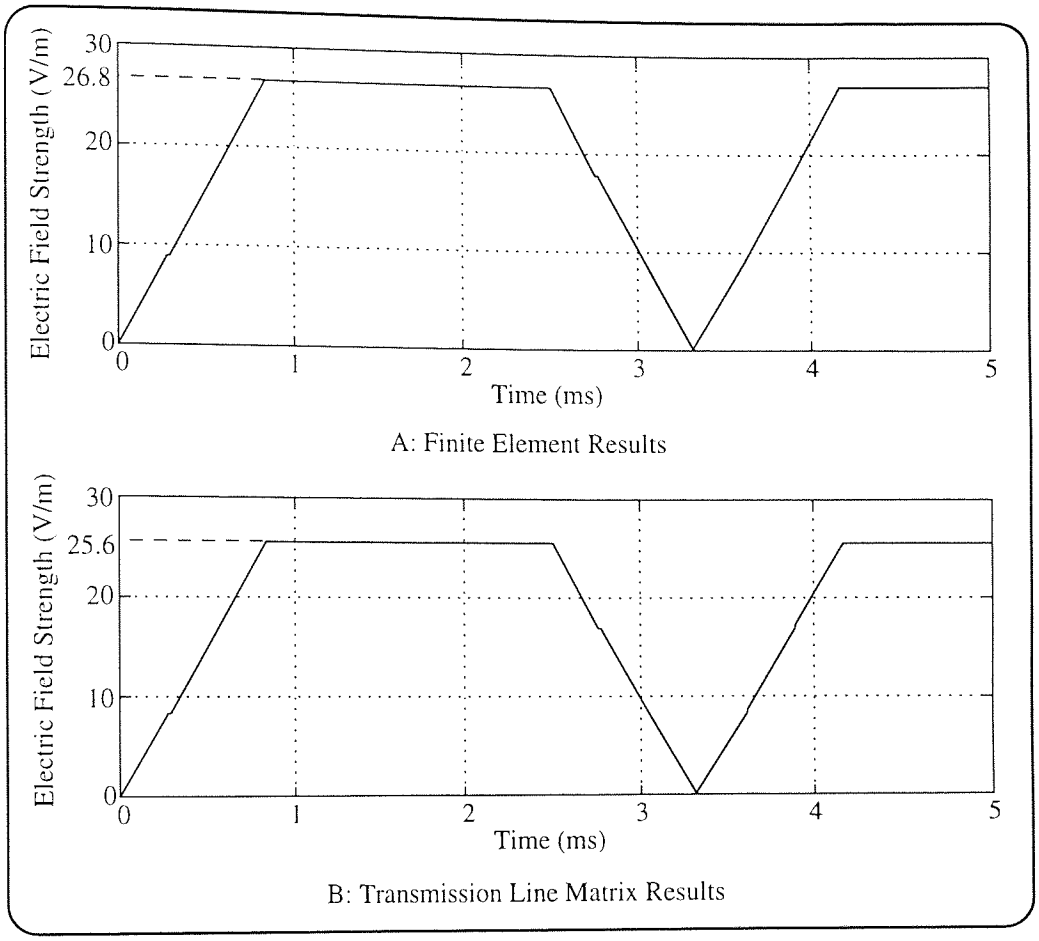

Figure 6.13: Comparison of the TLM and FEA Results

As can be seen from Figure 6.13 the results obtained from both of the methods are very similar. The similarity between the methods is very surprising as the finite element model only took into account two field directions, whereas the TLM method took into account all three directions. The peak values of the plots are within 1.3 V/m of each other and this corresponds to an error of 5%. This shows that the TLM method is capable of producing results that are comparable to results produced using a two-dimensional finite element model. Even though the TLM method is capable of producing comparable results to the finite element method, it was still deemed to be a poor solution to the problem. The reason for this being the size of the time steps (for the problem in question t_{step} = 0.707ns) the method uses, as the time steps are so small it therefore means that a large number of time steps need to be taken to run a problem for the desired length of time. Using the TLM method the above problem took approximately one month to produce a solution. Whereas the two-dimensional finite element method can produce the answer in approximately a day.

6.9 Problems With Three-Dimensional TLM Modelling

A number of problems with TLM modelling were identified, during the modelling and simulation of the 583 drive. The first of these problems was that the method is very slow when large time spans (ie above 5μs) need to simulated. The reason for this is the small time steps used in the TLM method which are dependent on the node size used (the smaller the node size the smaller the time step size). As each time step for a problem of size 17 x 7 x 9 nodes takes approximately 0.1s, this means that if the problem was required to be run for 10ms it would take 16.4 days of computer time to produce a solution if a node size of 0.3m was used. These figures are based on a 100MHz machine. Obviously these times could be reduced if a faster machine was used. This causes problems as it is not possible to use very large node sizes which would result in large time steps as this would prevent the modelling of any small detail that was present in the problem. This means that the TLM is not really suitable for predicting radiation profiles from equipment which operates on low frequencies (ie below 0.5MHz), however for equipment which operate at higher frequencies the TLM method is an ideal solution as the number of time steps will be less so the time to run the simulation will also be less.

The second problem with the method was that of the modelling of fine detail without producing very large problems. If the fine detail to be modelled is a wire this does not cause too many problems as the wire node described by Naylor & Christopoulos (1990) can be used to model a wire in a mesh where the node size is much greater than the wire diameter. However much of the fine detail which may need to be modelled will concern areas were there are abrupt changes of geometry which cause rapid changes in the fields around the area of the change in the geometry. It is possible to use a fine mesh over a whole problem, but this will result in a problem which is computationally large and hence takes a long time to produce a solution. The alternative is to apply the multi-grid technique to the problem, which means that the area where the fields are changing rapidly is modelled using a fine mesh and the rest of the problem is modelled using a coarse mesh. This method is not an ideal solution though as the areas of fine mesh will need more time steps than the areas of coarse mesh to keep the continuity of the

propagation of the fields correct.

The final point concerns the suitability of the TLM method as a tool for the prediction of the radiated emissions from variable speed drives. As can be seen from the the work presented in this chapter the TLM method is not ideally suited to predict radiated emissions, because it is slow and it is also fairly difficult to apply unusual sources (ie waveforms that cannot be described with an equation) to excite the model. However from the work that has been done using the TLM method it has become apparent that the method could be used in EMC modelling. As was said in chapter 2 the EMC legislations are not only concerned with emissions but also with the immunity of products to external sources of electromagnetic radiation. One of the tests that has to be performed is that of radiated immunity where the product under test is subjected to an electric field of strength 10V/m over the frequency range 27MHz to 500MHz. The way in which the TLM method could be used to simulate this test is to excite the model with a sine wave of peak value 10V/m at the relevant frequencies. It would then be possible to determine the effect that the field would have on the operation of the drive by applying the voltage waveform generated using the TLM model to the SABER model.

6.10 Summary

This chapter presented the transmission line matrix method as a means of predicting the electromagnetic radiation from the 583 drive. The first part of the chapter presented the theory for both two-dimensional and three-dimensional transmission line matrix models. A three-dimensional model of the 583 drive was developed and written using C++. The model of the drive took into account the shielded cable which connected the drive to the motor as the finite element models in the previous chapter showed that this was the major source of the radiation from the drive. As the time steps used by the transmission line matrix model were small (0.707ns) it was not feasible to excite the model with the common mode currents which were flowing in the shield as the waveform could not be described with an equation like the differential mode current (which took the form of a trapezoidal waveform, and could be described using a Fourier series) which was flowing in the cable. As it was not possible to excite the

cable model with the common mode currents it was not possible to predict the radiation from the drive with the transmission line matrix model. The results obtained from the transmission line matrix model were confirmed as being comparable to the finite element method by running an identical problem using the two-dimensional finite element model that was previously developed. It was found that the results obtained from the the methods were comparable to within 5%, suggesting that the transmission line matrix method was capable of producing results which were comparable to the two-dimensional finite element method. It was also explained that the TLM method is not an ideal method for predicting the radiation profiles from variable speed drives because of the large amount of time steps, and hence the large amount of time required to solve the problem. Finally it was proposed that the TLM method would be suitable to predict the immunity of a drive to an externally applied electromagnetic radiation (ie immunity modelling).

Chapter 7

Discussion and Conclusions

7.1 Introduction

The discussion and conclusions for the work have been broken down into three distinct areas:

1. Conducted Emissions.
2. Measurement of the Radiated Emissions
3. Modelling of the Radiated Emissions.

The conclusions for all of these areas are presented in the following three sections, with a third section summarising the overall conclusions for the project.

7.2 Conducted Emissions

A model for predicting the conducted emissions and also the voltage and current sources for use in predicting the radiated emissions in variable speed drives has been presented (chapter 3). The model used takes the form of a circuit model of the various areas of the drive, the areas being:

1. The power electronics of the drive in question as the control electronics do not have a significant effect on the conducted emissions. The only part of the control electronics that was modelled was the signal which switches the IGBT's in the inverter. The IGBT's in the inverter were initially modelled as an accurate model of the IGBT's in the drive, but this was found to produce a slow model which was highly time consuming to set up, so an alternative was developed which consisted of a digitally controlled single-pole single-throw switch with a diode in series. This model was found to operate up to 30% faster than the initial IGBT model and was also significantly quicker to set up.

2. The shielded cable that was used to connect the drive to the motor during the experimental work. This was modelled as a network of resistors, capacitors and inductors which were calculated and also measured where possible to confirm the validity of the calculated values.

3. The motor that was used during the experimental work was modelled as a simple network of resistors, capacitors and inductors whose values were measured from the motor. The motor model assumed that the the motor had a near zero load as the motor had been allowed to run freely during all the experimental work.

4.The Line Impedance Stabilising Network (LISN) that was used to measure the conducted emissions was modelled so that the values obtained for the conducted emissions from the model would be comparable to the experimental values.

5. The parasitic capacitances that were present in the system were modelled as they are a major source of the common mode currents which are coupled through them to the ground plane. The parasitic capacitances were measured from the drive as no way of accurately calculating them could be found.

The model that was developed to predict the conducted emissions was found to accurately predict the emissions in the frequency range 150kHz to 16MHz, see Figure 7.1, which coincides well with the conducted emission legislations which is in the frequency range 150kHz to 30MHz. As can be seen from Figure 7.1 the modelled data follows the experimental data very closely. The decay of both of the plots is approximately -20dB/decade. This decay starts to occur at approximately 3.33MHz and this corresponds to the frequency of the rise time of the IGBT's (t_r=300ns). The prominent peaks which can be seen on the plots at 3MHz are due to the resonances of the inductances and capacitances on the shielded cable. The accuracy of the model was in the range +/- 6dBμV.

The advantage of this model is that it will allow a drive designer to determine whether a new design will comply with the EMC legislations, concerning conducted emissions, before a prototype is built, and this means that the designer can build the conducted emissions compliance into the design without having to build costly prototypes and then finding that they fail the EMC legislations. The second advantage of the model is that it can also be used to generate the voltage and current sources which are used in the model to predict the radiated emissions.

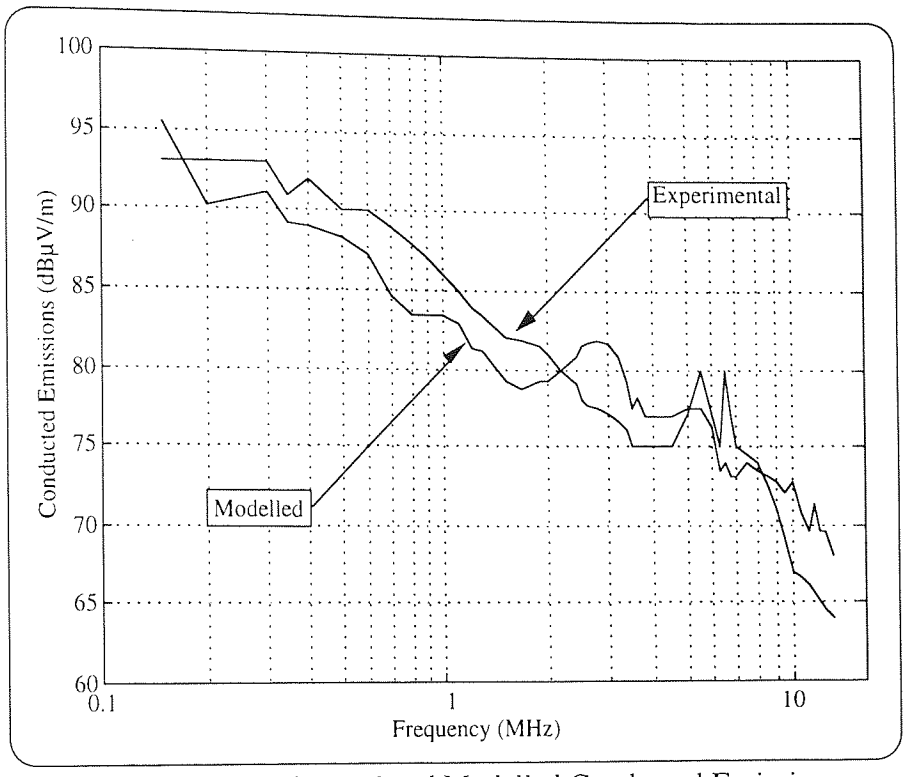

Figure 7.1: Experimental and Modelled Conducted Emissions

7.3 Measurement of the Radiated Emissions

A method used to measure the radiated emissions from variable speed drives has been presented (chapter 4). The measurements were made using an Open Area Test Site (OATS). The measurements were made with the antenna in the vertical and horizontal plane. It was found that the majority of the radiation was measured when the antenna was in the vertical plane. When the antenna was in the horizontal plane the reflections form the ground plane were having a nullifying effect on the measurements made.

As was said in chapter 4 there were a number of problems associated with the test rig used to make the radiated measurements and these are summarised below.

The first problem was with the repeatability of the results obtained from the rig. The only way to obtain any sort of repeatability from the rig is to attempt to always place the equipment under test in the same position, with the cables laid in the same path etc. Williams (1994) suggested that the repeatability of an open area test site is of the order of +/-10dB Even so it is not guaranteed that the results will be repeatable as the

background radiation may have a nullifying effect or magnifying effect at the time the measurements are made. Secondly the measurements are not made at the same time as the background readings, so it is not known what the background readings are at the time the measurements are made. The third problem was associated with the the rig's location. This was in a car park near to a factory, ideally it should have been located in the middle of a field several wavelengths away from any possible interference sources, but in practice this is generally not possible. The final problem concerned whether the noise was coming from the drive or the motor. As there was no way of knowing the answer it was assumed the noise was coming from the drive and the associated cables as the motor was constructed from a cast iron case which in theory would prevent any radiation generated within the motor from reaching the antenna.

In conclusion it would appear that the only way to perform repeatable radiated tests, where it was known that the noise was coming the drive, would be to use an anechoic chamber which would eliminate the problem of background noise. This would not solve the problem of small changes in the equipment layout affecting the results.

7.4 Modelling of the Radiated Emissions

The discussions relating to the work done on the radiated emissions have been further broken down into three sections covering finite element modelling and transmission line matrix modelling and a final section comparing these two methods of predicting the radiated emissions.

7.4.1 Finite Element Modelling

A model using two-dimensional finite element theory was presented (chapter 5) for predicting the radiated emissions from variable speed drives. The model took the form of a single plane through the drive which was likely to produce the majority of the radiation. On the drive in question, the Eurotherm 583, This turned out to be the plane which passed through the switching components (the IGBT's), the DC link and also the shielded cable which connected the drive to the motor. The motor which was connected

to the drive was ignored in the model as it was not expected to produce significant amounts of radiation due to the fact that it was encased in a steel casing which in theory would absorb any radiation generated by the windings. The model also took into account the architecture of the test rig used to measure the radiated emissions.

The finite element model was excited using the sources in the time-domain that had been previously generated with the conducted emissions model. An assumption was made that at each time step the model could be assumed to be a static solution as the electromagnetic wave will travel at the speed of light (3×10^8 m/s), hence it can be assumed that the transfer of the electromagnetic wave from the source to the point at which the field is measured (10m from the source) to be instantaneous as the time taken for the wave to travel the 10m is 33.3ns. The only problem with this assumption is that the emissions from the previous time steps will have no effect on the current time step, as each simulation is totally separate. The finite element model initially gave the values for the radiated field in terms of the magnetic field this was easily converted into an electric field. As the field values were in the far field they could be converted into the desired electric field by simply multiplying them by the impedance of free space (Z_O=377Ω).

A second finite element model was produced which took into account the shielded cable which attached the drive to the motor, and this was excited with the differential mode currents which would be seen by the motor and also the common mode currents which were flowing in the shield of the cable. It was found that this cable was producing the majority of the radiation. The reason for this being that the shielded cable is electrically long (total line length is greater than tenth of a wavelength) so it behaves like a monopole antenna which is an efficient source of emissions. Whereas the drive being electrically short (total line length is less than tenth of a wavelength) is a less efficient source of emissions when compared to the shielded cable. Hence it was deduced that the model for the radiation should concentrate on the shielded cable rather than the components contained within the drive as these tend be inefficient sources of radiation. Also the major radiation source was the common mode currents, the reason for this

being that the common mode currents are not balanced like the differential mode currents so the fields produced by them do not sum to zero.

The radiation from the 583 drive was correctly predicted using two-dimensional finite element theory in the frequency range 30MHz to 200MHz, see Figure 7.2, and compared well to measured results which were also in the frequency 30MHz to 200MHz. The EMC legislation covers the frequency range 30MHz to 1000MHz. There is no reason why the radiated model should not be extended to cover the entire frequency range. The reason that the model results only go up 200MHz is that above this frequency it was found that the radiation from the drive was minimal so no measurements were made above 300MHz. The accuracy of the model when compared to the measured results was in the range +10dBμV/m and -6dBμV/m. However it cannot be said that the model has an error of +10dBμV/m and -6dBμV/m as the experimental results are assumed to have a measurement uncertainty in the region of +/-5dB.

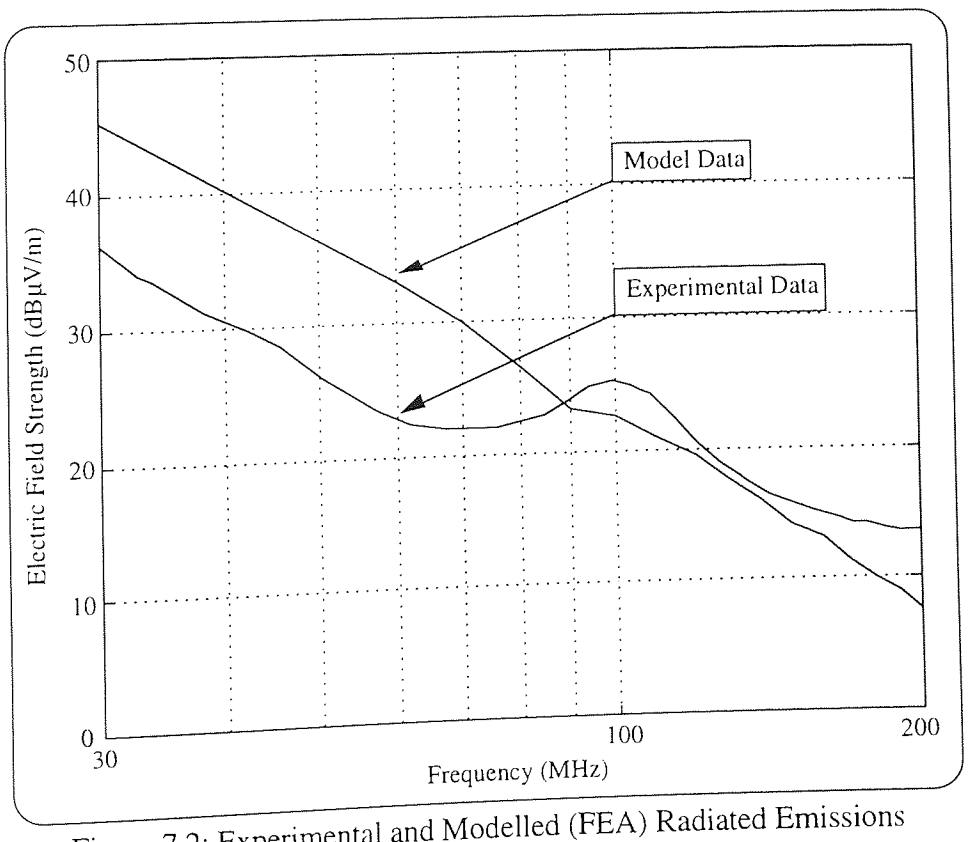

Figure 7.2: Experimental and Modelled (FEA) Radiated Emissions

The advantage of the two-dimensional finite element model used in conjunction with the SABER model is that it will allow a drive designer to determine whether a new design will comply with the EMC legislations, concerning radiated emissions, before a prototype is built, and this means that the designer can build the radiated emissions compliance into the design without having to build costly prototypes and finding out that they fail the EMC legislations.

The finite element models have shown that it is feasible to obtain results that are comparable to the measured results to within +10dB and -6dB by only modelling the shielded cable which connects the drive to the motor, which is excited with the both the differential and common mode currents which are flowing in it.

7.4.2 Transmission Line Matrix Modelling

A model using three-dimensional transmission line matrix modelling theory has been presented (chapter 6) for predicting the radiating emissions from variable speed drives. The model took account of the shielded cable as the finite element model had previously shown that it was feasible to predict the radiation by modelling the cable. The model also took account of the architecture of the test rig that was used to measure the radiated emissions. The main difference between the finite element model and the TLM model was that the TLM model was three-dimensional so the actual layout of the cable could be modelled rather than having to approximate the layout as in the two-dimensional finite element model.

The TLM model was excited with the current that the motor would see. It was not feasible to apply the common mode currents that were flowing in the shield to the problem, because the large number of time steps that the model would needed to take was the same as the amount of points required from the common mode waveform. As it was not a viable solution to write in all the points by hand and it was also not possible to generate an equation to predict the values, the common mode currents could not be applied to the model. If the SABER model had produced a file with all the points for the waveform contained in it, it would have been possible to read the values in from the file

and excite the model with them. The main problem with the TLM method is that the size of the time steps used in the analysis is directly related to the node sizes, and as the node size gets smaller so does the time step used. Obviously the node size is related to problem geometry and in the model that was generated for the 583 drive the node size was chosen to be 0.3m which gave a time step of 0.707ns. As the TLM model was excited with the current that the motor would see it was not possible to predict the electromagnetic radiation generated by the drive. The results from the TLM model were confirmed by comparing them to an identical problem that was run using the previously generated finite element model.

Both problems were excited with the current profile that would be seen by the motor. The problems were both run for a total time of 5ms, this took the TLM model approximately one month of computer time to produce a solution to this problem compared to approximately one day for the finite element model. The results in the time base for the modulus' of the electric fields for both of the models can be seen in Figure 7.3. As can be seen from Figure 7.3 the peak values of the plots are within 1.3 V/m of each other and this corresponds to an variation of 5%. This shows that the TLM method is capable of producing results that are comparable to results produced using a two-dimensional finite element model. Even though the TLM method is capable of producing comparable results to the finite element method, it was still deemed to be a poor solution to the problem. The reason for this being the size of the time steps (for the problem in question t_{step} = 0.707ns) the method uses, as the time steps are so small it therefore means that a large number of time steps need to be taken to run a problem for the desired length of time.

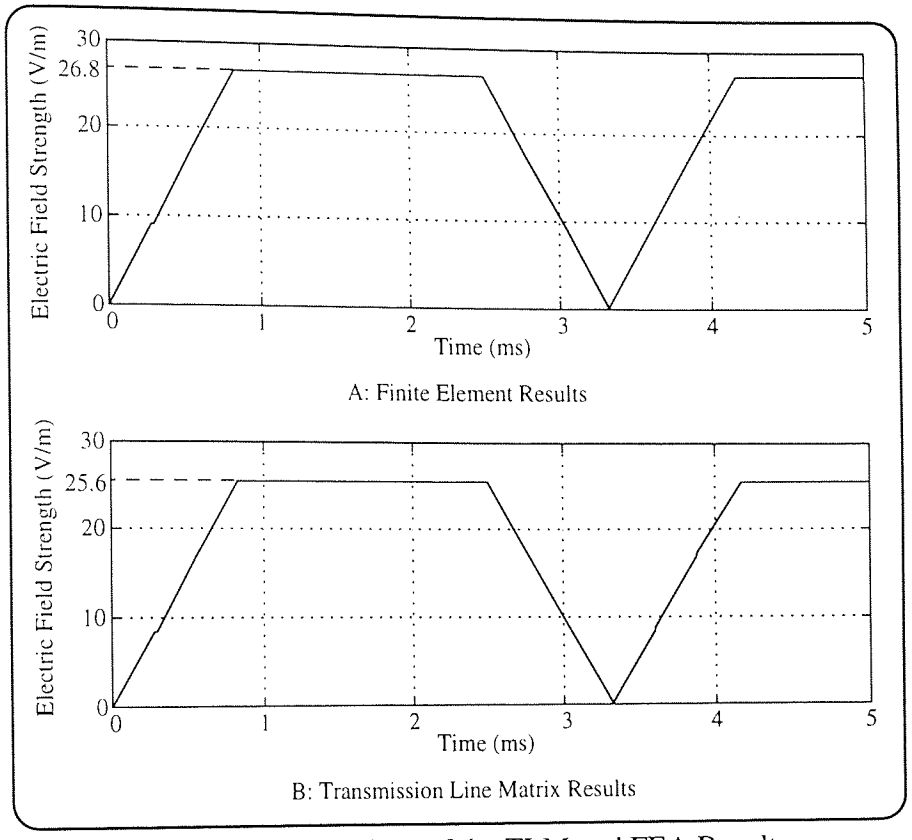

Figure 7.3: Comparison of the TLM and FEA Results

In conclusion it can be said that TLM modelling is not a suitable method for predicting the electromagnetic radiation from variable speed drives, due to the long time that it takes to produce a solution to a problem and also because of the difficulty in applying sources to a problem which cannot be characterised as an equation. However it may be possible to apply the method to predict a drive's level of immunity to an externally applied electromagnetic field.

7.4.3 FEA Versus TLM Modelling

As has been previously discussed two methods of predicting the radiated emissions have been considered. These methods being finite element analysis and transmission line matrix modelling, and the Table 7.1 below compares the two methods.

TLM Modelling	FEA
Theory relatively easy to understand	Theory hard to understand
Computationally inefficient	More efficient than TLM
Only performs transient analysis	Can perform transient, static, frequency etc
Number of iterations is related to the mesh size	Number of iterations when running a transient analysis is not related to the mesh size
Difficult to model fine detail, without making problems very large	Relatively easy to model fine detail
Can produce models which extend into the far field	Cannot produce models which extend into the far field

Table 7.1: Comparison of FEA and TLM Modelling

The first point on the table is not of extreme importance if the software which is being used has been pre-written. However if the software has to be written by the user than it is of extreme importance that the user has a sound understanding of the method. It can also be of some use however to have an understanding of how a method solves a problem even when using pre-written software.

The second point concerns the efficiency of the methods, and the more inefficient the method is the slower it will be to produce an answer to a problem. Computational inefficiency is a major problem with transmission line matrix modelling, which is due to the sheer number of calculations being performed. For a 10 x 10 x 10 node problem the number of equations per iteration is approximately 12,500, this is for a relatively small problem. When the problems become more complex and the number of iterations start to increase it can be seen that a huge amount of calculations would need to be

performed.

The third point shows the inflexibility of the transmission line matrix method when compared to finite element modelling, as the transmission line matrix method can only perform a transient analysis, whereas the finite element method has the ability to perform a number of different forms of analysis.

The forth outlines a major failing of the transmission line matrix method in that the time step size is related to the mesh size, and the smaller the mesh size the smaller the time step and hence the more calculations required to perform the analysis. However with the finite element analysis the transient analysis only generates results at the times specified by the user, and this means that as many or as few results can be generated.

The fifth point concerns the ability of the methods to model fine detail. Both methods are capable of having meshes of different sizes, but with the transmission line matrix method this results in increasing the number of calculations to be performed drastically. With the finite element method it is feasible to have meshes that are constantly varying across the the problem.

The final point concerns the methods ability to model problems in the far field region. The finite element method in the form presented in this thesis is not capable of predicting field profiles in the far field, whereas the transmission line matrix method is fully capable of predicting fields in both the near and far fields.

As can be seen from Table 7.1 the two methods both have their advantages and disadvantages. However it appears that finite element analysis has far more advantages than transmissions line matrix modelling in the fact that it is easier to and quicker to model the problem, even though finite element theory is far more complex than transmission line theory.

7.5 Overall Conclusions

The new and original work that has been presented in this thesis, can be summarised as follows:

1. A method of predicting the conducted emissions to within +/-6dB has been developed using circuit modelling techniques. For this model to produce accurate values of the conducted emissions the parasitic capacitances which provide an important path for the common mode currents must be modelled.

2. The circuit model that was used to predict the conducted emissions can also be used to generate the voltage and current sources which are used when predicting the radiated emissions.

3. A model for predicting the radiated emissions, both magnetic and electric, to within +10dB and -6dB has been developed using two-dimensional finite element theory.

4. The modelling showed that the majority of the radiation generated by the drive was due to the electrically long shielded cables, more specifically the common mode currents that were present in the shield of the cable, that were used to connect the drive to the motor, and that it was feasible to predict the radiation from the drive to within +10dB and -6dB by only modelling the shielded cables.

5. The transmission line matrix modelling method is currently not a suitable method for predicting the electromagnetic radiation profiles from variable speed drives, due to the difficulty of presenting the sources in a suitable format. However it would appear that the method is more suited to predicting a drive's level of immunity to electromagnetic fields.

6. A complete methodology has been developed to predict the electromagnetic radiation, in terms of the conducted and the radiated emissions, from variable speed drives. The methodology uses two models, the first being based on circuit theory and this is used to

predict the conducted emissions and the voltage and current sources which are used to predict the radiated emissions. The second model uses two-dimensional finite element theory to physically model the drive and its associated cables, and is excited with the sources generated using the SABER model. Figure 7.4 shows a flowchart of the complete method.

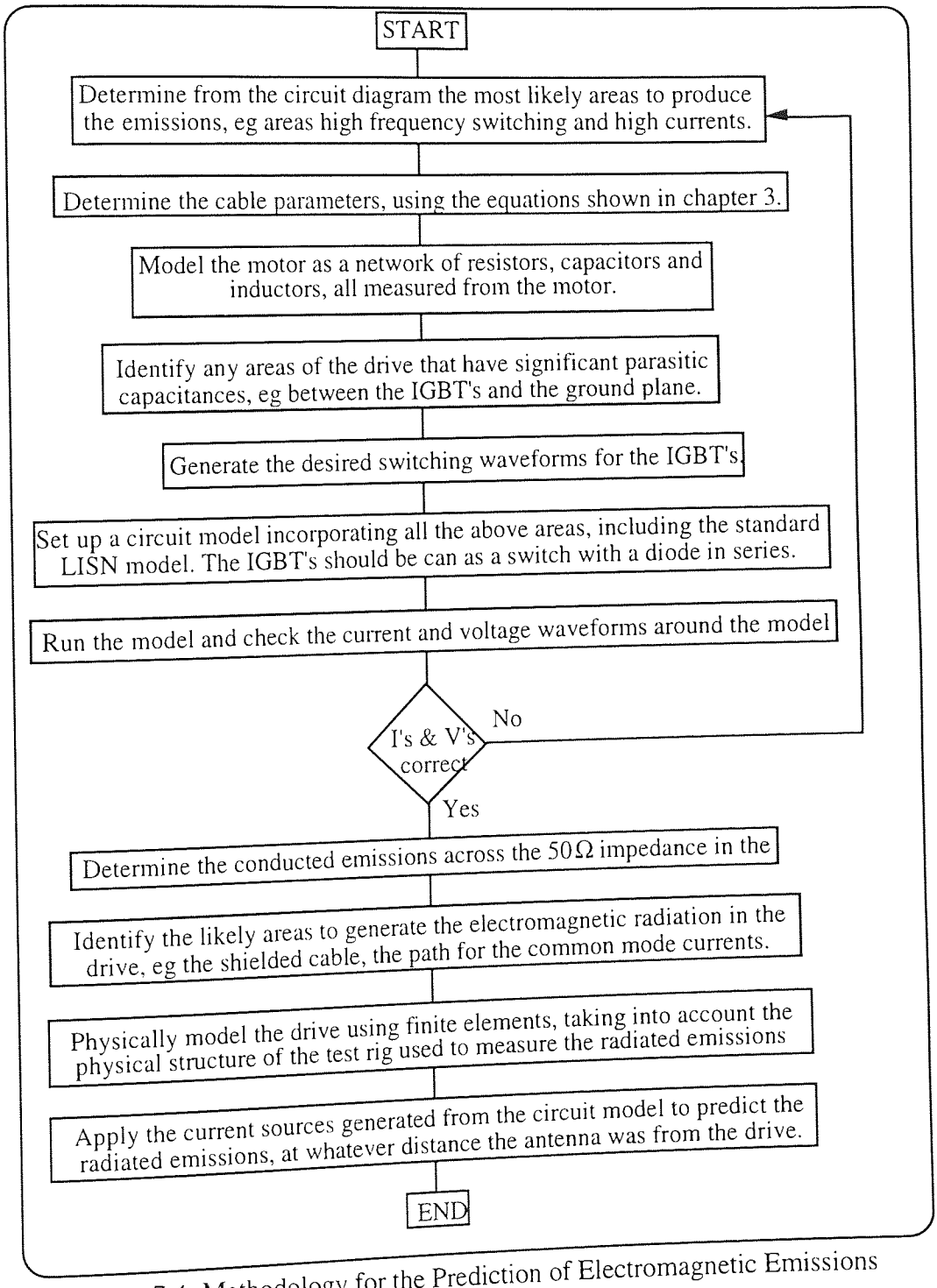

Figure 7.4: Methodology for the Prediction of Electromagnetic Emissions

7.6 Summary

This chapter has discussed the work that has been presented in the preceding chapters, and has drawn a number of conclusions from this discussion. A number of overall conclusions for the work were also drawn, which can be summarised as follows:

1. That it is feasible to predict the conducted emissions to within +/-6dB of measured values using circuit modelling techniques.

2. Circuit modelling techniques can also be used to generate current and voltage sources for use in predicting the radiated emissions.

3. Theory showed that is is possible to predict the radiated emissions to within +10dB and -6dB of measured values using two-dimensional finite element theory.

4. The majority of the radiation from the drive is in fact being generated by the shielded cable which connects the drive to the motor.

5. The transmission line matrix modelling method is currently not a suitable method for predicting the electromagnetic radiation profiles from variable speed drives, due to the difficulty of presenting the sources in a suitable format.

6. A complete methodology has been developed to predict the electromagnetic radiation, in terms of the conducted and the radiated emissions, from variable speed drives.

Chapter 8

Future Work

8.1 Introduction

Throughout the work presented in this thesis a number of areas of work, which were outside the realms of this project, were identified. The following sections outline what these areas are, and in certain cases suggest possible solutions.

8.2 Circuit Modelling (chapter 3)

A method needs to be developed for the prediction of the parasitic capacitances in the drive, as currently they can only be measured from the drive. This implies that before the conducted emissions model can be set up a mock up of the areas of the drive where there are significant parasitic capacitances, for example between the IGBT stack and the ground plane, needs to be built and the parasitic capacitances measured.

As the drive may fail to meet the limits set down in the legislations, a method for designing filters based on the results from the circuit model needs to be developed.

The circuit models could be rewritten as a specific piece of software which could be used to predict the conducted emissions and also to assist in the design of filters to allow the drive to meet the limits set in the legislations. This would speed up the process of modelling a specific drive, as common sections of each drive and the test rig used to measure the emissions could be set up as templates within the software.

8.3 Measurement Techniques (chapter 4)

As was said in chapter 4, the technique that is currently used for the measurement of the radiated emissions is not ideal as it tends to introduce errors, which cannot be quantified, into the results. The methods of measuring the radiated emissions need to be examined so as to make them more repeatable and also to make the errors present quantifiable. Some measurement techniques which could be looked are the use of shielded/anechoic chambers, and also the GTEM (Gigahertz Transverse Electromagnetic Mode) cell.

8.4 Prediction of the Radiated Emissions (chapters 5 and 6)

A comparison of various other methods of predicting the radiating emissions from variable speed drive's using other modelling techniques, for example the method of moments and finite difference time domain methods, to determine which method is the best one or which method is the best one for which type of problem. It may also be useful to compare both two-dimensional and three-dimensional solutions to identical problems using identical methods.

It would also be useful to check the conclusion that the majority of the emissions are due to the shielded cable which connected the drive to the motor, by setting up some simple models using such theorems as Biot-Savart and generating the emissions profile in the near field.

8.5 TLM Modelling (chapter 6)

The number of iterations which are required to model a problem needs to be reduced if the method is to be used for radiated emissions modelling, because currently a large number of iterations are required to model a problem for any significant length of time. For example the TLM models presented in this thesis required approximately 7.1 million iterations to correctly model the problem, as each iteration took a third of a second this corresponds to a time of approximately 27 days (using a 100MHz machine), which is far to long. As the models developed in this thesis are intended for use in industry it is not practical for a design tool to take several days to produce a solution to a problem.

8.6 Immunity Models

As the work presented in this thesis was totally concerned with the emissions generated by variable speed drives, the issue of immunity models was not considered. However it is an important part of the EMC directive, and as such it is of prime concern that modelling techniques which can predict a drive's behaviour under the influence of

external electromagnetic interference are generated.

The conducted susceptibility test could be modelled using the SABER model and injecting the required voltages and currents into the model, and then monitoring the behaviour of the model to see the effects of the conducted emissions on the drive.
The radiated immunity test could be modelled by exposing the finite element model of the drive to a radiated field of the relevant magnitude and frequency, and measuring the generated currents and voltages around the system. These currents and voltages would then be passed onto the SABER model where their effects on the operation on the drive could be determined.

The electrostatic discharge test would be modelled with a combination of a TLM model and the SABER model, depending on where the discharge was applied. If the discharge was applied to a plastic casing the initial modelling would be done using a TLM model and the currents and voltages generated on the drive would then be applied to SABER model to determine the effects on the operation on the drive.

REFERENCES

Al-Mukhtar. D. A, Sitch. J, E, (1981), "Transmission Line Matrix Method with Irregularly Graded Space", IEE Proceedings Part H, **128** (6), 299-305

Analogy UK Ltd., (1990), SABER User Manual, Cherry Orchard West, Kembrey Park, Swindon SN2 6UP

Bergervoet. J. R, (1994), "EMC Measurements And Models Connecting The System Level With The Module Level", Phillips Journal of Research, **48** (1-2), 63-81

Boglietti. A, Chiampi. M, Chiarabaglio. D, (1990), "Development And Use Of Finite Element Software For Electromechanical Analysis", Conference on Electrical Engineering Analysis, Massachusetts, pp 123-134

Burnett. D. S, (1987), Finite Element Analysis: From Concepts to Applications (1st edition), Addison Wesley, Wokingham, Great Britain

Cerri. G, DeLeo. R, Primiani. V. M, (1993), "A Rigorous Model for Radiated Emission Prediction in PCB Circuits", IEEE Transactions On Electromagnetic Compatibility, **35** (1), 102-109

Christopoulos. C, Herring. J. L, (1993), "The Application Of Transmission-Line Modelling (TLM) To Electromagnetic Compatibility Problems", IEEE Transactions On Electromagnetic Compatibility, **35** (2), 185-191

Christopoulos. C, (1995), Transmission-Line Modelling Method (1st edition), Oxford University Press, Oxford, Great Britain

Christopoulos. C, (1992a), "Electromagnetic Compatibility Part 1 General Principles", Power Engineering Journal, **6** (2), 89-64

Christopoulos. C, (1992b), "Electromagnetic Compatibility Part 2 Design Principles", Power Engineering Journal, **6** (5), 239-247

Christopoulos. C, (1990), "Field Analysis Software Based On The Transmission-Line Modelling Method", Conference On Electrical Engineering Software, Massachusetts, pp 135-148

Coenen. M. J, (1994), "EMC Workbench: Testing Methodology, Module Testing and Standardisation", Phillips Journal of Research, **48** (1-2), 83-115

Conner. F. R, (1982), Noise (2nd edition), Edward Arnold, London, England

Conway. G. A, (1994), "A.C Drives: Electrical Disturbance Problems And Solutions", Colloquium on Predicting and Assuring EMC in the Power Electronics Area, London, pp 4/1-4/5

Cook. S, (1990), "A Question Of Development Or Discipline", New Electronics, **23** (9), 81-83

Davies. E. R, (1993), Electronic Noise and Signal Recovery (1st edition), Academic Press Inc, London, England

Degauque. P, Hamelin. J, (1193), Electromagnetic Compatibility (1st edition), Academic Press Inc., London, England

Department of Trade And Industry, (1992), The Single Market, Electromagnetic Compatibility (2nd edition), Department of Trade And Industry, London, Great Britain

Dixon. D. S, Obara. M, Schade. N, (1993), "Finite-Element Analysis (FEA) as an EMC Prediction Tool", IEEE Transactions On Electromagnetic Compatibility, **35** (2), 241-248

Duffy. A. P, Herring. T. M, Benson. T. M, Christopoulos. C, (1993), "The Application of Transmission-Line Modelling to EMC Design", Colloquium on Does Electromagnetic Modelling Have a Place in EMC Design, London, pp 5/1-5/5

Goebloed. J, (1990), Electromagnetic Compatibility (1st edition), Prentice-Hall, New York, USA

Green. T. C, (1994), "The Impact of EMC Regulations on Mains-Connected Power Converters", Power Engineering Journal, **8** (1), 35-43

Hargis. C, (1994), "Design of a PWM AC Variable Speed Motor Drive for Conducted Emission Compliance", Conference Proceedings EURO EMC'93, Tunbridge Wells, 89-92

Hefner. A R, Blackburn. D. L, (1988), "An Analytical Model For the Steady-state and Insulated Characteristics of the Power IGBT", Solid-State Electronics, **31** (10), 1513-1532

Herring. J. L, (1993), "Developments in the Transmission-Line Modelling Method for Electromagnetic Compatibility Studies", Ph.D. Thesis, University of Nottingham

Herring. J. L, Christopoulos. C, (1994), "Solving Electromagnetic Field Problems Using a Multiple Grid Transmission-Line Modelling Method", IEEE Transactions on Antennas and Propagation, **42** (12), 1654-1658

Hoefer. W. J. R, So. P. P. M, (1992), The Electromagnetic Wave Simulator (third edition), John Wiley & Sons, Chichester, England

Hoefer. W. J. R, (1985), "The Transmission Line Matrix Method Theory and Applications", IEEE Transactions on Microwave Theory Applications, **33** (10), 882-893

Hubing. T. H, (1991), " Survey of Numerical Electromagnetic Modelign Techniques", University of Missiouri-Rolla, EMC Laboratory, Report No: TR91-1-001.3

Hubing. T. H, Kaufman. J. F, (1989), "Modelling the Electromagnetic Radiation from Electrically Small Table Top Products", IEEE Transactions on Electromagnetic Compatibility, **31** (1), 74-84

Huygens. C, (1690), Traite de la Lumiere, Leiden

IEC, (1993), EMC Product Standard Including Specific Test Methods for Power Drive Systems, IEC 22G-WG4 (Cv) 5

Jackson. G. A, (1989), "Survey of EMC Measurement Techniques", Electronics and Communication Engineering Journal", **1** (2), 61- 70

Johns. D. P, Wlodarczyk. A. J, Mallik. A, Scaramuzza. R, (1993), "The Role of TLM in EMC Design", Colloquium on Does Electromagnetic Modelling Have a Place in EMC Design, London, pp 9/1-9/5

Johns. P. B, (1987), "A Symmetrical Condensed Node for the TLM Method", IEEE Transactions on Microwave Theory and Practice, **35** (4), 370-377

John. P. B, Beurle. R.L, (1971), "Numerical Solution of 2-Dimensional Scattering Problems Using a Transmission Line Matrix", Proceedings of the IEE, **118** (9), 1203-1208

Khan. R. L, Costache. G. I, (1989), "Finite Element Method Applied to Modelling Crosstalk Problems on Printed Circuit Boards", IEEE Transactions On Electromagnetic Compatibility, **31** (1), 5-15

Kraus. J. D, (1992), Electromagnetics (4th edition), McGraw Hill, London, England

Laroussi. R, Costache. G. I, (1993), "Finite-Element Method Applied To EMC Problems", IEEE Transactions On Electromagnetic Compatibility, **35** (2), 178-184

Lin. F, Chen. D.Y, (1994), "Reduction of Power Supply EMI Emission by Switching Frequency Modulation", IEEE Transactions on Power Electronics, **9** (1), 132-137

Macleod. A, (1993), "Care with Installation Ensures Compatibility is Maintained", New Electronics, **26** (11), 57-59

Mahdavi. J, Roudet. J, Scheich. R, (1993), "Conducted RFI Emissions from an AC/DC Converter with Sinusoidal Line Current", 1993 IEEE Industry Applications Meeting, Part 2 (of 3), Toronto, Canada, pp 1048-1053

Mahdavi. J, Roudet. J, Scheich. R, (1993), "Common Mode Conducted RFI Emissions of an AC/DC Converter with Sinusoidal Line Current", IEE Power Electronics and Variable Speed Drives Conference, London, Great Britain, pp 632-637

Marvin. A. C, (1991), "Measurement Environments And Testing", EMI And EMC, Portugal: AGARD, pp 8-1 to 8-24

Mitter. C. S, Hefner. A. R, Chen. D. Y, Lee. F. C, (1993), "Insulated Gate Bipolar Transistor Modelling Using IG-SPICE", IEEE Transactions on Industry Applications, **30** (1), 24-32

Naylor. P, Christopoulos. C, (1990), "A New Wire Node for Modelling Thin Wires in Electromagnetic Field Problems Solved by Transmission Line Modelling", IEEE Transactions on Microwave Theory and Techniques, **38** (2), 328-330

Paul. C. R, (1991), "Cables And Crosstalk", EMI And EMC, Portugal: AGARD, pp 4-1 to 4-13

Paul. C. R, (1989a), "Modelling Electromagnetic Interference Properties Of PCB'S", IBM Journal Of Research And Development, **33** (1), 33-50

Paul. C. R, (1989b), "A Comparison of the Contributions of Common-Mode and Differential-Mode Currents in Radiated Emissions", IEEE Transactions On Electromagnetic Compatibility, **31** (2), 189-193

Paul. C. R, (1980), "Effects of Pigtails on Crosstalk to Braided-Sheild Cables", IEEE Transactions On Electromagnetic Compatibility, **22** (3), 161-1172

Paul. C. R, (1979a), "Prediction Of crosstalk In Ribbon Cables: Comparison Of Model Prediction And Experimental Results", IEEE Transactions On Electromagnetic Compatibility, **20** (3), 394-406

Paul. C. R, (1979b), "Solution Of The Transmission-Line Equations For Three-Conductor Lines In Homogeneous Media", IEEE Transactions On Electromagnetic Compatibility, **20** (1), 216-222,

Paul. C. R, McKnight. J. W, (1979a), "Prediction Of Crosstalk Involving Twisted Pairs Of Wires-Part I: A Transmission-Line Model For Twisted-Wire Pairs", IEEE Transactions On Electromagnetic Compatibility, **21** (2), 92-105

Paul. C. R, McKnight. J. W, (1979b), "Prediction Of Crosstalk Involving Twisted Pairs Of Wires-Part II: A Simplified Low-Frequency Prediction Model", IEEE Transactions On Electromagnetic Compatibility, **21** (2), 105-114

Popovic. B. D, (1973), Introductory Engineering Electromagnetics (2nd edition), Addison Wesley, Massachusetts, USA

Rafinejad. P, Sabonnadiere. J. C, (1976), "Finite Element Computer Program in Design of Electromagnetic Devices", IEEE Transactions On Magnetics, **12** (5), 575-578

Rashid. M. H, (1993), SPICE For Power Electronics And Electric Power (1st edition), Prentice Hall, Englewood Cliffs, New Jersey, USA

Simms. J. R, (1992), "Electromagnetic Compatibility for the Power Engineer", Power Engineering Journal, **6** (6), 279-286

Taylor. J, (1994), "Controlling Noise From High Speed Inverters", Drives And Controls, **10** (3), 84-85

Tirkas. P. A, Balanis. C. A, Purchine. M. P, Barber. G. C, (1993), "Finite-Difference Time-Domain Method For Electromagnetic Radiation, Interference, And Interaction With Complex Structures", IEEE Transactions On Electromagnetic Compatibility, **35** (2), 192-203

Vance. E. F, (1975), "Shielding Effectiveness of Braided-Wire Shields", IEEE Transactions on Electromagnetic Compatibility, **17** (2), 71-77

Vector Fields, (1995), PC-OPERA User Manual, 24 Bankside, Kidlington, Oxford OX5 1JE

Warren. P. J, (1993), "EMC Modelling, a Method for Reducing Emissions: Modelling PCB, Cables, and Connectors Using the Greenfield Transmission Line Simulator From Quantic Laboratories Inc.", Colloquium on Does Electromagnetic Modelling Have a Place in EMC Design, London, pp 4/1-4/4

Williams. T, (1994), EMC for Product Designers (1st edition), Newnes, Oxford, Great Britain

Appendix 1

Description of Equipment Modelled

A1.1 The 583 Drive

Company Name	: Eurotherm Drives
Code Number	: 583
Supply Voltage	: 220/240 V
Supply Current	: single phase - 10A
	three phase - 6A
Supply Frequency	: 50/60 Hz
Output Voltage	: 220/240 V
Output Current	: 5.5 A
Output Frequency	: 0-100/120 Hz
Output Power	: 1.1 KW

A1.2 The Induction Motor

Company Name	: ABB
Frequency	: 50/60 Hz
Power	: 1.5/1.75 KW
Speed	: 1420/1710 rev/min
Maximum Voltage	: 380-420 / 440-480 V when wired in Y
	220-240 / 250-280 V when wired in Δ
Maximum Current	: 3.7/3.6 A when wired in Y
	6.4/6.3 A when wired in Δ

Appendix 2

Software Used

A2.1 The SABER Simulator

This appendix presents an overview of the SABER simulator.

A simulator is often compared with an oscilloscope because they perform the same basic function, which is to measure the behaviour of a system or device, but the instruments are very different. The oscilloscope operates in a real world environment, while the simulator operates in an quasi-real environment which is composed of mathematical expressions that resemble physical laws.

The SABER simulator is a product sold by Analogy Inc.. The SABER simulator has a unique architecture that makes the simulation of a system independent from the modelling of its components. This feature of the SABER simulator means that it is possible to produce highly detailed models of individual components, and then to combine these models together to create systems.

The SABER simulator is provided with a vast library of models, which range from resistors to electric motors to hydraulics. The SABER simulator also has the ability to model any system that can be defined using piecewise-continuous algebraic and ordinary differential equations, equations that change value in a step-wise manner. This means that the user can write his own models, which can then be used to model a complete system.

Finally, the SABER simulator can run seven different types of simulation on the system:

DC - The DC analysis finds the time-independent, steady state operating point for the system.

DC Transfer - The DC transfer analysis finds a series of DC operating points, based on a sweep of a voltage or current source, with derivatives set to 0.

Transient - The transient analysis analyses the response of the system in the time domain.

DCTR - The DCTR analysis is a DC analysis followed immediately by a transient analysis, where the initial point output of the DC analysis is the input to the transient part.

AC - The AC analysis, also called the frequency analysis, analyses the system in the frequency domain.

Noise - The noise analysis analyses the effects of small signal noise in a frequency domain analysis of a system.

Distortion - The distortion analysis calculates the small signal distortion in an output signal around an operating point as a function of frequency.

Fourier - The Fourier provides the spectral components of a signal.

A2.2 PC-OPERA

This appendix presents an overview of the finite element package PC-OPERA.

PC-OPERA is a two-dimensional finite element package developed and marketed by Vector Fields Ltd. The package is specifically designed for the electromagnetic analysis and simulation of devices in which the third dimension is not a significant factor in the analysis. The program uses finite element theory to solve the partial differential equations that describe the behaviour of the fields, for example the Poisson and Laplace equations.

The package is capable of producing either electric or magnetic solutions to a problem and is also capable of applying scalar and vector magnetic potentials where relevant. It is also feasible to model non-linear materials such as magnets by supplying information

concerning the B-H curves. The finite element that is used in the analysis is triangular and may be first order (3 noded) or second order (6 noded) for higher accuracy.

PC-OPERA can perform nine types of analysis which can be grouped under the headings of static analysis, eddy currents, stress analysis and thermal analysis:

STATIC ANALYSIS

Static - Performs a linear or non-linear magnetostatic or electrostatic analysis on isotropic materials and permanent magnets.

Adaptive Statics - The same as the static analysis but with self-adaptive mesh refinement to reduce the errors associated with the mesh density.

Packing Factor - A special version of the static analysis for laminated materials which are defined with a packing factor.

Electrostatics - Includes the effects of space charge from particle beams.

EDDY CURRENTS

AC Analysis - Steady state ac eddy currents with linear materials and either voltage or current driven sources.

Transient - Transient eddy currents with multiple drives and linear or non-linear materials. Where the inputs can either take the form of a standard function eg sine, or they can be generated using 'time-tables' which take the form of the time and the value of the wave at each time step.

Velocity - Eddy currents induced by constant velocity motion of one part of the model with respect to the rest.

STRESS ANALYSIS

Stress - Calculates the stress on a model using as an input the forces calculated form an earlier electromagnetic analysis.

THERMAL ANALYSIS

Thermal - Calculates the thermal effects on a model using nodal temperatures and power densities calculated form an earlier electromagnetic analysis.

Appendix 3

Circuit Diagrams

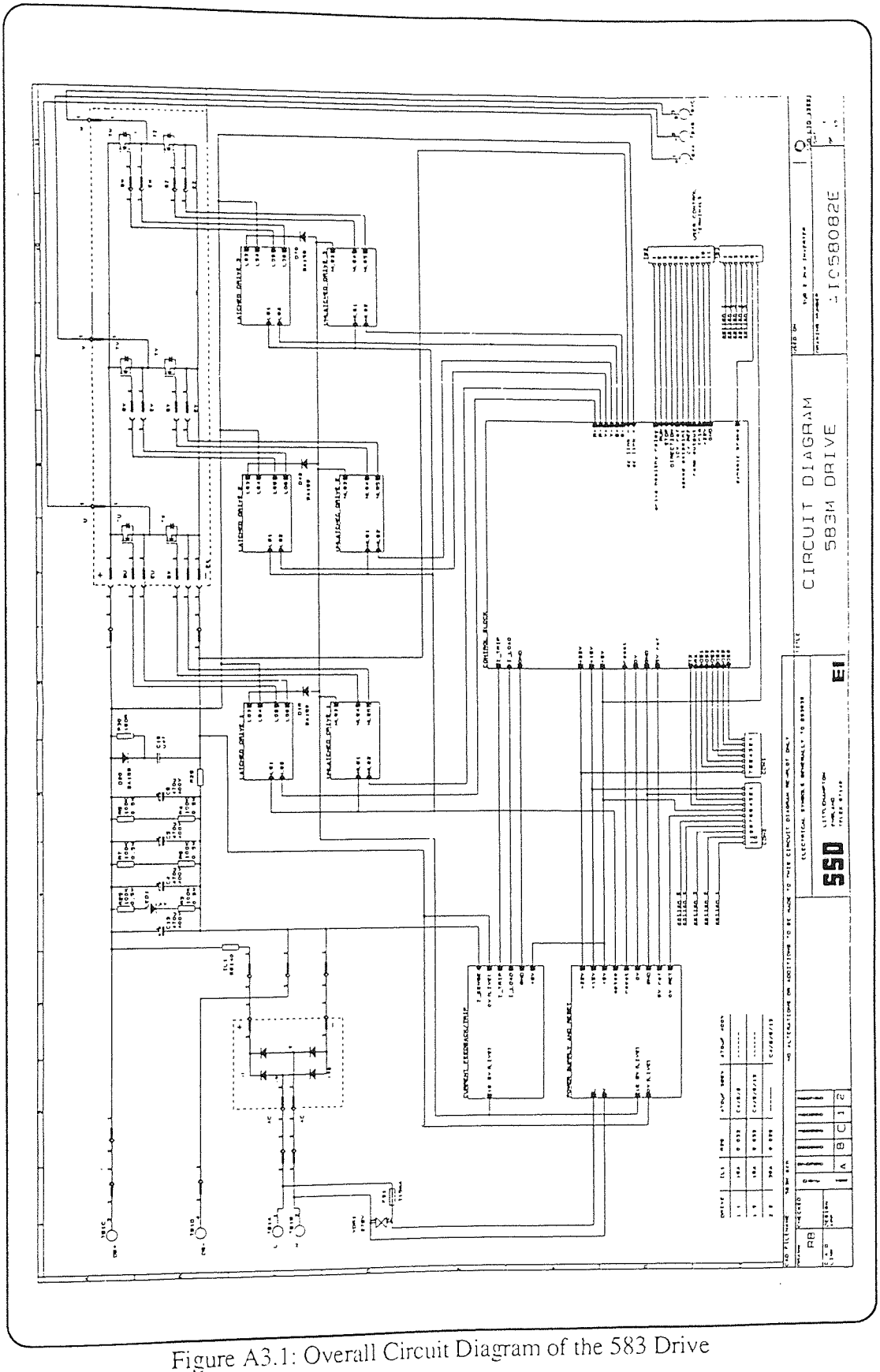

Figure A3.1: Overall Circuit Diagram of the 583 Drive

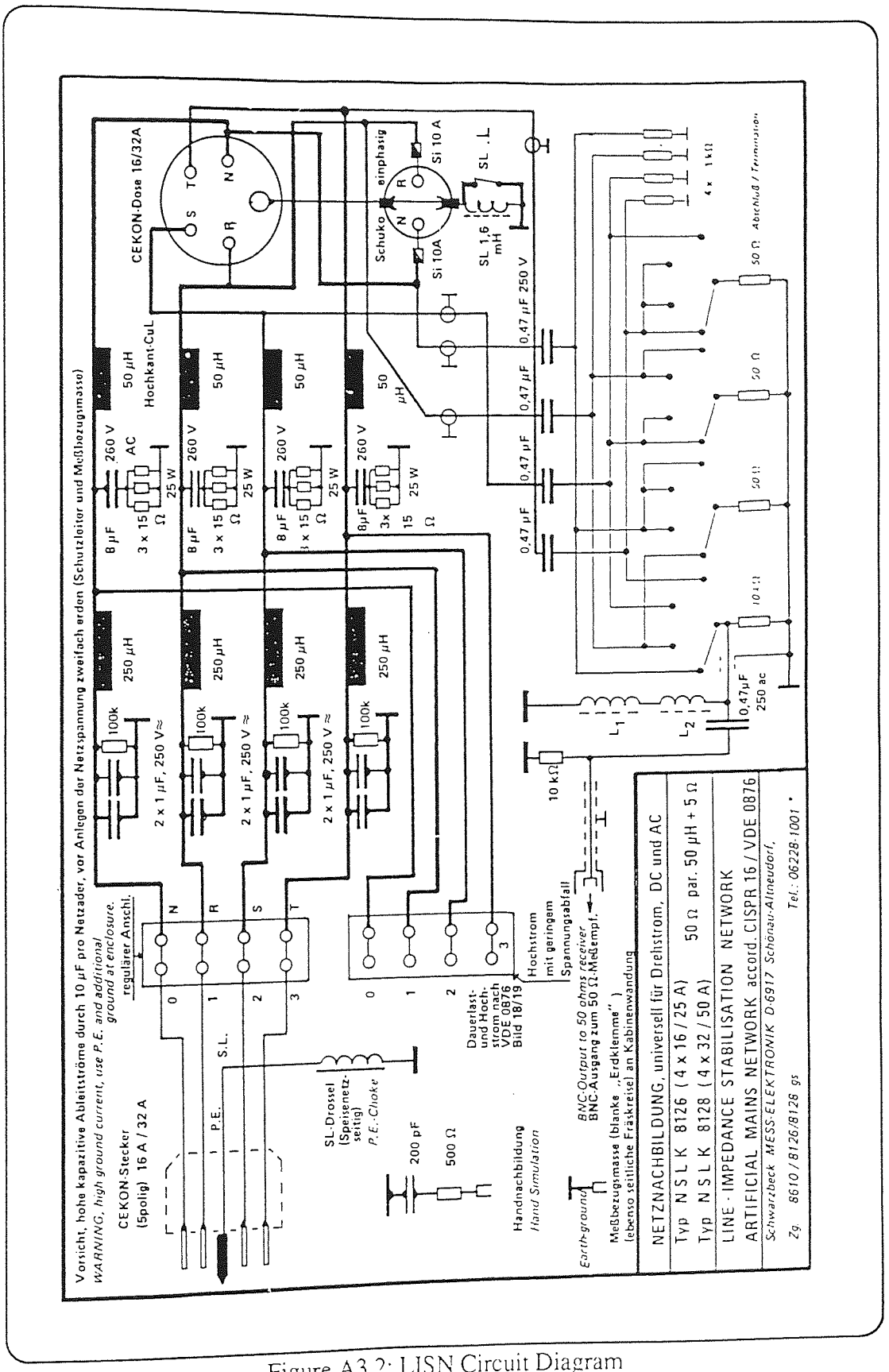

Figure A3.2: LISN Circuit Diagram

Appendix 4

Default Values for SABER Templates

A4.1 IGBT Default Values

High level excess carrier lifetime.	1 μs
Metallurigcal base width.	0.01 cm
Base doping concentration.	2e14 cm^{-3}
Device active area.	0.1 cm^2
Gate drain overlap active area.	0.05 cm^2
Emitter electron satauration current.	10 fA
MOSFET channel threshold voltage.	5 V
Intrinsic anode series resistance.	0.01 Ω
Empirical factor that models MOSFET transconductance reduction due to transverse electric field.	0.01 V^{-1}
Empirical factor to model ratio of MOSFET channel transconductance in triode region to that in saturation for MOSFET.	2
MOSFET channel transconductance in saturation region.	1 AV^{-2}
Gate source capacitance.	1 nF
Gate drain oxide capacitance.	2 nf
Gate drain overlap depletion threshold.	0 V
Avalanche uniformity factor.	1
Avalanche multiplication exponent.	4
Temperature for which parameters apply.	27 ^{o}C
Minimum slope for MOSFET current.	1 pS
Initial conditions on the gate source voltage and on the anode cathode voltage respectively.	undef V, undef V
Maximum power dissipation with junction to ambient thermal resistance.	undef W
Maximum power dissipation with junction to case thermal resistance and heat sink thermal resistance.	undef W

Maximum internal temperature.	undef ^{o}C
Minimum internal temperature.	undef ^{o}C
Maximum anode cathode voltage.	undef V
Maximum gate cathode voltage.	undef V
Maximum average (continuous) anode current.	undef A
Maximum instantaneous (pulsed) anode current.	undef A
Junction to ambient thermal resistance.	undef $^{o}C\ W^{-1}$
Junction to case thermal resistance.	undef $^{o}C\ W^{-1}$
Heat sink thermal resistance.	undef $^{o}C\ W^{-1}$

A4.2 Diode Default Values

Saturation current.	1e-14 A
Ohmic Contact Resistance.	0 Ω
Emission coefficient (must be greater than zero).	1
Transit time.	0 s
Junction capacitance.	0 F
Junction potential.	1 V
Junction grading coefficient.	0.5
Activation energy.	1.11 eV
Saturation current temperature exponent.	3
Flicker noise coefficient.	$0\ A^{2}Hz^{-1}$
Flicker noise exponent.	1
Forward bias junction capacitance coefficient.	0.5
Reverse breakdown voltage.	undef V
Current at Reverse breakdown voltage.	1e-3 A
Temperature at which parameters are defined.	27 ^{o}C
Junction minimum conductance.	1e-12 S
Relative tolerance.	0.0001

Area multiplier (must be nonzero).	1
Noise flag (if zero noise is not calculated).	0
Initial conditions on the voltage across the diode.	undef V
Peak inverse voltage.	undef V
Maximum average current.	undef A
Maximum peak current.	undef A
Maximum internal temperture.	undef ^{o}C
Minimum internal temperture.	undef ^{o}C
Maximum power dissipation with junction to ambient thermal resistance.	undef W
Maximum power dissipation with junction to case thermal resistance and heat sink thermal resistance.	undef W
Junction to ambient thermal resistance.	undef ^{o}C
Junction to case thermal resistance.	undef ^{o}C
Heat sink thermal resistance.	undef ^{o}C

Appendix 5

The SABER Programes

A5.1 SABER Model Netlist

```
#########################################################################
# A program to predict the behaviour of the Eurotherm 583 drive and associated        #
# equipment. The program is constructed from the following five areas of the drive    #
# during the conducted emissions testing:                                             #
# 1.The Line Impedance Stabilising Network (LISN)                                     #
# 2. The power electronics side of the 583 drive                                      #
# 3. The induction motor that was connected to the drive during all the testing.      #
# 4. The shielded cable which connected the motor to the 583 drive.                   #
# 5. The parasitic capacitances that were present in the system.                      #
#                                                                                     #
# Written for use in the SABER circuit simulator.                                     #
#                                                                                     #
# Written by J. Maggs, August 1994                                                    #
#########################################################################
#
# SINGLE PHASE SUPPLY
#
v.in 1 2 = tran = ( sin =(vo=0, va=240, f=50))
#
# LISN
#
r.1 1 0 = 100k
r.2 2 0 = 100k
c.1 2 0 = 2u
c.2 1 0 = 2u
l.1 2 7 = 250u
l.2 1 5 = 250u
c.3 5 6 = 8u
c.4 7 8 = 8u
r.3 6 0 = 5
r.4 8 0 = 5
l.3 7 9 = 50u
l.4 5 10 = 50u
c.16 10 33 = 0.47u
c.17 9 32 = 0.47u
r.18 32 0 = 50
r.19 33 0 = 50
#
# BRIDGE RECTIFIER
#
di.1 9 103
di.2 100 9
di.3 10 103
di.4 100 10
#
# CAPACITANCES FROM BRIDGE RECTIFIER TO GROUND
#
c.22 10 0 = 120p
c.23 9 0 = 120p
#
# SMOOTHING AND DECOUPLING CIRCUITS
#
r.5 102 103 = 0.055
```

```
r.6 102 13 = 100K
r.7 13 100 = 100k
c.6 400 100 = 470u
r.8 102 14 = 100K
r.9 14 100 = 100K
c.7 102 100 = 470u
c.8 102 100 = 470u
r.10 102 100 = 200K
r.20 100 101 = 0.033
r.13 102 16 = 180
c.9 16 101 = 0.47u
di.5 102 16
#
# SWITCHING UNIT (TRANSISTORS CONSTRUCTED FROM AN IDEAL
# SWITCH WITH A DIODE IN SERIES), THE SWITCH MODEL CAN BE
# REPLACED WITH THE IGBT MODEL PRESENTED IN APPENDIX 5.2
#
sw_l4.1 500 19 17
sw_l4.2 19 510 18
sw_l4.3 501 22 20
sw_l4.4 22 511 21
sw_l4.5 502 25 23
sw_l4.6 25 512 24
di.21 200 500
di.22 200 501
di.23 200 502
di.24 510 300
di.25 511 300
di.26 512 300
#
# CAPACITANCES FROM IGBT'S TO GROUND
#
c.24 800 0 = 165p
c.25 22 0 = 165p
c.26 25 0 = 165p
#
# SWITCHING UNIT (DIODES)
#
di.6 19 200
di.7 22 200
di.8 25 200
di.9 300 19
di.10 300 22
di.11 300 25
#
# TRANSMISSION LINE FROM DRIVE TO MOTOR
#
r.15 50 26 = 0.0274
r.16 51 27 = 0.0274
r.17 52 28 = 0.0274
l.6 26 29 = 3u
l.7 27 30 = 3u
l.8 28 31 = 3u
c.10 810 0 = 924.7p
c.11 27 0 = 924.7p
c.12 28 0 = 924.7p
```

```
c.13 29 30 = 462p
c.14 30 31 = 462p
c.15 29 31 = 462p
#
# MOTOR
#
r.23 30 40 = 30
r.21 29 41 = 30
r.22 31 42 = 30
c.18 820 0 = 1.6n
c.19 30 0 = 1.6n
c.20 31 0 = 1.6n
l.9 29 40 = 22m
l.10 30 42 = 22m
l.11 41 31 = 22m
#
# PWM CONTROL VOLTAGES
#
pwmt.1 17 = 0.228m
pwmt.2 18 = 10.228m
pwmt.3 20 = 6.928m
pwmt.4 21 = 16.928m
pwmt.5 23 = 13.528m
pwmt.6 24 = 3.528m
#
# INTERNAL CAPACITANCE OF THE IGBT"S
#
c.30 200 19 = 1.75n
c.31 19 300 = 1.75n
c.32 200 22 = 1.75n
c.33 22 300 = 1.75n
c.34 200 25 = 1.75n
c.35 25 300 = 1.75n
#
# CURRENT MEASUREMENT
#
v.m1 19 50 = dc = 0
v.m2 22 51 = dc = 0
v.m3 25 52 = dc = 0
v.m4 102 200 = dc = 0
v.m5 101 300 = dc = 0
v.m6 102 400 = dc = 0
v.m10 19 800 = dc = 0
v.m20 26 810 = dc = 0
v.m30 29 820 = dc = 0
v.m40 10 830 = dc = 0
```

A5.2 IGBT Template

```
#########################################################################
# Template written to model the IGBT's in the SABER model, the IGBT model being  #
# based on Hefner's IGBT model.                                                   #
#                                                                                 #
# Written using MAST (SABER modelling language)                                   #
#                                                                                 #
# Written by J. Maggs, July 1994                                                  #
#########################################################################

template trig a g k
electrical a, g, k
{
igbt.john a g k = model = (vt = 5.9, cgs = 900p, tnom = 25, theta = 0.02, rs = 0.15)
}
```

A5.3 Diode Template

```
#########################################################################
# Template written to model the diodes's in the SABER model.                      #
#                                                                                 #
# Written using MAST (SABER modelling language)                                   #
#                                                                                 #
# Written by J. Maggs, July 1994                                                  #
#########################################################################

template dmod a b
electrical a, b
{electrical c
val i i
d.john a c = model =(vj = 0.85, bv = 1400, ibv = 0.1m, tnom = 25)
r.1 c b = 0.04
when (i == 0) {
                schedule_next_time(time)
                }
}
```

A5.4 PWM Template

```
#########################################################################
# Template written to model the PWM waveform in the SABER model. The times      #
# used in the template correspond to times measured off the Eurotherm 583 drive.      #
#                                                                                     #
# Written using MAST (SABER modelling language)                                       #
#                                                                                     #
# Written by J. Maggs, July 1994                                                      #
#########################################################################

element template pwmt out = start
state logic_4 out
number start = 0

{
state nu wake_up
when(time_init) {
        schedule_event(time, out, l4_0)
        schedule_event(start, wake_up, 0)
                }

when (event_on(wake_up)) {
        schedule_event(time,out,l4_1)
        schedule_event(time+0.228m,out,l4_1)
        schedule_event(time+0.273m,out,l4_0)
        schedule_event(time+0.660m,out,l4_1)
        schedule_event(time+0.774m,out,l4_0)
        schedule_event(time+1.092m,out,l4_1)
        schedule_event(time+1.251m,out,l4_0)
        schedule_event(time+1.502m,out,l4_1)
        schedule_event(time+1.729m,out,l4_0)
        schedule_event(time+1.934m,out,l4_1)
        schedule_event(time+2.207m,out,l4_0)
        schedule_event(time+2.366m,out,l4_1)
        schedule_event(time+2.707m,out,l4_0)
        schedule_event(time+2.821m,out,l4_1)
        schedule_event(time+3.162m,out,l4_0)
        schedule_event(time+3.231m,out,l4_1)
        schedule_event(time+3.617m,out,l4_0)
        schedule_event(time+3.686m,out,l4_1)
        schedule_event(time+4.095m,out,l4_0)
        schedule_event(time+4.141m,out,l4_1)
        schedule_event(time+4.550m,out,l4_0)
        schedule_event(time+4.596m,out,l4_1)
        schedule_event(time+5.005m,out,l4_0)
        schedule_event(time+5.028m,out,l4_1)
        schedule_event(time+5.460m,out,l4_0)
        schedule_event(time+5.506m,out,l4_1)
        schedule_event(time+5.892m,out,l4_0)
        schedule_event(time+5.961m,out,l4_1)
        schedule_event(time+6.325m,out,l4_0)
        schedule_event(time+6.416m,out,l4_1)
        schedule_event(time+6.780m,out,l4_0)
        schedule_event(time+6.916m,out,l4_1)
```

```
            schedule_event(time+7.212m,out,l4_0)
            schedule_event(time+7.371m,out,l4_1)
            schedule_event(time+7.644m,out,l4_0)
            schedule_event(time+7.872m,out,l4_1)
            schedule_event(time+8.054m,out,l4_0)
            schedule_event(time+8.350m,out,l4_1)
            schedule_event(time+8.509m,out,l4_0)
            schedule_event(time+8.827m,out,l4_1)
            schedule_event(time+8.941m,out,l4_0)
            schedule_event(time+9.328m,out,l4_1)
            schedule_event(time+9.396m,out,l4_0)
            schedule_event(time+20000u, wake_up, 0)
                        }

}
```

Appendix 6

Graded Mesh Theory

The theory described in this appendix was originally described by Al-Mukhtar & Sitch (1981).

The method used to calculate the graded mesh took advantage of the different velocities on different lines (slow pulses on short lines and fast pulses on long lines) and a single time step for all the pulses. A typical single node and its equivalent circuit is shown in figure A6.1.

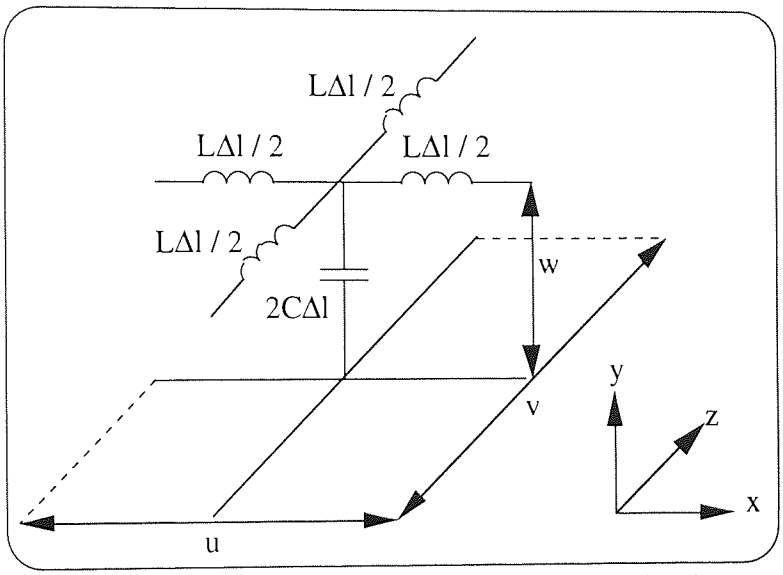

Figure A6.1: Basic Node and its Equivalent Circuit

The velocity of a pulse on a line of length l is:

$$v_n = \frac{l}{\sqrt{L\,C}} = \frac{l}{\tau} \qquad \text{(eqA6.1)}$$

Where L and C are the inductances and capacitances per unit length of the line respectively.

The characteristic impedances of the x and t-directed lines are:

$$Z_x = \frac{w\,v}{u}\,\mu_r \qquad \text{(eqA6.2)}$$

$$Z_z = \frac{w\,u}{v}\,\mu_r \qquad \text{(eqA6.3)}$$

Both values of the impedance are normalised to (τ / ε_o).

The scattering process takes place in two stages, at the nodes and at the nodal boundaries. The nodal scattering takes the following format, where V5 is the open circuited stun at the node:

$$\begin{bmatrix} V1 \\ V2 \\ V3 \\ V4 \\ V5 \end{bmatrix}^r = \frac{1}{Y+4} \begin{bmatrix} -(Y+2) & 2 & 2 & 2 & 2Y \\ 2 & -(Y+2) & 2 & 2 & 2Y \\ 2 & 2 & -(Y+2) & 2 & 2Y \\ 2 & 2 & 2 & -(Y+2) & 2Y \\ 2 & 2 & 2 & 2 & (Y-4) \end{bmatrix} \begin{bmatrix} V1 \\ V2 \\ V3 \\ V4 \\ V5 \end{bmatrix}^i \qquad \text{(eqA6.4)}$$

Where:

$$Y = \frac{2\tau^2}{\mu_o \varepsilon_o^2} \cdot \left[\frac{\varepsilon_o}{w} u v \varepsilon_r - \frac{(u^2 + v^2)\varepsilon_o \mu_o}{u v \tau^2 \mu_r} \right] \qquad \text{(eqA6.5)}$$

The second scattering process takes place at the nodal boundaries where an abrupt change in impedance occurs due to the variation in element sizes. If a pulse propagates on a line of impedance Z_i which meets a line of impedance Z_j, the reflection coefficient at the junction is:

$$\rho_{ij} = \frac{Z_j - Z_i}{Z_j + Z_i} \qquad \text{(eqA6.6)}$$

The transmission coefficient is related to this by:

$$T_{ij} = 1 - \rho_{ij} \qquad \text{(eqA6.7)}$$

The scattering at the junction is summarised by:

$$\begin{bmatrix} V_i \\ V_j \end{bmatrix}^r = \begin{bmatrix} \rho_{ij} & T_{ji} \\ T_{ij} & -\rho_{ij} \end{bmatrix} \begin{bmatrix} V_i \\ V_j \end{bmatrix}^i \qquad \text{(eqA6.8)}$$

The point at which the above scattering takes place is mid-way between the nodes so as to achieve time synchronisation. A two-dimensional program using this thoery can be seen in appendix A5.1.

Appendix 7

The TLM Programs

A7.1 Two-Dimensional TLM Program

```
%%%%%%%%%%%%%%%%%%%%%%%%%%%%%%%%%%%%%%%%%%%%%%%%%%%%%%%%%%%%%%%
% A simple program to predict the electromagnetic radiation from sources in two    %
% dimensions using the TLM modelling technique.                                    %
% The model uses shunt nodes rather than series ones. The program has the          %
% following capabilities:                                                          %
% 1. the ability to model a number of different materials                          %
% 2. the ability to model irregularly graded meshes                                %
% 3. the ability to model varying numbers of sources                               %
% 4. the ability to only store the desired output information.                     %
%                                                                                  %
% Written using MATLAB 4.0                                                         %
%                                                                                  %
% Written by: J. Maggs, September 1995                                             %
% %%%%%%%%%%%%%%%%%%%%%%%%%%%%%%%%%%%%%%%%%%%%%%%%%%%%%%%%%%%%%%
%
clear
%
% Problem default constants
%
eo=8.84e-12;
erd=4.9;
uo=4*pi*1e-7;
urd=1;
sigd=0.05;
%
% Variable problem constants
%
ur1=2000;
er1=1;
sig1=0;
%
nx=input('Number of nodes in the x-direction?  ');
end
ny=input('Number of nodes in the y-direction?  ');
end
dl=input('Default Node length(m)?  ');
end
nits=input('Number of Iterations to Perform?  ');
end
%
sos=1/sqrt(uo*eo);
dt=dl/sos;
tmax=dt*nits;
%
% Specification of the output nodes
%
xo=6;
yo=6;
%
% Specification of the irregularly Graded Mesh
% The length w is set to unity, so it can be ignored for the rest of the program
%
v=dl*ones(ny,nx);
```

```
u=dl*ones(ny,nx);
%
% Specification of the position of alternative materials
%
m=zeros(nx,ny);
%
% Intialisation of matrices
% v1, v2, v3 and v4 are the nodal pulses on the link lines
% v5=pulses on the lossy stubs at the centre of the nodes
%
v1=zeros(ny,nx);
v2=zeros(ny,nx);
v3=zeros(ny,nx);
v4=zeros(ny,nx);
v5=zeros(ny,nx);
%
% Specification of the boundary nodes
%
% The boundary conditions have simply been set up around the
% perimter of the problem area.
%
% Reflection coefficients for the boundaries
%
no=sqrt((uo*urd)/(eo*erd));
zz=sqrt((uo*urd)/(eo*erd));
a=zz/sqrt(2);
r=(a-no)/(a+no);
%
nx=nx-1;
ny=ny-1;
%
% Sources
%
v1(1,1)=1;
v1(1,2)=1;
v2(1,1)=1;
v2(2,1)=1;
%
% Time matrix, time steps
%
t=0;
ni=(tmax/dt)+1;
time=zeros(ni,1);
%
% Output matrices
%
eh=zeros(ni,1);
%
% Starting the iteration process
%
for l=1:ni;
%
% Calculation of the boundary reflections
%
for nb1=1:nx+1;
v1(nb1,1)=r*(v1(nb1,1));
```

```
end
%
for nb2=1:nx+1;
v3(nb2,ny+1)=r*(v3(nb2,ny+1));
end
%
for nb3=1:ny+1;
v2(1,nb3)=r*(v2(1,nb3));
end
%
for nb4=1:ny+1;
v4(nx+1,nb4)=r*(v4(nx+1,nb4));
end
%
% Starting the iteration process for the pulses at the nodes
%
for j=1:nx;
for i=1:ny;
%
% Detrmination of the material parameters from the m matrix
%
if m(i,j)==0;
                    er=erd;
                    ur=urd;
                    sig=sigd;
elseif m(i,j)==1;
                      er=er1;
                      ur=ur1;
                      sig=sig1;
end
%
% Material constants for the scattering matrix
%
yc=((2*dt*dt)/(uo*eo*eo))*((eo*u*v*er)-(((u*u+v*v)*eo*uo)/(u*v*dt*dt*ur)));
%
% Calculating the pulses at the nodes
%
v1(i,j)=(1/(yc+4))*(v1(i,j+1)*((yc+2))+v1(i,j) +v2(i,j)+v2(i+1,j)+(v5(i,j)*2*yc));
%
v2(i,j)=(1/(yc+4))*(v1(i,j+1)+v1(i,j)*(-(yc+2)) +v2(i,j)+v2(i+1,j)+(v5(i,j)*2*yc));
%
v3(i,j)=(1/(yc+4))*(v1(i,j+1)+v1(i,j)+ v2(i,j)*(-(yc+2))+v2(i+1,j)+(v5(i,j)*2*yc));
%
v4(i,j)=(1/(yc+4))*(v1(i,j+1)+v1(i,j)+ v2(i,j)+v2(i+1,j)*(-(yc+2))+(v5(i,j)*2*yc));
%
v5(i,j)=(1/(yc+4))*(v1(i,j+1)+v1(i,j)+v2(i,j)+ v2(i+1,j)+(v5(i,j)*2*yc));
%
v2(i+1,j)=v4(i,j);
v1(i,j+1)=v3(i,j);
end
end
%
% Determination of the reflections at the nodal boundaries due to the irregularly graded
% mesh, in the negative x and y-directions.
%
for p=1:nx;
```

```
for q=1:ny;
%
% Detrmination of the material parameters from the m matrix
%
if m(q,p)==0;
                ura=urd;
elseif m(q,p)==1;
                ura=ur1;
end
%
if m(q,p-1)==0;
                urb=urd;
elseif m(q,p-1)==1;
                urb=ur1;
end
%
if m(q-1,p)==0;
                urc=urd;
elseif m(q-1,p)==1;
                urc=ur1;
end
%
% Line Impedances
%
zy1=(1*v(q,p)/u(q,p))*ura;
zx1=(1*u(q,p)/v(q,p))*ura;
zx2=(1*u(q,p-1)/v(q,p-1))*urb;
zy3=(1*v(q-1,p)/u(q-1,p))*urb;
%
% Junction reflection coefficients
%
rp1=(zx1-zx2)/(zx1+zx2);
rp2=(zx2-zx1)/(zx2+zx1);
rq1=(zy1-zy3)/(zy1+zy3);
rq2=(zy3-zy1)/(zy3+zy1);
%
% Transmission coefficients
%
tp1=1-rp1;
tq1=1-rq1;
tp2=1-rp2;
tq2=1-rq2;
%
% Nodal junction scattering equations
%
v1(p,q)=rp1*v1(p,q)+tp1*v2(p-1,q);
v2(p-1,q)=rp1*v1(p,q)-tp1*v2(p-1,q);
%
v1(p,q)=rq1*v1(p,q)+tq2*v2(p,q-1);
v2(p,q-1)=tq1*v1(p,q)-rq1*v2(p,q-1);
end
end
%
% Evaluating and storing the desired results, where eh is the electric field.
%
eh(l)=(0.5*(v1(xo,yo)+v2(xo,yo)+v3(xo,yo)+ v4(xo,yo)+yc*v5(xo,yo)))/dl;
```

```
%
time(l)=t;
t=t+dt;
%
end
%
```

A7.2 Three-Dimensional TLM Program

```
////////////////////////////////////////////////////////////////////////////////////////////////////////////////////
// A program to predict the electromagnetic radiation from the Eurotherm 583 drive.    //
// The program using three-dimensional Tranmission Line Matrix (TLM) theory. The      //
// program uses the symmetrical condensed node with stubs so that both homgenous      //
// and inhomogenous materials can be modelled, wires are modelled using special       //
// wire nodes.                                                                        //
//                                                                                    //
// Written in C++                                                                     //
//                                                                                    //
// Written by J. Maggs, January 1996                                                  //
////////////////////////////////////////////////////////////////////////////////////////////////////////////////////

#include <math.h>
#include <stdio.h>
#include <stdlib.h>

//
// Function to determine the position in 3-d arrays from column arrays
//
inline int findx (int y, int x, int z)
{
  const int max_x = 17;
  const int max_y = 7;
  const int max_z = 9;
  return  z + max_z*x + max_x*max_z*y;
}
main ()
{
//
// A program to predict the electromagnetic radiation from  sources in three
// dimensions using the TLM modelling technique. The model uses the symmetrical
// condensed node.
//
printf("start\n");
//
// Definition of Variables
//
double dl=0.3;
int nx=17;
int ny=7;
int nz=9;
double nits=7100000;
double ni=7100001;
int xo=13;
int yo=3;
```

```
int zo=5;
double * time;
time = new double[7100002];
double * ehx;
ehx = new double[7100002];
double * ehy;
ehy = new double[7100002];
double * ehz;
ehz = new double[7100002];
long tot=1250;
double * vv1;
vv1 = new double[1250];
double * vv2;
vv2 = new double[1250];
double * vv3;
vv3 = new double[1250];
double * vv4;
vv4 = new double[1250];
double * vv5;
vv5 = new double[1250];
double * vv6;
vv6 = new double[1250];
double * vv7;
vv7 = new double[1250];
double * vv8;
vv8 = new double[1250];
double * vv9;
vv9 = new double[1250];
double * vv10;
vv10 = new double[1250];
double * vv11;
vv11 = new double[1250];
double * vv12;
vv12 = new double[1250];
double * v13e;
v13e = new double[1250];
double * v14e;
v14e = new double[1250];
double * v15e;
v15e = new double[1250];
double * v16h;
v16h = new double[1250];
double * v17h;
v17h = new double[1250];
double * v18h;
v18h = new double[1250];
double * temp1;
temp1 = new double[1250];
double * temp2;
temp2 = new double[1250];
double * temp3;
temp3 = new double[1250];
double * temp4;
temp4 = new double[1250];
double * temp5;
temp5 = new double[1250];
```

```
double * temp6;
temp6 = new double[1250];
double * temp7;
temp7 = new double[1250];
double * temp8;
temp8 = new double[1250];
double * temp9;
temp9 = new double[1250];
double * temp10;
temp10 = new double[1250];
double * temp11;
temp11 = new double[1250];
double * temp12;
temp12 = new double[1250];
double * m;
m = new double[1250];
double eo=8.84e-12;
double erd=1.0;
double er1=1.0;
double uo=1.26e-6;
double urd=1.0;
double ur1=2000.0;
double sigd=0.0;
double sig1=0.0;
double erw=1.0;
double rad=0.011;
double aa=0.0;
double b=0.0;
double bb=0.0;
double cc=0.0;
double cont=0.0;
double dd=0.0;
double dt=0.0;
double ee=0.0;
double ff=0.0;
double hh=0.0;
double ii=0.0;
double jj=0.0;
int l=0;
int loop=0;
int nb1=0;
int nb2=0;
int nb5=0;
int nb6=0;
int nb9=0;
int nb10=0;
double no=0.0;
int pot=0;
double r=0.0;
double s=0.0;
double sos=3e8;
double t=0.0;
double tmax=0.0;
double wa=0.0;
double wb=0.0;
double what=0;
```

```
double vo1=0.0;
double vo2=0.0;
double vo3=0.0;
double vo4=0.0;
double vo5=0.0;
double vo6=0.0;
double vo7=0.0;
double vo8=0.0;
double vo9=0.0;
double vo10=0.0;
double vo11=0.0;
double vo12=0.0;
double vo13=0.0;
double vo14=0.0;
double vo15=0.0;
double vo16=0.0;
double vo17=0.0;
double vo18=0.0;
double vw1=0.0;
double vw2=0.0;
double vw3=0.0;
double vw4=0.0;
double vw5=0.0;
double vw6=0.0;
double vw7=0.0;
double vw8=0.0;
double vw9=0.0;
double vw10=0.0;
double vw11=0.0;
double vw12=0.0;
double vw13=0.0;
double vw14=0.0;
double vw15=0.0;
double vw16=0.0;
double vw17=0.0;
double vw18=0.0;
int x=0;
double Y=0.0;
int y=0;
double Z=0.0;
int z=0;
//
// Setting all the positions in the 3-d arrays to zero
//
for (l=1; l<=tot; ++l)
        {
        vv1[l]=0;
        vv2[l]=0;
        vv3[l]=0;
        vv4[l]=0;
        vv5[l]=0;
        vv6[l]=0;
        vv7[l]=0;
        vv8[l]=0;
        vv9[l]=0;
        vv10[l]=0;
```

```
            vv11[l]=0;
            vv12[l]=0;
            v13e[l]=0;
            v14e[l]=0;
            v15e[l]=0;
            v16h[l]=0;
            v17h[l]=0;
            v18h[l]=0;
            temp1[l]=0;
            temp2[l]=0;
            temp3[l]=0;
            temp4[l]=0;
            temp5[l]=0;
            temp6[l]=0;
            temp7[l]=0;
            temp8[l]=0;
            temp9[l]=0;
            temp10[l]=0;
            temp11[l]=0;
            temp12[l]=0;
            }
//
// Determination of dt and tmax
//
dt=dl/(sos*sqrt(2));
tmax=dt*nits;
//
// Reflection coefficients for the boundaries
//
no=sqrt((uo*urd)/(eo*erd));
b=no/sqrt(2);
r=(b-no)/(b+no);
wo=2*3.14/tc;
//
// Starting the iteration process
//
for (l=1; l<=ni; ++l)
            {
            printf("Still Iterating\n");
            //
            // Source generation
            //
squa=(tt*am/tc)+((2*am*tt/tc)*(sin(1*3.14*tt/tc)/(1*3.14*tt/tc))*((sin(1*3.14*trf/tc)/(1
*3.14*trf/tc))*cos(1*wo*t)));
squa=squa+((2*am*tt/tc)*(sin(2*3.14*tt/tc)/(2*3.14*tt/tc))*((sin(2*3.14*trf/tc)/(2*3.1
4*trf/tc))*cos(2*wo*t)));
squa=squa+((2*am*tt/tc)*(sin(3*3.14*tt/tc)/(3*3.14*tt/tc))*((sin(3*3.14*trf/tc)/(3*3.1
4*trf/tc))*cos(3*wo*t)));
squa=squa+((2*am*tt/tc)*(sin(4*3.14*tt/tc)/(4*3.14*tt/tc))*((sin(4*3.14*trf/tc)/(4*3.1
4*trf/tc))*cos(4*wo*t)));
squa=squa+((2*am*tt/tc)*(sin(5*3.14*tt/tc)/(5*3.14*tt/tc))*((sin(5*3.14*trf/tc)/(5*3.1
4*trf/tc))*cos(5*wo*t)));
squa=squa+((2*am*tt/tc)*(sin(6*3.14*tt/tc)/(6*3.14*tt/tc))*((sin(6*3.14*trf/tc)/(6*3.1
4*trf/tc))*cos(6*wo*t)));
squa=squa+((2*am*tt/tc)*(sin(7*3.14*tt/tc)/(7*3.14*tt/tc))*((sin(7*3.14*trf/tc)/(7*3.1
4*trf/tc))*cos(7*wo*t)));
```

```
squa=squa+((2*am*tt/tc)*(sin(8*3.14*tt/tc)/(8*3.14*tt/tc))*((sin(8*3.14*trf/tc)/(8*3.1
4*trf/tc))*cos(8*wo*t)));
squa=squa+((2*am*tt/tc)*(sin(9*3.14*tt/tc)/(9*3.14*tt/tc))*((sin(9*3.14*trf/tc)/(9*3.1
4*trf/tc))*cos(9*wo*t)));
squa=squa+((2*am*tt/tc)*(sin(10*3.14*tt/tc)/(10*3.14*tt/tc))*((sin(10*3.14*trf/tc)/(1
0*3.14*trf/tc))*cos(10*wo*t)));
squa=squa+((2*am*tt/tc)*(sin(11*3.14*tt/tc)/(11*3.14*tt/tc))*((sin(11*3.14*trf/tc)/(1
1*3.14*trf/tc))*cos(11*wo*t)));
        //
        s=(squa-6.7)/2;
        //
        // Source Positions
        //
        for (y=2; y<=3; ++y)
                {
                x=4;
                z=4;
                pot=findx(y,x,z);
                vv3[pot]=s;
                vv4[pot]=s;
                vv8[pot]=s;
                vv11[pot]=s;
                }
        //
        for (x=5; x<=6; ++x)
                {
                for (y=2; y<=3; ++y)
                        {
                        z=4;
                        pot=findx(y,x,z);
                        vv1[pot]=s;
                        vv2[pot]=s;
                        vv9[pot]=s;
                        vv12[pot]=s;
                        }
                }
        //
        for (y=2; y<=3; ++y)
                {
                for (z=5; z<=6; ++z)
                        {
                        x=6;
                        pot=findx(y,x,z);
                        vv5[pot]=s;
                        vv6[pot]=s;
                        vv7[pot]=s;
                        vv10[pot]=s;
                        }
                }
        //
        for (y=2; y<=3; ++y)
                {
                for (x=4; x<=5; ++x)
                        {
                        z=6;
                        pot=findx(y,x,z);
```

```
                vv1[pot]=s;
                vv2[pot]=s;
                vv9[pot]=s;
                vv12[pot]=s;
                }
        }
//
for (y=2; y<=3; ++y)
        {
        x=4;
        z=5;
        pot=findx(y,x,z);
        vv5[pot]=s;
        vv6[pot]=s;
        vv7[pot]=s;
        vv10[pot]=s;
        }
//
// Calculation of the electric and magnetic fields in the x-direction only
//
// Electric Fields
//
// Determination of the material properties form the material matrix
//
if (m[y,x,z]==0){
        er=erd;
        ur=urd;
        sig=sigd;
        }
else{
        er=er1;
        ur=ur1;
        sig=sig1;
        }
//
// Calculation of material properties
//
sos=1/(sqrt(uo*eo));
Y=(2*er*dl)/(sos*dt)-4;
Z=(2*ur*dl)/(sos*dt)-4;
//
pot=findx(yo,xo,zo);
ehx[l]=-2*(vv1[pot]+vv2[pot]+vv9[pot]+vv12[pot]+Y*v13e[pot])/(dl*(4+Y));
ehy[l]=-2*(vv3[pot]+vv4[pot]+vv8[pot]+vv11[pot]+Y*v14e[pot])/(dl*(4+Y));
ehz[l]=-2*(vv5[pot]+vv6[pot]+vv7[pot]+vv10[pot]+Y*v15e[pot])/(dl*(4+Y));
//
// Starting the iteration process for the pulses at the nodes
//
for (z=1; z<=nz; ++z)
        {
        for (x=1; x<=nx; ++x)
                {
                for (y=1; y<=ny; ++y)
                        {
                        //
                        // Determination of the material properties from the
```

material matrix

```
//
if (m[y,x,z]==0){
        er=erd;
        ur=urd;
        sig=sigd;
        }
else{
        er=er1;
        ur=ur1;
        sig=sig1;
        }
//
Y=(2*er*dl)/(sos*dt)-4;
Z=(2*ur*dl)/(sos*dt)-4;
//
if (er==1 & ur==1){
        aa=0;
        bb=0.5;
        cc=0;
        dd=0.5;
        ee=0;
        ff=0;
        gg=0;
        hh=0;
        ii=0;
        jj=0;
        }
else{
        aa=(-Y/(2*(4+Y)))+(Z/(2*(4+Z)));
        bb=(4/(2*(4+Y)));
        cc=(-Y/(2*(4+Y)))-(Z/(2*(4+Z)));
        dd=(4/(2*(4+Z)));
        ee=bb;
        ff=Z*dd;
        gg=bb*Y;
        hh=(Y-4)/(Y+4);
        ii=dd;
        jj=(4-Z)/(4+Z);
        }
//
pot=findx(y,x,z);
vo1=vv1[pot];
vo2=vv2[pot];
vo3=vv3[pot];
vo4=vv4[pot];
vo5=vv5[pot];
vo6=vv6[pot];
vo7=vv7[pot];
vo8=vv8[pot];
vo9=vv9[pot];
vo10=vv10[pot];
vo11=vv11[pot];
vo12=vv12[pot];
vo13=v13e[pot];
vo14=v14e[pot];
```

```
                    vo15=v15e[pot];
                    vo16=v16h[pot];
                    vo17=v17h[pot];
                    vo18=v18h[pot];
                    //
                    // Calculating the pulses at the nodes
                    //
                    temp1[pot]=(aa*vo1+bb*vo2+dd*vo3+bb*vo9-
dd*vo11+cc*vo12+gg*vo13+ii*vo18);
                    //
                    temp2[pot]=(bb*vo1+aa*vo2+dd*vo6+cc*vo9-
dd*vo10+bb*vo12+gg*vo13-ii*vo17);
                    //
                   temp3[pot]=(dd*vo1+aa*vo3+bb*vo4+bb*vo8+cc*vo11-
dd*vo12+gg*vo14-ii*vo18);
                    //
                    temp4[pot]=(bb*vo3+aa*vo4+dd*vo5-
dd*vo7+cc*vo8+bb*vo11+gg*vo14+ii*vo16);
                    //
                    temp5[pot]=(dd*vo4+aa*vo5+bb*vo6+cc*vo7-
dd*vo8+bb*vo10+gg*vo14-ii*vo16);
                    //
                    temp6[pot]=(dd*vo2+bb*vo5+aa*vo6+bb*vo7-
dd*vo9+cc*vo10+gg*vo15+ii*vo17);
                    //
                    temp7[pot]=(-
dd*vo4+cc*vo5+bb*vo6+aa*vo7+dd*vo8+bb*vo10+gg*vo15+ii*vo16);
                    //
                    temp8[pot]=(bb*vo3+cc*vo4-
dd*vo5+dd*vo7+aa*vo8+bb*vo11+gg*vo14-ii*vo16);
                    //
                    temp9[pot]=(bb*vo1+cc*vo2-
dd*vo6+aa*vo9+dd*vo10+bb*vo12+gg*vo13+ii*vo17);
                    //
                    temp10[pot]=(-
dd*vo2+bb*vo5+cc*vo6+dd*vo7+dd*vo9+aa*vo10+gg*vo15-ii*vo17);
                    //
                    temp11[pot]=(-
dd*vo1+cc*vo3+bb*vo4+bb*vo8+aa*vo11+dd*vo12+gg*vo14+ii*vo18);
                    //
                    temp12[pot]=(cc*vo1+bb*vo2-
dd*vo3+bb*vo9+dd*vo11+aa*vo12+gg*vo13-ii*vo18);
                    //
                v13e[pot]=(ee*vo1+ee*vo2+ee*vo9+ee*vo12+hh*vo13);
                    //
                v14e[pot]=(ee*vo3+ee*vo4+ee*vo8+ee*vo11+hh*vo14);
                    //
                v15e[pot]=(ee*vo5+ee*vo6+ee*vo7+ee*vo10+hh*vo15);
                    //
                    v16h[pot]=(ff*vo4-ff*vo5+ff*vo7-ff*vo8+jj*vo16);
                    //
                    v17h[pot]=(-ff*vo2+ff*vo6+ff*vo9-ff*vo10+jj*vo17);
                    //
                    v18h[pot]=(ff*vo1-ff*vo3+ff*vo11-ff*vo12+jj*vo18);
                    }
                }
```

```
                }
        //
        // Calculation of the scattering within the wire nodes (y direction)
        //
        Y=(2*no*sqrt(erw))/(60*log(0.54*dl/rad));
        wa=Y/(2*(Y+2));
        wb=1/(Y+2);
        //
        for (y=2; y<=3; ++y)
                {
                //
                z=4;
                x=4;
                //
                pot=findx(y,x,z);
                vw1=vv1[pot];
                vw2=vv2[pot];
                vw3=vv3[pot];
                vw4=vv4[pot];
                vw5=vv5[pot];
                vw6=vv6[pot];
                vw7=vv7[pot];
                vw8=vv8[pot];
                vw9=vv9[pot];
                vw10=vv10[pot];
                vw11=vv11[pot];
                vw12=vv12[pot];
                vw13=v13e[pot];
                vw14=v14e[pot];
                //
                vv1[pot]=0.5*(vw2+vw3+vw9-vw11);
                //
                vv2[pot]=0.5*(vw2+vw6-vw10+vw12);
                //
                vv3[pot]=vw2*0.5-vw3*wa+vw4*wb-vw8*wa+vw11*wb-
vw12*0.5+vw13*Y*wb+vw13*Y*wb;
                //
                vv4[pot]=vw3*wb-vw4*wa+vw5*0.5-vw7*0.5+vw8*wb-
vw11*wa+vw13*Y*wb+vw13*Y*wb;
                //
                vv5[pot]=0.5*(vw4+vw6-vw8+vw10);
                //
                vv6[pot]=0.5*(vw2+vw5+vw7-vw9);
                //
                vv7[pot]=0.5*(-vw4+vw6+vw8+vw10);
                //
                vv8[pot]=vw3*wb-vw4*wa-vw5*0.5+vw7*0.5+vw8*wb-
vw11*wa+vw13*Y*wb+vw13*Y*wb;
                //
                vv9[pot]=0.5*(vw1-vw6+vw10+vw12);
                //
                vv10[pot]=0.5*(vw2+vw5+vw7+vw9);
                //
                vv11[pot]=-vw2*0.5-vw3*wa+vw4*wb-
vw8*wa+vw11*wb+vw12*0.5+vw13*Y*wb+vw13*Y*wb;
                //
```

```
                vv12[pot]=0.5*(vw2-vw3+vw9+vw11);
                //
                v13e[pot]=wb*(vw3+vw4+vw8+vw11+vw13*Y-vw14*2);
                //
                v14e[pot]=wb*(vw3+vw4+vw8+vw11-vw13*2+vw14*Y);
                //
                }
        //
        // Calculation of the scattering within the wire nodes (x direction)
        //
        for (y=2; y<=3; ++y)
                {
                for (x=5; x<=6; ++x)
                        {
                        //
                        z=4;
                        //
                        pot=findx(y,x,z);
                        vw1=vv1[pot];
                        vw2=vv2[pot];
                        vw3=vv3[pot];
                        vw4=vv4[pot];
                        vw5=vv5[pot];
                        vw6=vv6[pot];
                        vw7=vv7[pot];
                        vw8=vv8[pot];
                        vw9=vv9[pot];
                        vw10=vv10[pot];
                        vw11=vv11[pot];
                        vw12=vv12[pot];
                        vw13=v13e[pot];
                        vw14=v14e[pot];
                        //
                        vv1[pot]=-vw1*wa+vw2*wb+vw3*0.5-vw9*wa-
vw11*0.5+vw12*wb+vw13*Y*wb+vw14*Y*wb;
                        //
                        vv2[pot]=vw1*wb-vw2*wa+vw6*0.5+vw9*wb-vw10*0.5-
vw12*wa+vw13*Y*wb+vw14*Y*wb;
                        //
                        vv3[pot]=0.5*(vw1+vw4+vw8-vw12);
                        //
                        vv4[pot]=0.5*(vw3+vw5-vw7+vw11);
                        //
                        vv5[pot]=0.5*(vw4+vw6-vw8+vw10);
                        //
                        vv6[pot]=0.5*(vw2+vw5+vw7-vw9);
                        //
                        vv7[pot]=0.5*(-vw4+vw6+vw8+vw10);
                        //
                        vv8[pot]=0.5*(vw3-vw5+vw7+vw11);
                        //
                        vv9[pot]=vw1*wb-vw2*wa-vw6*0.5+vw9*wb+vw10*0.5-
vw12*wa+vw13*Y*wb+vw14*Y*wb;
                        //
                        vv10[pot]=0.5*(-vw2+vw5+vw7+vw9);
                        //
```

```
                        vv11[pot]=0.5*(-vw1+vw4+vw8+vw12);
                        //
                        vv12[pot]=-vw1*wa+vw2*wb-vw3*0.5-
vw9*wa+vw11*0.5+vw12*wb+vw13*Y*wb+vw14*Y*wb;
                        //
                        v13e[pot]=wb*(vw1+vw2+vw9+vw12+vw13*Y-vw14*2);
                        //
                        v14e[pot]=wb*(vw1+vw2+vw9+vw12-vw13*2+vw14*Y);
                        //
                        }
                }
        //
        // Calculation of the scattering within the wire nodes (x direction)
        //
        for (y=2; y<=3; ++y)
                {
                for (x=4; x<=4; ++x)
                        {
                        //
                        z=6;
                        //
                        pot=findx(y,x,z);
                        vw1=vv1[pot];
                        vw2=vv2[pot];
                        vw3=vv3[pot];
                        vw4=vv4[pot];
                        vw5=vv5[pot];
                        vw6=vv6[pot];
                        vw7=vv7[pot];
                        vw8=vv8[pot];
                        vw9=vv9[pot];
                        vw10=vv10[pot];
                        vw11=vv11[pot];
                        vw12=vv12[pot];
                        vw13=v13e[pot];
                        vw14=v14e[pot];
                        //
                        vv1[pot]=-vw1*wa+vw2*wb+vw3*0.5-vw9*wa-
vw11*0.5+vw12*wb+vw13*Y*wb+vw14*Y*wb;
                        //
                        vv2[pot]=vw1*wb-vw2*wa+vw6*0.5+vw9*wb-vw10*0.5-
vw12*wa+vw13*Y*wb+vw14*Y*wb;
                        //
                        vv3[pot]=0.5*(vw1+vw4+vw8-vw12);
                        //
                        vv4[pot]=0.5*(vw3+vw5-vw7+vw11);
                        //
                        vv5[pot]=0.5*(vw4+vw6-vw8+vw10);
                        //
                        vv6[pot]=0.5*(vw2+vw5+vw7-vw9);
                        //
                        vv7[pot]=0.5*(-vw4+vw6+vw8+vw10);
                        //
                        vv8[pot]=0.5*(vw3-vw5+vw7+vw11);
                        //
                        vv9[pot]=vw1*wb-vw2*wa-vw6*0.5+vw9*wb+vw10*0.5-
```

```
vw12*wa+vw13*Y*wb+vw14*Y*wb;
                        //
                        vv10[pot]=0.5*(-vw2+vw5+vw7+vw9);
                        //
                        vv11[pot]=0.5*(-vw1+vw4+vw8+vw12);
                        //
                        vv12[pot]=-vw1*wa+vw2*wb-vw3*0.5-
vw9*wa+vw11*0.5+vw12*wb+vw13*Y*wb+vw14*Y*wb;
                        //
                        v13e[pot]=wb*(vw1+vw2+vw9+vw12+vw13*Y-vw14*2);
                        //
                        v14e[pot]=wb*(vw1+vw2+vw9+vw12-vw13*2+vw14*Y);
                        //
                        }
                }
        //
        // Calculation of the scattering within the wire nodes (z direction)
        //
        for (y=2; y<=3; ++y)
                {
                for (z=5; z<=6; ++z)
                        {
                        //
                        x=6;
                        //
                        pot=findx(y,x,z);
                        vw1=vv1[pot];
                        vw2=vv2[pot];
                        vw3=vv3[pot];
                        vw4=vv4[pot];
                        vw5=vv5[pot];
                        vw6=vv6[pot];
                        vw7=vv7[pot];
                        vw8=vv8[pot];
                        vw9=vv9[pot];
                        vw10=vv10[pot];
                        vw11=vv11[pot];
                        vw12=vv12[pot];
                        vw13=v13e[pot];
                        vw14=v14e[pot];
                        //
                        vv1[pot]=0.5*(vw2+vw3+vw9-vw11);
                        //
                        vv2[pot]=0.5*(vw1+vw6-vw10+vw12);
                        //
                        vv3[pot]=0.5*(vw1+vw4+vw8-vw12);
                        //
                        vv4[pot]=0.5*(vw3+vw5-vw7+vw11);
                        //
                        vv5[pot]=0.5*vw4-wa*vw5+wb*vw6-wa*vw7-
0.5*vw8+wb*vw10+Y*wb*vw13+Y*wb*vw14;
                        //
                        vv6[pot]=0.5*vw2+wb*vw5-wa*vw6+wb*vw7-0.5*vw9-
wa*vw10+Y*wb*vw13+Y*wb*vw14;
                        //
                        vv7[pot]=-0.5*vw4-wa*vw5+wb*vw6-
```

```
wa*vw7+0.5*vw8+wb*vw10+Y*wb*vw13+Y*wb*vw14;
                        //
                        vv8[pot]=0.5*(vw3-vw5+vw7+vw11);
                        //
                        vv9[pot]=0.5*(vw1-vw6+vw10+vw12);
                        //
                        vv10[pot]=-0.5*vw2+wb*vw5-wa*vw6+wb*vw7+0.5*vw9-
wa*vw10+Y*wb*vw13+Y*wb*vw14;
                        //
                        vv11[pot]=0.5*(-vw1+vw4+vw8+vw12);
                        //
                        vv12[pot]=0.5*(vw2-vw3+vw9+vw11);
                        //
                        v13e[pot]=wb*(vw5+vw6+vw7+vw10+Y*vw13-2*vw14);
                        //
                        v14e[pot]=wb*(vw5+vw6+vw7+vw10-2*vw13+Y*vw14);
                        //
                        }
                }
        //
        // Calculation of the scattering within the wire nodes (z direction)
        //
        for (y=2; y<=3; ++y)
                {
                //
                z=5;
                x=4;
                //
                pot=findx(y,x,z);
                vw1=vv1[pot];
                vw2=vv2[pot];
                vw3=vv3[pot];
                vw4=vv4[pot];
                vw5=vv5[pot];
                vw6=vv6[pot];
                vw7=vv7[pot];
                vw8=vv8[pot];
                vw9=vv9[pot];
                vw10=vv10[pot];
                vw11=vv11[pot];
                vw12=vv12[pot];
                vw13=v13e[pot];
                vw14=v14e[pot];
                //
                vv1[pot]=0.5*(vw2+vw3+vw9-vw11);
                //
                vv2[pot]=0.5*(vw1+vw6-vw10+vw12);
                //
                vv3[pot]=0.5*(vw1+vw4+vw8-vw12);
                //
                vv4[pot]=0.5*(vw3+vw5-vw7+vw11);
                //
                vv5[pot]=0.5*vw4-wa*vw5+wb*vw6-wa*vw7-
0.5*vw8+wb*vw10+Y*wb*vw13+Y*wb*vw14;
                //
                vv6[pot]=0.5*vw2+wb*vw5-wa*vw6+wb*vw7-0.5*vw9-
```

```
wa*vw10+Y*wb*vw13+Y*wb*vw14;
                //
                vv7[pot]=-0.5*vw4-wa*vw5+wb*vw6-
wa*vw7+0.5*vw8+wb*vw10+Y*wb*vw13+Y*wb*vw14;
                //
                vv8[pot]=0.5*(vw3-vw5+vw7+vw11);
                //
                vv9[pot]=0.5*(vw1-vw6+vw10+vw12);
                //
                vv10[pot]=-0.5*vw2+wb*vw5-wa*vw6+wb*vw7+0.5*vw9-
wa*vw10+Y*wb*vw13+Y*wb*vw14;
                //
                vv11[pot]=0.5*(-vw1+vw4+vw8+vw12);
                //
                vv12[pot]=0.5*(vw2-vw3+vw9+vw11);
                //
                v13e[pot]=wb*(vw5+vw6+vw7+vw10+Y*vw13-2*vw14);
                //
                v14e[pot]=wb*(vw5+vw6+vw7+vw10-2*vw13+Y*vw14);
                //
                }
        //
        // Calculation of the boundary reflections
        //
        for (x=1; x<=nx; ++x)
                {
                for (y=1; y<=ny; ++y)
                        {
                        z=1;
                        pot=findx(y,x,z);
                        temp4[pot]=r*vv4[pot];
                        temp2[pot]=r*vv2[pot];
                        //
                        z=9;
                        pot=findx(y,x,z);
                        temp9[pot]=r*vv9[pot];
                        temp8[pot]=r*vv8[pot];
                        }
                }
        //
        for (z=1; z<=nz; ++z)
                {
                for (y=1; y<=ny; ++y)
                        {
                        x=1;
                        pot=findx(y,x,z);
                        temp3[pot]=r*vv3[pot];
                        temp6[pot]=r*vv6[pot];
                        //
                        x=17;
                        pot=findx(y,x,z);
                        temp10[pot]=r*vv10[pot];
                        temp11[pot]=r*vv11[pot];
                        }
                }
        //
```

```
for (x=1; x<=nx; ++x)
        {
        for (z=1; z<=nz; ++z)
                {
                y=1;
                pot=findx(y,x,z);
                temp1[pot]=-1*vv1[pot];
                temp5[pot]=-1*vv5[pot];
                //
                y=7;
                pot=findx(y,x,z);
                temp7[pot]=r*vv7[pot];
                temp12[pot]=r*vv12[pot];
                }
        }
//
// Transferral of the temp matrices into the pulse matrices
//
for (z=1; z<=nz; ++z)
        {
        for (x=1; x<=nx; ++x)
                {
                for (y=1; y<=ny; ++y)
                        {
                        pot=findx(y,x,z);
                        vv1[pot]=temp1[pot];
                        vv2[pot]=temp2[pot];
                        vv3[pot]=temp3[pot];
                        vv4[pot]=temp4[pot];
                        vv5[pot]=temp5[pot];
                        vv6[pot]=temp6[pot];
                        vv7[pot]=temp7[pot];
                        vv8[pot]=temp8[pot];
                        vv9[pot]=temp9[pot];
                        vv10[pot]=temp10[pot];
                        vv11[pot]=temp11[pot];
                        vv12[pot]=temp12[pot];
                        }
                }
        }
//
// Connection stage (ie the transferrance of the pulses onto the correct stubs)
//
for (z=1; z<=nz; ++z)
        {
        for (x=1; x<=nx; ++x)
                {
                for (y=1; y<=ny; ++y)
                        {
                        pot=findx(y,x,z);
                        //
                        if (x<=nx){
                                cont=vv10[pot];
                                vv10[pot]=vv6[findx(y,x+1,z)];
                                vv6[findx(y,x+1,z)]=cont;
                                cont=vv11[pot];
```

```
                                        vv11[pot]=vv3[findx(y,x+1,z)];
                                        vv3[findx(y,x+1,z)]=cont;
                                }
                                else{
                                        cont=0;
                                }
                                //
                                if (y<=ny){
                                        cont=vv7[pot];
                                        vv7[pot]=vv5[findx(y+1,x,z)];
                                        vv5[findx(y+1,x,z)]=cont;
                                        cont=vv12[pot];
                                        vv12[pot]=vv1[findx(y+1,x,z)];
                                        vv1[findx(y+1,x,z)]=cont;
                                }
                                else{
                                        cont=0;
                                }
                                //
                                if (z<=nz){
                                        cont=vv8[pot];
                                        vv8[pot]=vv4[findx(y,x,z+1)];
                                        vv4[findx(y,x,z+1)]=cont;
                                        cont=vv9[pot];
                                        vv9[pot]=vv2[findx(y,x,z+1)];
                                        vv2[findx(y,x,z+1)]=cont;
                                }
                                else{
                                        cont=0;
                                }
                                //
                                }
                        }
                }
        //
        time[l]=t;
        t=t+dt;
        //
        }       // end of main loop
//
// Writing of the arrays ehx, ehy, ehz and time to files
//
FILE *xalted;
//
xalted=fopen("elecx.out","w");
for (loop=1; loop<=ni; loop=loop+50)
        {
        what=ehx[loop];
        fprintf(xalted,"%-12.5e\n",what);
        }
fclose(xalted);
//
FILE *yeltsin;
//
yeltsin=fopen("elecy.out","w");
for (loop=1; loop<=ni; loop=loop+50)
```

```
        {
        what=ehy[loop];
        fprintf(yeltsin,"%-12.5e\n",what);
        }
//fclose(yeltsin);
FILE *zenophobe;
//
zenophobe=fopen("elecz.out","w");
for (loop=1; loop<=ni; loop=loop+50)
        {
        what=ehz[loop];
        fprintf(zenophobe,"%-12.5e\n",what);
        }
fclose(zenophobe);
//
FILE *tinnitus;
tinnitus=fopen("time.out","w");
for (loop=1; loop<=ni; loop=loop+50)
        {
        what=time[loop];
        fprintf(tinnitus,"%-12.5e\n",what);
        }
fclose(tinnitus);
//
//
return(0);
}       // end of program
```

Appendix 8

Papers Published

A8.1 Paper 1

AUTHORS: Maggs. J, Oliver. T, Wright. M. T, Payn. M

TITLE: Prediction of the Conducted Emissions in Variable Speed Motor Drives

CONFERENCE: Universities Power Engineering Conference (UPEC)

DATE: 18 -20 September 1996

LOCATION: Iraklion, Crete

PAGES: 211 - 214

VOLUME: 3

Aston University

Content has been removed for copyright reasons

A8.2 Paper 2

AUTHORS: Maggs. J, Oliver. T, Wright. M. T

TITLE: Electromagnetic Compatibility of Variable Speed Drives

CONFERENCE: Power Electronics and Variable Speed Drives (PEVD)

DATE: 23 - 25 September 1996

LOCATION: Nottingham, UK

PAGES: 552 - 557

Aston University

Content has been removed for copyright reasons